2001

Photoemission and Photo-Absorption Studies of Ultrathin Iron Films on Copper(100) Oxidized at Elevated Temperature.

Reginaldt Hamilton Madjoe
Louisiana State University and Agricultural & Mechanical College

INFORMATION TO USERS

This manuscript has been reproduced from the microfilm master. UMI films the text directly from the original or copy submitted. Thus, some thesis and dissertation copies are in typewriter face, while others may be from any type of computer printer.

The quality of this reproduction is dependent upon the quality of the copy submitted. Broken or indistinct print, colored or poor quality illustrations and photographs, print bleedthrough, substandard margins, and improper alignment can adversely affect reproduction.

In the unlikely event that the author did not send UMI a complete manuscript and there are missing pages, these will be noted. Also, if unauthorized copyright material had to be removed, a note will indicate the deletion.

Oversize materials (e.g., maps, drawings, charts) are reproduced by sectioning the original, beginning at the upper left-hand corner and continuing from left to right in equal sections with small overlaps.

Photographs included in the original manuscript have been reproduced xerographically in this copy. Higher quality 6" x 9" black and white photographic prints are available for any photographs or illustrations appearing in this copy for an additional charge. Contact UMI directly to order.

ProQuest Information and Learning
300 North Zeeb Road, Ann Arbor, MI 48106-1346 USA
800-521-0600

PHOTOEMISSION AND PHOTO-ABSORPTION STUDIES OF ULTRATHIN Fe FILMS ON Cu(100) OXIDIZED AT ELEVATED TEMPERATURE

A Dissertation

Submitted to the Graduate Faculty of the
Louisiana State University and
Agricultural and Mechanical College
in partial fulfillment of the
requirements for the degree of
Doctor of Philosophy

in

The Department of Physics and Astronomy

by
Reginaldt Madjoe
B. S(Hons)., University of the Western Cape, Bellville, South Africa, 1991
M. S., University of the Western Cape, Bellville, South Africa, 1994
M. S., Louisiana State University, 1997
May, 2001

Bell & Howell Information and Learning Company
300 North Zeeb Road
P.O. Box 1346
Ann Arbor, MI 48106-1346

Acknowledgements

I am deeply grateful to my graduate advisor, Dr Richard L. Kurtz and also Dr Roger L. Stockbauer, for their suggestion of this problem, for their close guidance and great patience, and for their editorial help during the writing of papers and this dissertation. Their advice on research and writing has been indispensable in completing this work and will be invaluable to my future scientific career. I have benefited a great deal from their deep insight into physics, their experimental skills, their broad knowledge and from their numerous comments and suggestions. Many thanks to my graduate committee members Dr Ravi Rau (for all the help with the theoretical interpretation and useful discussions), Dr Phillip Adams (for the experimental help in designing the sample rotation stage used in this investigation) and Dr Kuo from Mathematics (for his patience and understanding).

Many thanks go to the current and former members of the Surface Science group at LSU: Dr Krishnan Subramanian (who served as my mentor when I joined the group in 1995), Dr Jeevananda Karunamuni (our STM specialist whose STM work I constantly used as a reference in this investigation), Alexey Koveshnikov (my experimental partner with whom I worked in parallel for almost 4 years, who helped with some figures used in this dissertation, and who will report on the magnetic behavior of Fe/Cu and Co/Cu systems), Alice Acatrinei (for experimental help), Dr Xingyu Gao (the postdoc from Germany for his experimental help) and Roger Wendell (whose help with some drawings was invaluable). Gergana Stoitcheva for her friendship and help with the preparation of this dissertation and useful discussion.

I also extend my appreciation to the Physics Department and all its members for their friendliness and help throughout my graduate career. In particular Ms Brenda Smith, who helped with some typing as well as Ms Arnell Jackson, for constant encouragement and help. The technical assistance received from the physics department machine shop and electronic shop has been of great value.

A special thanks goes to the staff of the Center for Advanced Microstructures and Devices (CAMD) and the staff of the PGM Beamline (Drs Phil Sprunger and Eizi Morikawa) at CAMD where most of my experiments were performed.

I would like to thank my friends and family especially my mother Mary, sister Unice, and brother Simon, for being understanding and supportive in difficult times, as my in-laws the Scheepers family, for constant support.

My biggest thanks and appreciation is reserved for my wife of 12 years Lynette, for all the sacrifices she made and for her unselfish support and understanding during the time of my graduate studies. To my two boys Sean Michael and Clarence Reginald, thanks for understanding that "Daddy must go to CAMD/Lab". Finally to my Lord and savior Jesus Christ, for the strength to finish this project.

Table of Contents

List of Figures

Abstract

In this investigation, I have focused on understanding the structure and morphology of ultrathin iron oxide films and characterizing them by using LEED, photoemission (both angle-resolved and angle-integrated) and photoabsorption measurements. Fe films were deposited on a Cu(100) substrate at room temperature growing in a layer by layer fashion. The sample was then annealed to 810K in oxygen ambient. This oxidation process led to dramatic changes of the sample surface and electronic structure depending on initial Fe coverage. Half-metallic oxides such as CrO_2 and Fe_3O_4 may provide opportunities for new magnetic devices since their single spin orientation at the Fermi level gives rise to spin-dependent transport. However, these films are most often grown on oxide substrates that are not currently incorporated in GMR devices. We report a study of the electronic and geometric structures of Fe_3O_4 films grown on copper, which is currently used in commercial heterostructures.

An array of techniques including ARUPS, NEXAFS, LEED and STM were used to characterize these films. They were grown by depositing Fe on Cu(001) at room temperature and oxidizing at 810K in 10^{-6} Torr O_2 ambient. The particular oxide phase that forms depends on the initial Fe thickness. For Fe films less than 2 ML thick, LEED and STM measurements show that oxidation produces an FeO(111) bilayer. The oxide forms long, narrow strips with two mutually-perpendicular orientations aligned along Cu[110] and [$1\bar{1}0$].

Oxidation of thicker Fe layers give crystallites of $Fe_3O_4(111)$ of micron dimensions, which are oriented 15° from the [010] directions and highly lattice-matched to the Cu substrate.

Both core level and valence band photoemission data provide spectroscopic confirmation for the classification of the Fe oxides. Near-edge X-ray absorption fine-structure (NEXAFS) taken at the oxygen K-edge, shows the existence of two distinct valence states for Fe_3O_4 (Fe^{2+} and Fe^{3+}) while spectra for FeO shows a single valence state (Fe^{2+}).

Chapter 1

Introduction

The computer industry has experienced rapid changes in the past few years, as the need to "stay connected" led to a huge public demand for portable communication devices like very small laptops, handheld PCs, etc. This has fueled a need to reduce dramatically the size of computer components. The new technology used in these components is made possible, in part, to new physics recently discovered in the materials studied in this dissertation.

Exactly twenty years ago (1980), IBM introduced the world's first gigabyte-capacity disk drive, the 3380. It was as big as a refrigerator, weighed over 265 kg and cost $40,000. However, IBM recently (June 20, 2000) announced that they manufactured a 1 gigabyte *micro*drive with physical dimensions: height ~ 5.0 mm, width ~ 42.8 mm, depth ~ 36.4 mm and it weighs ~16g. The current cost of the *micro*drive is less than $500. With this new technology, IBM has managed to place one thousand million bytes of information on a microdrive that is about the size of a

US quarter coin! This announcement implies even further development in the affordable miniaturization and portability of electronic products.

The most significant developments have been in the field of ultra-thin magnetic films and multilayers, which have applications in magnetic memories and sensors. This technology necessitates the consideration of new physics that is displayed by materials in these shrinking dimensions. Prinz[1] in a recent Science review article entitled "Magnetoelectronics" described how spin-dependent transport can lead to even more interesting devices and revolutionize the design of computational instrumentation.

Prior hard drive technology involved the use of inductive heads for reading and writing data. Recently however, magnetoresistive (MR) sensors have been used for reading data written on hard disks, and storage density has increased significantly. Currently, a giant magneto resistive (GMR) effect, that provides even greater sensitivity than MR is used in computer disk sensors.

The widely cited report of the discovery of GMR was first reported in 1988 by Baibich *et al.*[2] Since that time, intense investigations have led to a general understanding of the phenomenon. Layered magnetic thin-film structures composed of alternating ferromagnetic (FM) and non-magnetic layers provide potential barriers at their interfaces which set up quantum well states in the non-magnetic spacer. This

state couples magnetic information from one FM layer to the other and, depending on the thickness of the spacer, can induce either parallel or antiparallel alignment of the FM layers. The thickness is determined by the regions of the Fermi surface of the non-magnetic spacer which provide for strong scattering. Strong coupling occurs for regions of the Fermi surface that are nearly parallel, or well-nested.

For parallel magnetic moments of the FM layers, the spin-dependent scattering of the carriers is minimized, and the material has its lowest resistance. However, when the FM layers are anti-aligned, the spin-dependent scattering of the carriers is maximized, and the material has its highest resistance. The directions of the magnetic moments are manipulated by external magnetic fields that are applied to the materials. These materials can therefore be fabricated to produce significant changes in resistance, at room temperature, by applying a relatively small external magnetic field.

Spin-polarized transport will occur naturally for materials (like ferromagnets Fe, Co and Ni) in which there is an imbalance (40-50%) of the spin population at the Fermi level due to the unequal filling of the spin-polarized bands.[1] Ideal materials needed for spin-dependent transport will be 100% spin-polarized. These materials are termed half-metallic since they have only one spin orientation at the Fermi level.

Three classes of materials that have been proposed to exhibit half-metallic behavior include the Heusler alloys (such as $Ni_{1-x}Mn_xSb$), the so-called colossal magnetoresistive perovskites (such as $La_xCa_{1-x}CuO_3$ and oxides of transition metal elements, like CrO_2 and Fe_3O_4.[3] Andreev reflection measurements have recently shown that CrO_2 is indeed 90% spin-polarized at the Fermi surface and other oxides such as $La_{0.7}Sr_{0.3}MnO_3$ display a significant spin polarization as well.[4] The application of these materials in realistic devices, however, is impeded by the need to produce the half-metallic material with high conductivity in a thin-film form. The application of Heusler alloys in devices application has been problematic due to difficulties in controlling the stoichiometry in thin films. It appears that Fe_3O_4 is an excellent candidate material for device development.

Computations by Zhang and Satpathy in 1991 suggested complete minority spin polarization at the Fermi level.[5] Early spin-resolved secondary-electron measurements by Alvarado *et al.*[6] observed a 40% spin-polarization in the empty states near the Fermi level. Other advantages of using Fe_3O_4 in devices is the fact

that the Curie temperature is well above room temperature (858 K) and it has a relatively high electrical conductivity of 100 $(\Omega\ cm)^{-1}$ at room temperature.[3]

1.1 Oxides of Fe

The two stable oxidation states of Fe are Fe^{2+} and Fe^{3+}, and four stable bulk oxide phases exist.[7] α-Fe_2O_3 (hematite) has the hexagonal crystal structure of corundum with Fe^{3+} cations located in distorted oxygen octahedra (Figure 1.1b). Fe_3O_4 (magnetite) has the cubic inverse spinel structure with Fe^{2+} cations in octahedral sites and Fe^{3+} cations in both octahedral and tetrahedral sites, with each layer of iron separated by a hexagonal layer of oxygen ions (Figure 1.1c). The spins of Fe ions in octahedral and tetrahedral sites couple antiferromagnetically, resulting in a net magnetization due to the different total magnetic moment in the two sublattices.

The high room temperature conductivity of magnetite is attributed to a continuous hopping of electrons between octahedral Fe ions.[8] This hopping is frozen out below ~122K at which the Verwey phase transition occurs.[9]

γ-Fe_2O_3, just like magnetite, crystallizes in the cubic inverse spinel structure, but with vacancies and Fe^{3+} cations replacing the Fe^{2+} cations in octahedral sites.

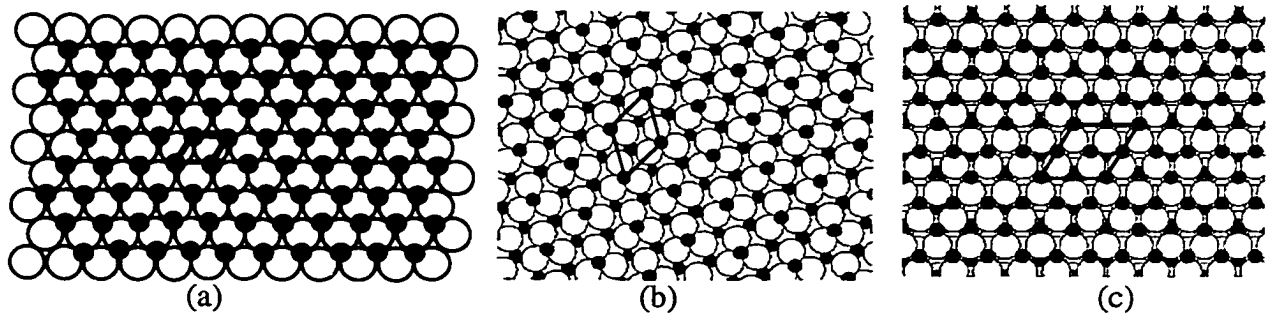

Figure 1.1: Schematic illustration of the surface periodicities of Fe Oxides. The dark circles represent the Fe cations and the open circles represent the O ions. The unit cell is indicated on the schematic of each oxide. (a) FeO(111) surface, (b) α-Fe_2O_3(0001) surface and (c) Fe_3O_4(111) surface.

$Fe_{1-x}O$ (wustite) has the NaCl structure containing Fe^{2+} cations octahedrally coordinated to the oxygen anions (Figure 1.1a).

In the past, spectroscopic studies of the oxides of Fe were limited to mostly bulk single crystals because of the difficulty of preparing thin films on suitable substrates, with well-defined stoichiometry.[7] Photoemission studies on single crystals were also hampered by difficult substrate preparation. However, recent works have demonstrated that it is possible to stabilize a few of these complex oxide structures in the form of ultrathin films, by epitaxial growth on appropriate crystalline substrates. Thin films of Fe oxides have been successfully grown on oxide substrates such as MgO and NiO, on the dissimilar metal Pt(111) and on the Fe(110) surface.[10, 11, 12, 13] In the case of NiO and MgO, O-plasma assisted oxidation of evaporated-Fe films was found to produce Fe_3O_4 films for substrate temperatures between 540 and 570K.[10, 14]

One monolayer thick $Fe_{1-x}O$ was formed on Pt(111) by oxidizing a submonolayer of Fe. Fe_3O_4(111) could subsequently be prepared by further Fe deposition and oxidation cycles and annealing in 10^{-6} mbar O_2 at 1020K.[15] A recent report on the oxidation of Fe(110) showed that the reaction proceeds through

two distinct phases: an initial (paramagnetic) FeO(111) layer is subsequently transformed into a stable Fe_3O_4(111) overlayer at high oxygen doses of more than 600 Langmuir (1 Langmuir (L) = 10^{-6} Torr-sec exposure).[13] The magnetization of the resultant Fe_3O_4(111) overlayer and the Fe(110) substrate are coupled antiparallel.

Room temperature oxidation of Fe on Cu(100) has been reported previously.[16, 17, 18] Kishi and Nishioka studied the room temperature oxidation of Fe/Cu(100), using mostly XPS (X-ray Photoelectron Spectroscopy) for characterization of the 2*p* peaks.[17] They found that 0.3 and 0.6 ML Fe on Cu exposed to 750L O_2 gave shifts of the Fe $2p_{3/2}$ peak ascribed to FeO-like species. For 2 ML of Fe, however, they concluded that the shift of the Fe $2p_{3/2}$ peak was more consistent with Fe_3O_4-like species. However, the interpretation of Fe 2*p* core-levels in a mixed oxide is problematic due to the presence of satellite structure and the broad, overlapping features from different Fe charge states.

Daas et al.,[16] also investigated both the Fe film thickness and the oxygen exposure dependence at room temperature using an array of spectroscopic tools, including XPS (X-ray Photoelectron Spectroscopy), UPS (Ultraviolet Photoelectron Spectroscopy) and AES (Auger Electron Spectroscopy). Based on the Fe 2*p* XPS spectra shape and core-level shift they concluded that Fe_2O_3 is always formed on the

surface of 0.5 – 10.0 ML Fe thin films exposed to 10^4 Langmuir of oxygen independent of the iron thickness. Lozzi, *et al.* also reported that α-Fe_2O_3 always forms on the Cu(100) surface at room temperature, independent of initial Fe thickness. [18] However, they also reported that submonolayer Fe coverage (0.5 – 1.0 ML), exposed to increasing amounts of oxygen, has shown the presence of both Fe^{2+} and Fe^{3+} in the middle stages of oxidation.

These contradictory results at 300 K warrant further investigation of the Fe oxidation process on Cu(100) to determine which factors (temperature, oxygen exposure, etc.) governs the formation of which oxide.

1.2 Motivation for this Study

In a previous dissertation from this group, Karunamuni grew Fe on Cu(100) and investigated its oxidation at elevated temperatures.[19] Cu was chosen as a substrate since it is used in device fabrication and is known to provide a suitable template for ordered growth of a fcc Fe phase. Using STM and LEED, Karunamuni found that two distinct oxides form, depending on the initial Fe coverage. The STM showed that the low coverage phase (< 2 ML Fe) grew in strips along the Cu[110] azimuths while the high coverage phase (> 2 ML Fe) grew in strips oriented 15°

from Cu[001]. The oxide also flattened the Cu surface producing atomically-flat micron-wide terraces.

Based on the LEED and STM results, Karunamuni proposed a structural model for oxide growth. For initial Fe coverages below 2 monolayers, a single bilayer of $Fe_{1-x}O$ forms, and for thicker iron films the Fe_3O_4 spinel phase forms. This model, however, is based solely on structural studies and it is critical to understand both the structural and the electronic properties of this material.

However, some questions remained unanswered. For instance, does the valency of the Fe oxides agree with the known valencies of bulk oxides? Does the electronic correlate with the geometric structures of the different Fe oxides that form on Cu(100) using the high temperature oxidation technique?

This investigation will serve to address these unanswered questions by making use of spectroscopic techniques to investigate the valence states of the different oxides. To our knowledge there have been no previous studies of the electronic structure associated with the high temperature oxidation of ultrathin Fe films deposited on a Cu(100) substrate. The LEED, photoemission and photoabsorption data obtained in this investigation will be compared to the structural and morphological changes observed previously.

The remainder of this thesis is presented in the following order: Chapter 2 will describe the experimental methods and techniques applied in this thesis. Chapter 3 will discuss the growth of metallic Fe on Cu(100) and give results tying the known thickness-dependent magnetic and structural changes to the electronic structure. Chapter 4 will describe the high temperature oxidation of the Fe/Cu(100) and present measurements of structural properties (using LEED) as well as electronic properties using photoemission (UPS and XPS) and photoabsorption (NEXAFS - near edge X-ray absorption fine structure). Chapter 5 presents a discussion of the results obtained during this investigation followed by the conclusions.

Chapter 2

The Experimental Method

This chapter describes the experimental methods and instrumentation employed in this research. Complementary information from fundamentally different experiments is essential in the study and characterization of solid surfaces since a multiplicity of information helps with the analysis and interpretation of data. This chapter describes the basic principles of the spectroscopic techniques that have been used in this research as well as the instrumentation that was used to obtain the experimental data.

Most of the experimental methods described below involve electron emission from a sample surface as indicated schematically in figure 2.1. In photoemission spectroscopy (PES) the sample is irradiated with a photon of energy $h\nu$, and an electron is emitted with kinetic energy, $KE = h\nu - \phi - E_B$ (see figure 2.1 (a)) (Note: E_B = binding energy of electron, ϕ = workfunction of the material).

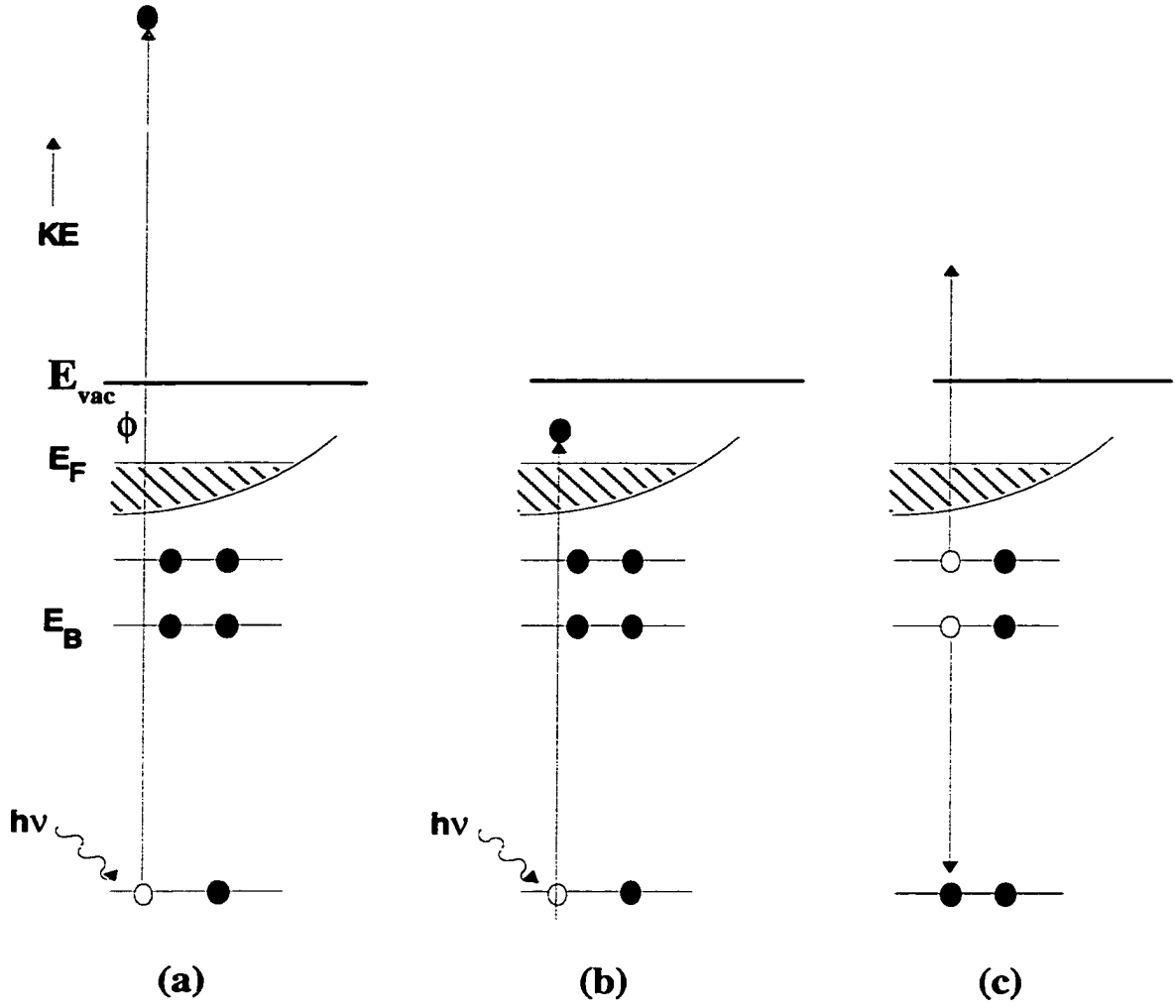

Figure 2.1: Schematic diagram of the transitions involved in various spectrosopies that will be discussed in this investigtion. (a) Photoemission spectroscopy(PES); (b) X-ray absorption spectroscopy(XAS); (c) Auger electron spectroscopy (AES)

In X-ray absorption spectroscopy (XAS) one scans the radiation energy ($h\nu$) and observes the increase in secondary electron yield at the threshold (or edge) when a core level is excited to the first unoccupied state (note: $h\nu = E_B + \phi$ at the threshold for metals.) (see figure 2.1(b)).

Auger electron spectroscopy (AES) is based on the relaxation of the excited state created in photoemission: it is a core-hole decay process whereby the hole is filled by an electron from a higher level and the excess energy is taken away by an ejected electron (see figure 2.1 (c)).

The different methods provide us with a wealth of information regarding the near-surface region of the material. Near-surface because the relevant electrons are those that are emitted from the sample without undergoing inelastic scattering since scattering removes the information contained in the energy and direction of the electron's motion. Since the electron mean free path for inelastic scattering is limited, our measurements are surface sensitive. Seah and Dench showed that most materials exhibit a minimum in the mean free path λ, of about 2 to 3 Å for 60 eV electron kinetic energy. (Most of our measurements are made near this minimum.)

Low-Energy Electron Diffraction (section 2.1.1) provides us information regarding surface geometry and degree of order. X-ray photoemission spectroscopy

(section 2.2.1) is used to provide compositional information since it probes core-level states, and through measurements of core-level shifts, can reveal the various valence states that arise due to chemical reactions.[20] Ultraviolet photoemission spectroscopy (section 2.2.2) is used to study valence-band electronic structure and for observing the interaction of different molecules with the sample surface. Photoabsorption (section 2.3) was used as a complementary technique to probe the deep-level core states. NEXAFS (Near-Edge X-Ray Absorption Fine Structure), a technique whereby high-energy photons are used to stimulate core-level transitions, is used to provide compositional information and indicate core-level shifts in different chemical environments.[20]

2.1 Low-Energy Electron Diffraction (LEED)

Elastic scattering or diffraction of a monoenergetic beam of electrons is a standard technique used for obtaining structural information about surfaces. Low-energy electron diffraction (LEED) can provide information on the crystallographic quality of a freshly prepared crystal sample surface as well as to obtain morphological data on atoms, molecules, and thin films on crystal surfaces.[20, 21, 22, 23] The surface atomic structure determines the periodicity of the system and thus the basic unit of repetition on the surface unit mesh.[23] These characteristics

and the long-range translational symmetry provide a periodic system amenable to diffraction methods.

The diffraction process in LEED is described by the Bragg condition. It requires that energy be conserved (elastic collisions) and that the momentum transfer ($\boldsymbol{p} = \hbar \boldsymbol{k}$) be equal to a reciprocal lattice vector **G**. So for incident wavevector **k**, (and outgoing wavevector, **k'**) one obtains

$$\Delta \boldsymbol{k} = \boldsymbol{k}' - \boldsymbol{k} = \boldsymbol{G}. \qquad (2.1)$$

This can be seen using an Ewald construction as shown in figure 2.2, for a 2D surface lattice.[23] The reciprocal lattice points of a 3D lattice become rods in the direction normal to the surface since the surface is not periodic in this direction. The Bragg scattering condition as expressed above is satisfied where the rods intersect with the Ewald sphere and thus describes beams of diffracted electrons.

Simple inspection of the resulting LEED pattern and measurement of the geometrical spot positions can yield a wealth of information about the symmetry and perfection of the surface. A perfect LEED pattern must exhibit sharp spots with high contrast and low background intensity. Random defects and imperfections broaden spots and increase the background intensity. Complex LEED patterns are obtained when the surface undergoes reconstructions that gives rise to superstructures.

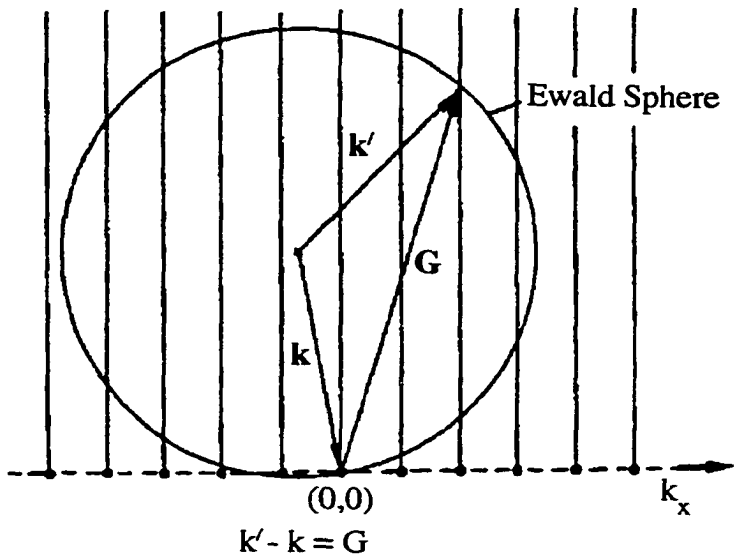

Figure 2.2: Ewald construction for elastic scattering on a 2D surface lattice.[23] Incident electron with wavevector **k** diffracts with momentum transfer G to new state k'. The corresponding 2D reciprocal lattice points(hk) are indicated with dots on a cut along k_x. The diffraction condition is fulfilled where the Ewald sphere and rods intersect, i.e. at (hk)=(20), etc.

When atoms or molecules are adsorbed on surfaces, they often order in arrays that have lattice parameters that are related to those of the substrate and this can give rise to additional spots (half order, for example) in the LEED pattern. Elongated or streaky spots (combined with spot splitting) can indicate the presence of an overlayer on the substrate that has a lower degree of symmetry or unrelated lattice parameter in the corresponding real space.

2.1.1 LEED Optics

The standard experimental setup for LEED consists of an electron gun to produce an electron beam with primary energies ranging from about 20 eV up to 500 eV, and a display system to observe the Bragg diffraction spots.

All LEED measurements reported here were performed at normal incidence with emission current of about 0.2 mA, using a retractable rear-view LEED optics. We used energies below 300 eV since the mean free path λ of these slow electrons in the solid is short enough to give good surface sensitivity.[23]

The electron wavelength, λ_e, can be obtained from the de Broglie relation

$$\lambda_e = \sqrt{\frac{150.4}{E}} \ , \qquad (2.2)$$

where λ_e is in Å and E in electron volts (eV). For E < 300eV we get λ_e in the Å range that is in the same magnitude as the interatomic distances in solids.

The diffracted electrons are accelerated to a phosphor screen which provides a visible output. This is viewed with a high resolution CCD video camera and the image is stored in a Macintosh Computer by a frame grabber (LG-3, Scion Corporation using Scion-Image 1.54 software as the driver). To improve the image signal-to-noise ratio, 100 one-second images were averaged for each LEED image.

2.2 Photoemission Spectroscopy

2.2.1 Photoemission Spectroscopy (PES)

Photoemission spectroscopy (PES) is based on the principle of the photoelectric effect, the discovery of which earned Albert Einstein the Nobel prize for Physics in 1922. Einstein's explanation of the photoemission phenomenon can be summarized as follows:

$$E = h\nu - \phi \ ,$$

where hν is the incident photon energy with wavelength λ ($\lambda = c/\nu$) and φ is the work function of the metal. The energy E corresponds to the kinetic energy given to the electron by absorbing the energy of the incident photon. The work function is the minimum energy needed to overcome the potential barrier at the surface and escape into vacuum.

Photoemission related research during much of the first half of the 20th century concentrated on understanding work function related phenomena, as well as on developing materials with differing photocathode properties.[24] Throughout the 1960's, experimental techniques and the improvement of vacuum technology progressed in the field leading to the first angle-integrated photoemission spectra from Cu and Ag obtained by Berglund and Spicer.[25] Their first data showed *d*-band edges at 2 and 4 eV, respectively, below the Fermi edge.

Kane, in a landmark publication[26], showed that the band structure of solids could indeed be mapped by angle-resolved photoemission. By the early 1970's, the ability to acquire angular distributions of photoemitted electrons led to the development of the powerful tool of angular resolved ultraviolet photoemission spectroscopy (ARUPS). This technique can be used to provide direct experimental information regarding momentum-dependent electronic bulk and surface band structure of materials.

Laboratory based light sources (He, Ne, Mg, Al, etc) were the primary source of photons in the early days of photoemission research. With the development of synchrotron radiation facilities and monochromators, a continuum of polarized intense radiation became available which greatly enhanced photoemission research.

Photoemission is a technique where photons go in and electrons come out as shown in figure 2.3. The sample is irradiated with photons of a specific energy (hence wavelength). The electrons in the solid absorb the photons and are emitted, as long as the photon energy exceeds the work function (ϕ) of the material (typically ~ 4 - 5 eV or so for most surfaces). The electron kinetic energies depend on how strongly (or weakly) they are bound in the solid. This is described by the energy conservation equation:

$$E_{kin} = h\nu - \phi - E_B, \qquad (2.3)$$

where $h\nu$ is the incident photon energy, ϕ is the work function, E_B is the energy measured relative to the Fermi level (E_F), and E_{kin} is the kinetic energy of the photoelectron relative to vacuum. The usual procedure to assure that all electrons are collected is to apply a small negative bias (~5 eV) to accelerate all electrons to the detector.

The photoelectron spectrometer or energy analyzer measures the number of electrons emitted within a narrow window of kinetic energy. It does so by converting the kinetic energy of the emitted photoelectrons to a fixed energy called the pass energy. This is to ensure that the instrumental resolution and transmission is independent of the electron's original kinetic energy.

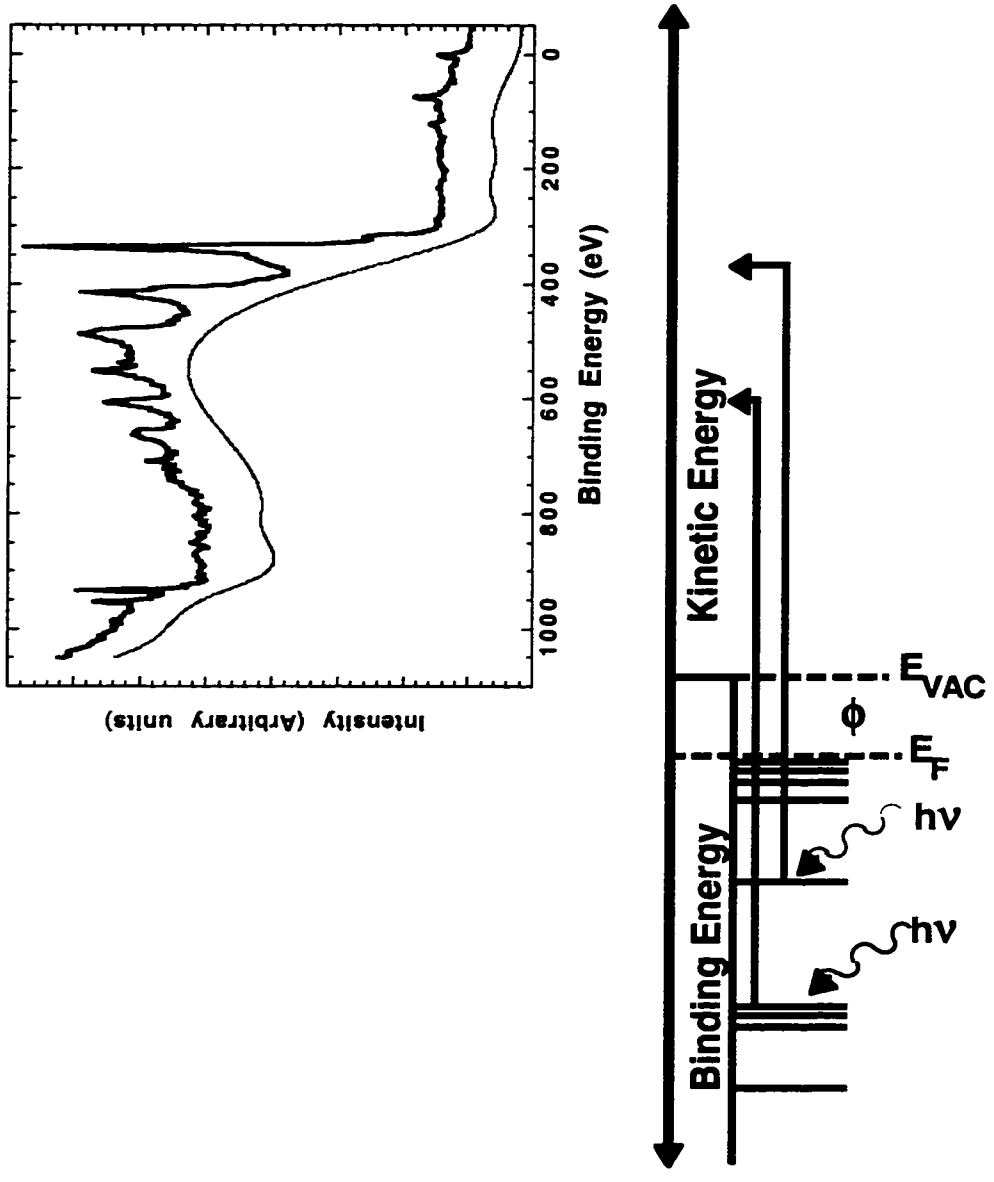

Figure 2.3: Schematic diagram of the transitions involved in X-ray photoemission spectroscopy(XPS). The spectrum is taken for 1.8 ML Fe layer on Cu(100) irradiated with a Mg Kα source.

The window of energy that is selected determines the energy resolution of the measurement. When convolved with the resolution of the incident radiation, the total energy resolution of the spectrometer and excitation source is obtained. Several spectrometers with differing resolutions were used in the work reported here.

The wavevector **k** (from momentum $\boldsymbol{p} = \hbar \boldsymbol{k}$) of the outgoing photoelectron is determined by:

$$E_{kin} = \frac{\hbar^2 k^2}{2m} \qquad \text{or} \qquad k = \sqrt{\frac{2mE_{kin}}{\hbar^2}}, \tag{2.4}$$

From equations (2.3) and (2.4) it can be seen that information about the valence electronic levels in a material (E(**k**)) can be obtained if we know the incident photon energy and if we measure the momentum of the excited electron. Photon energies used in ARUPS experiments normally range between 20 and 200 eV. At large photon energies (for instant a typical laboratory XPS source with hν (Mg Kα) = 1253.6eV), the final states of the photoelectrons sample multiple Brillouin zones. At lower photon energy the full zone might not be sampled. The photo energy range used assures a single zone may be sampled allowing for band mapping.

A photoelectron spectrum is a plot of the number of detected photoelectrons (y-axis), as a function of their kinetic energy (x-axis). Usually the kinetic energy scale is converted to binding energy (using equation (2.3)) with $E_F \equiv 0$. Such a

spectrum or energy distribution curve (EDC) can be compared to the occupied density of electronic states within the solid. The primary peaks that are seen in the spectrum arise from electron transitions from the various energy levels or bands that the electrons occupy. Emission from core levels, which are strongly bound, result in peaks with relatively small energy spread as they are more atomic-like, and those from shallower valence levels are broader due to the solid state effects. These features are all located on top of a background of secondary electrons, which arise from inelastically scattered electrons that escape the solid.

In order to use photoemission to map the energy bands in a solid, one needs not only the electron's energy, but also information regarding the electron's momentum. This can be deduced from the angle that the electron is emitted in with respect to the surface normal. This requires the use of single crystalline samples, since polycrystalline materials consist of different orientations of single crystallites and will yield angle- or momentum- averaged spectra. Relating the photoelectron's energy and momentum to the bands in the solid is discussed below.

2.2.2 Theoretical Description of ARUPS

There are several models used to discuss ARUPS but the three-step model introduced by W. E. Spicer is the most commonly used method.[27] The photoemission process is conceptually separated into three independent steps:

(1) The first step involves the optical excitation of an electron from the initial valence band state, $| i >$, into a final unoccupied band state, $< f |$, within the crystal. Since the photon's momentum can be neglected, only direct (or vertical) transitions are allowed in the reduced zone scheme of the band structure.

We obtain the transition probabilities from first order perturbation theory by coupling the electron to the electric field,

$$W_i \propto < f | \mathbf{A} \cdot \mathbf{p} + \mathbf{p} \cdot \mathbf{A} | i >,$$

where **A** is the vector potential of the incident radiation and **p** is the momentum operator. If we assume that the photon field varies slowly across the dimension of an atom, the second term is equal to the first term, and, the above equation reduces to,

$$W_i \propto < f | \mathbf{A} \cdot \mathbf{p} | i >.$$

By analyzing the emission direction and energy of the final state, $| f >$, we know **k** and E ($E = \frac{\hbar^2 k^2}{2m}$) uniquely and the final state is therefore uniquely defined.[24]. Furthermore, by combining this final state information with the photon's energy and polarization, we can deduce important properties of the initial state $| i >$.

2) The second step is the propagation of the excited electron to the surface/vacuum interface. Photon energies used in ARUPS experiments normally

range between 20 and 200 eV while the light penetrates 100 – 1000 Å. Although the photoemission process takes place throughout this region only a few photoemitted electrons escape the surface due to inelastic losses during electron-electron interactions. The mean-free path λ of the material restricts the information depth, or region from which electrons escape to only a few Å.

3) In step 3 the photoelectron, having traversed the crystal to the sample surface, escapes from the solid into the vacuum. At this point the electron wave packet inside the crystal scatters from the surface potential barrier and becomes a free electron wave function outside the crystal. Boundary conditions require that the wavevector component parallel to the surface be conserved. However, the normal component does change.

The photoelectron's momentum, $\mathbf{k_f}$ (emitted into vacuum) being a vector, may be resolved into two components $k_f^{\parallel}$ and $k_f^{\perp}$ representing the components parallel and perpendicular to the surface. If θ is the polar angle of the photoelectron's trajectory, measured with respect to the sample normal, then

$$k_f^{\parallel} = k_f \sin\theta \quad (2.5), \qquad \text{and} \qquad k_f^{\perp} = k_f \cos\theta. \quad (2.6)$$

From these, we need to determine the electron's momentum inside the solid, $\mathbf{k_{in}}$, in terms of the photoelectron's kinetic energy or equivalently its binding energy

by virtue of equation 2.3. Since the photoelectron is moving in vacuum (free space), its kinetic energy may be written as

$$E_f = \frac{\hbar^2 k_f^{\,2}}{2m}. \tag{2.7}$$

At the vacuum-solid interface, the parallel component of the momentum is conserved:

$$k^{\parallel}_{f(inside)} = k^{\parallel}_{f} \tag{2.8}$$

Therefore,

$$k^{\parallel}_{f(inside)} = \sqrt{\frac{2mE_f}{\hbar^2}} sin\theta\,. \tag{2.9}$$

The perpendicular component of momentum is not conserved as it crosses the potential barrier at the surface and this result in refraction of the electron as it exits the crystal. Mapping this to $k^{\perp}_{f(inside)}$ is not as straightforward. The 'free electron final state' model provides an approach to solving this problem[28].

This phenomenological model assumes that the final state to which the electron is excited in the first step of the three-step model is one that disperses parabolically, regardless of the calculated band structure. This is one way in which one can bring in the effect of the existence of the surface, which is crucial in modeling photoemission. The excitation to a free electron like final state occurs

within the solid. The perpendicular momentum is reduced when passing through the potential barrier at the surface so,

$$k^{\perp}_{f(inside)} > k^{\perp}_{f} \qquad (2.10)$$

$$k^{\perp}_{f(inside)} = \sqrt{\frac{2mE_f}{\hbar^2} + V_o}\cos\theta. \qquad (2.11)$$

where V_o is the inner potential, which usually refers to the binding energy of the bottom of the valence band in metals. For most materials, it is an empirical parameter used to fit the data. Thus equations 2.9 and 2.11 are the central equations used to map energy bands from photoemission.

The next section will deal with a description of the several experimental set-ups and chambers used during this investigation as well as a description of the photoelectron spectrometers used.

2.2.3 Hemispherical Analyzer (HSA)

There are various types of electron spectrometers (analyzers) used to measure the energy distribution of photoemitted electrons as a function of emission angle. The standard analyzer that can be described as the workhorse for photoemission is the hemispherical deflection analyzer shown in figure 2.4.[23]

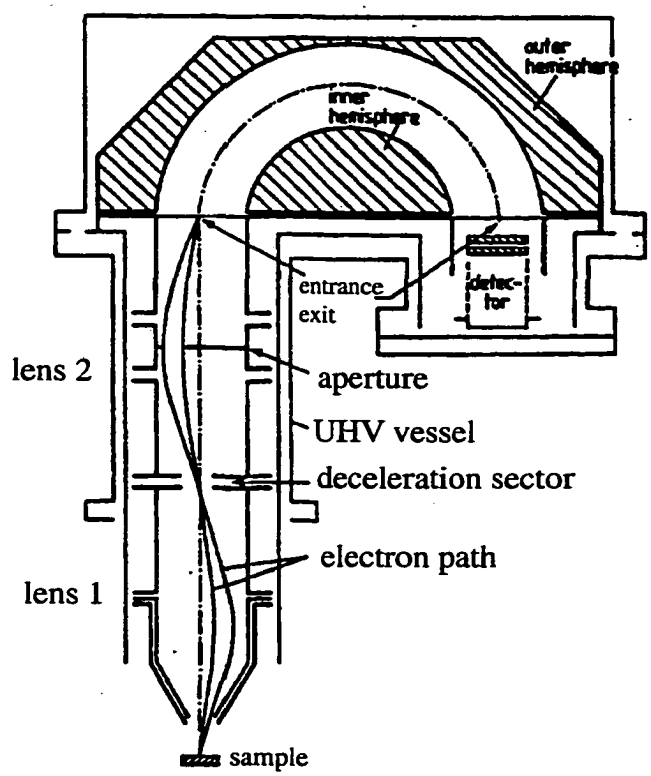

Figure 2.4: Schematic diagram of a hemispherical analyzer for angle-resolved UPS studies. [23]

This analyzer consists of entrance electrostatic lenses which focus the incoming electrons onto the entrance slit, two hemispherical electrodes which energy disperse the beam, and a detector (channeltron). The 180° design enables first-order focussing between the entrance and exit slits.

The typical mode of operation is to set the potential on the inner and outer hemispheres to pass one kinetic energy, E_{pass} (the 'pass energy' = slit potential). This mode is preferred since the electrons leaving the sample with kinetic energy E_k are easily accelerated or decelerated in the lens column without changing their absolute energy spread.

For fixed pass energy, we get a fixed intrinsic energy resolution independent of the kinetic energy. (This resolving power is based on the dimensions of the hemisphere and the pass energy selected.) Because of the electron optics of the lens column, only photoemitted electrons within a small window of (±3°) opening angle are transmitted (angle resolved term in ARUPS) and detected. Depending on the instrumental configuration, the sample or the analyzer is rotated to vary the emission angle of the detected electrons.

We have used analyzers that can rotate using one or two axis goniometers. This allows for the angle of the incoming light to be fixed while the analyzer rotates about the sample normal to extract EDCs at different angles.

2.2.4 Ellipsoidal Mirror Analyzer (EMA)

The ellipsoidal mirror is a display-type analyzer, which performs electron energy analysis while preserving the trajectories of the photoemitted electrons. It is a very unique analyzer and only a handful exist. The EMA in this work was designed and built at the National Institute of Standards and Technology (NIST) by Stockbauer *et al.*[29] Here, the EMA is used primarily for ARUPS where the data is displayed as two-dimensional images of photoelectron angular distributions.

Figure 2.5 shows a schematic of the EMA[29]. It consists of an ellipsoidally shaped electrostatic mirror. This mirror has two foci. The sample is placed at one focal point. When illuminated with radiation, the emitted photoelectrons are selectively reflected off the mirror and are refocused at the other focal point, which is the property of an ellipse. The reflection acts as a low pass energy filter; i.e. only electrons with less than a certain energy reflect off the mirror, with the mirror absorbing energy electrons.

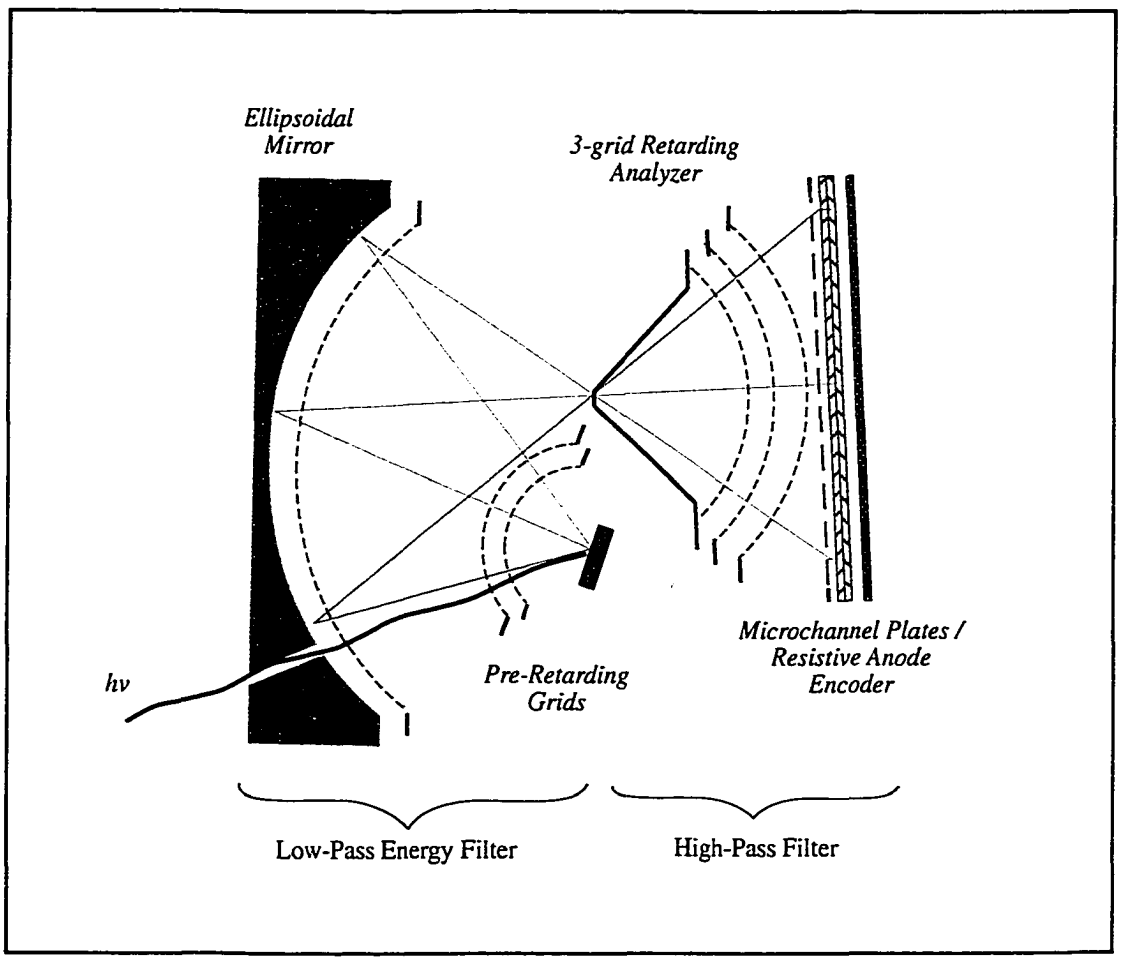

Figure 2.5: A schematic of the Ellipsoidal Mirror Analyzer (EMA). The sample is illuminated with the light and the electrons are emitted from the first focal point of the ellipsoidal electrostatic mirror. The electrons are then refocussed on the other focal point for detection.

The grids at the other focal point act as a high pass energy filter and only allow electrons above a certain energy to pass through. Thus, together, energy analysis is achieved while keeping the angular information intact.

There may be minor distortions in the optics of this instrument. Most of the grids have a spherical curvature, and therefore they can always present a perpendicular surface to the electron trajectories. This helps in not distorting the angular information and keeping the angular distributions intact. The three trajectories shown in figure 2.5 illustrate this. The mirror and G3 are the only components that have ellipsoidal curvature.

The detector consists of microchannel plates coupled to a resistive anode area detector. This consists of a high resistive sheet with uniform resistivity and with four symmetrically placed anodes.

A charge packet incident at any point on this detector produces a charge pulse that is divided among the anodes. The amount of charge reaching each anode depends on the point of impact of the pulse. For example, equal signals at the four anodes imply that the pulse impacted in the center. The actual position is decoded using a position computer and the images are displayed on the computer screen. The raw data are acquired as 16 bit images. The width of the images corresponds to an

angular separation of 64°. This is also shown in figure 2.5. The typical angular resolution is ~2°.

The analyzer can be operated in several modes. One can obtain EDC's by scanning kinetic energy while integrating over all the detected electrons. It is also possible to operate the instrument in an angle-resolved mode, setting the analyzer to detect electrons of a particular kinetic energy and accumulating counts in the form of an image.

The free-electron final state model, described above, relates the angle at which the electron is emitted to the original k-vector within the sample. This means that our image of the angular distribution is a measure of the locations in k-space where transitions occur. Since we image this at a well-defined energy, our image can be related to a horizontal slice through the sample's E(k), its band structure. In fact, this "horizontal slice" is actually a spherical slice through the Brillouin zone with the sphere radius given by $E_{final} = \frac{\hbar^2 k_f^{\,2}}{2m}$.

Conventional hemispherical analyzers measure a spectrum at a fixed angle, or **k**. The binding energy of a peak in that spectrum provides a single point on the band structure. Our imaging technique, however, provides a distinct advantage by

providing many k-values at a single constant energy. This is ideal when a constant energy surface such as a Fermi surface must be determined.

Figure 2.6 shows a cartoon of the Fermi surface of Cu[30]. It consists of a nearly spherical surface in the center fcc Brillouin zone that is connected to similar surfaces in adjacent zones through necks along the (111) direction. The large dark circle in the cartoon represents the free electron sphere. One expects to see four arcs corresponding to emission from adjacent zones. Next to the cartoon in figure 2.6 is the actual data. The contours observed in the image correspond to the intersection of the free electron final state sphere with the initial-state constant energy surface at E_F. This typical image normally takes 15 minutes to acquire. Images such as the one shown in figure 2.6 must be corrected for non-uniformity in the gain of the channel plates and for variations in the transmission of the analyzer.

This is accomplished by taking a background image at an energy where there is no structure in the angular distributions, e.g. where there is only secondary electron emission. Dividing the raw data by this background results in the removal of the non-uniform gain and transmission, thus rendering the true angular intensities. This is the only correction that has been applied to any of the image data.

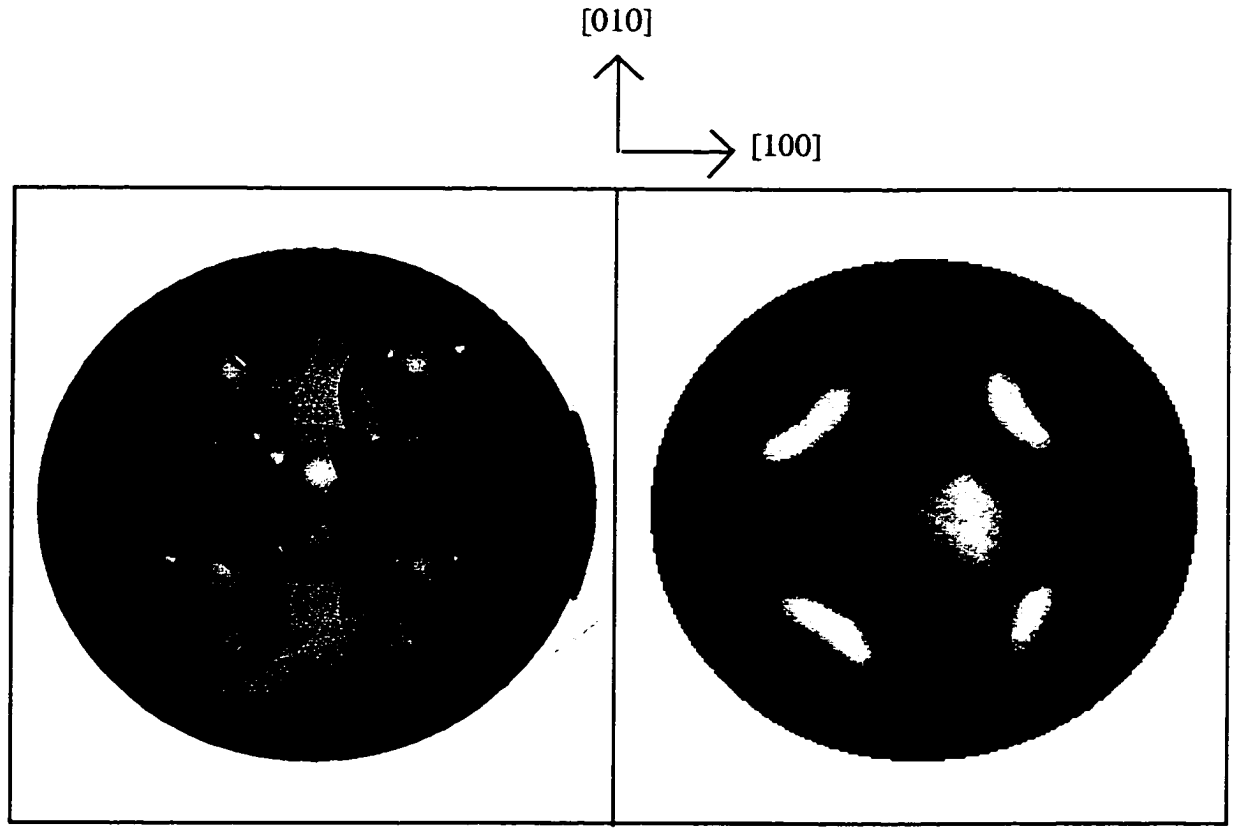

Figure 2.6: A cartoon of the Cu Fermi surface and a 2D image obtained with the EMA. The nearly spherical balls are interconnected throught the necks along the <111> direction. The shaded sphere in the cartoon is the free electron final state sphere for 90 eV photons. The intersection of this sphere with the Fermi surface will give the observed photoemisssion angular distribution. There is very good agreement between the cartoon and the actual data.

The transmission of the analyzer, which is the fraction of electrons emitted in a given energy window that are actually detected, is a strong function of the electron kinetic energy. The grids G1 and G2 allow one to accelerate or decelerate the electrons to the same kinetic energy, called the pass energy. This ensures the same transmission for all the electrons, independent of their original kinetic energy. All the data were acquired using a pass energy of 25 eV. The energy resolution of the instrument is ~ 250 meV for the settings we used. The ultimate resolution is ~90 meV.

2.3 X-Ray Absorption Spectroscopy (XAS)

Absorption spectroscopy is a popular experimental technique used at synchrotron radiation facilities. This is because the setup of an absorption experiment is rather simple, and a wide variety of information can be obtained from many types of samples. The absorption process itself is well understood, and theories describing the observed features in absorption spectra are well established.[31]

The absorption of X-rays in a material as a function of depth (x) follows an exponential decay as

$$I(x) = I_0 e^{-\mu x}.$$

The mass absorption coefficient (sometimes called the extinction coefficient) $\mu(h\nu)$ of X-rays decreases with increasing photon energy. Furthermore, at the absorption edges (*K, L, M*, etc.) where the photon energy reaches the ionization energy of a particular atomic shell, photoelectron production increases and a steep enhancement of the absorption occurs. This jump in absorption is called an "absorption edge."

X-ray absorption spectroscopy can be used to analyze elemental composition of materials since the electron binding energies are different for different elements. Apart from information about elemental composition, absorption spectra also contain information about the chemical environment of a particular element. This results from the influence of the chemical environment on the electron binding energy[20] which translates into a shift of the absorption edge.

Absorption spectra can either be recorded using a transmission or a total yield setup. The transmission method requires special thinning of the sample in order to transmit the X-rays. (Experimentalists use similar techniques to get the samples thin enough as those used for transmission electron microscopy (TEM)).

The total electron yield (TY) method is preferred, it being experimentally the simplest absorption technique since it does not require difficult sample preparation.

2.3.1 Properties of X-Ray Absorption Spectroscopy

In an absorption process the incident photon is absorbed by depositing its energy into the electronic system, which it excites from its initial state $|i\rangle$ to the final state $|f\rangle$ as shown in figure 2.7. Energy conservation gives:

$$E_f - E_i = h\nu$$

with $h\nu$ the photon energy, E_i and E_f the total energy of the electronic system before and after the absorption of the photon. The transition probability (per unit time) follows from Fermi's Golden Rule: [32]

$$W_{i\to f} \propto \frac{2\pi}{\hbar} \left|\langle f|H'|i\rangle\right|^2 \delta\left(E_f - E_i + h\nu\right),$$

where H' is the perturbation Hamiltonian of the interaction between a photon field and the electrons, i.e.,

$$H' \cong -\frac{e}{2mc}(\boldsymbol{p}\cdot\boldsymbol{A} + \boldsymbol{A}\cdot\boldsymbol{p}) + \frac{e^2}{2mc}\boldsymbol{A}\cdot\boldsymbol{A} \cong -\frac{e}{2mc}(\boldsymbol{p}\cdot\boldsymbol{A} + \boldsymbol{A}\cdot\boldsymbol{p}) \cong -\frac{e}{mc}\boldsymbol{A}\cdot\boldsymbol{p}.$$

In the above approximations, we have assumed that the diamagnetic $\boldsymbol{A}\cdot\boldsymbol{A}$ term which changes the number of photons by 0 or ± 2, can be neglected in lowest order since in a single absorption process just one photon is absorbed. Furthermore, $\boldsymbol{p}\cdot\boldsymbol{A} = \boldsymbol{A}\cdot\boldsymbol{p}$ if we assume that the photon field varies slowly across the dimension of an atom.

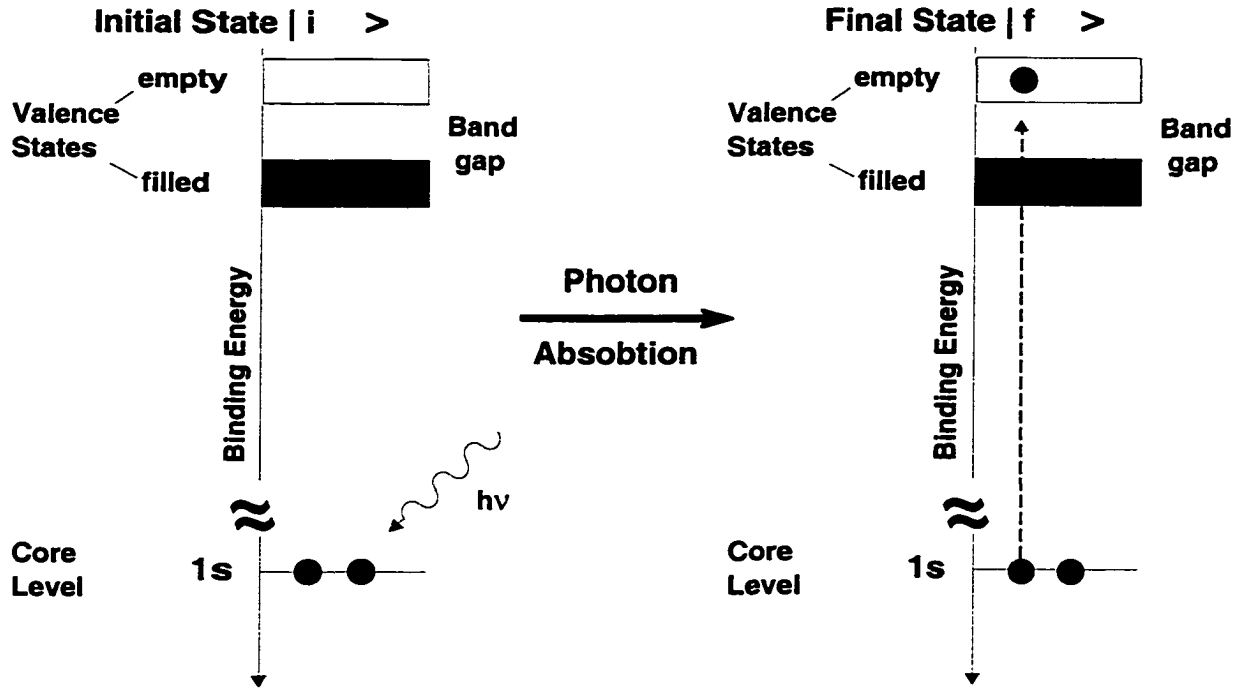

Figure 2.7 Principle of an X-Ray absorption process. The initial and final state of the electron is shown before and after the absorption of the photon.

For solids we can use another important physical assumption that electron-electron interactions can be neglected. This is called the single-electron approximation. Within the single-electron picture the incident photon is absorbed by a single electron i with the one electron wavefunction $|\psi_i\rangle$, and the electron is excited into an unoccupied state f with the one electron wavefunction $|\psi_f\rangle$.

The photoabsorption intensity inside the crystal can be written as

$$I(E,h\nu)=\sum_{fi}|M_{fi}|^2\,\delta\left(E_f-E_i+h\nu\right),$$

where the transition matrix is given by $|M_{fi}|^2 \propto |<f|\boldsymbol{A}\cdot\boldsymbol{p}|i>|^2$.

Radiative transitions are governed by the *dipole selection rules.*[32] The selection rules for the principal (n), orbital angular momentum (l), spin (s), magnetic (m_j) and total angular momentum (j) quantum numbers are the following:

Δn *is not constrained,*

$\Delta l = \pm 1$,

$\Delta s = 0$,

$\Delta j = 0$ *or* ± 1 *and*

$\Delta m_j = 0$ *or* ± 1.

Table 2.1 gives the notation used for X-ray spectra.

Table 2.1: Notation used for X-ray spectra.

X-Ray Notation	Atomic Notation
K	$1s_{1/2}$
L_1	$2s_{1/2}$
$L_{2,3}$	$2p_{1/2,3/2}$
M_1	$3s_{1/2}$
$M_{2,3}$	$3p_{1/2,3/2}$
$M_{4,5}$	$3d_{3/2,5/2}$
N_1	$4s_{1/2}$
$N_{2,3}$	$4p_{1/2,3/2}$
$N_{4,5}$	$4d_{3/2,5/2}$
$N_{6,7}$	$4f_{5/2,7/2}$

In NEXAFS two selection rules follow from the involvement of a localized core electron in the absorption process:

(a) The core electron can only be excited to the conduction band states, which have a non-vanishing wavefunction amplitude locally in the surroundings of the atomic site of the core hole. This means that photo-absorption probes the *local* density of states (DOS).

(b) The core electron has a well-defined angular momentum with respect to its atomic site. Without electron correlation effects the dipole transition can only alter the angular momentum l of a core electron, i.e., the dipole selection rule is given by

$$\Delta l = \pm 1 \text{ and } \Delta m = 0, \pm 1,$$

with m the projection of the angular momentum on the quantization axis. As a consequence, only band states can participate in the absorption process which have a well-defined (angular momentum) symmetry character relative to the angular momentum of the core state. This means that photo-absorption probes the *partial* DOS of a certain local symmetry character. In other words, the X-ray absorption process is a local projection of the band states on the angular momentum symmetry of the core state resulting from the angular integration of the dipole transition matrix element. Therefore, it makes sense to speak of a local s, p, or d character of the band states although these states are Bloch states, i.e., they are delocalized over the whole crystal and are periodic with respect to the crystal structure.

By evaluation of the dipole transition matrix element we get that for an initial s-symmetric core state, only states of local p symmetry can contribute to the absorption process. Furthermore, for an initial p-symmetric core state, only states of local s and d symmetry are involved.

2.4 Experimental Detail

The following section will describe the various experimental set-ups used in this investigation. This includes the various chambers, energy analyzers as well as the beamline at the Center for Advanced Microstructures and Devices (CAMD) synchrotron source.[33]

2.4.1 Center for Advanced Microstructures and Devices (CAMD)

Our initial set of photoemission data was taken at LSU's Surface Science laboratory that is located in the Physics Department. Those preliminary photoemission measurements were followed by more detailed studies performed at Louisiana State University's (LSU's) CAMD synchrotron source[33]. The CAMD storage ring has a diameter of ~55 feet and consists of 8 bending magnets, each of which can accommodate two beamline ports. The bending magnet radius is 2.928 meters. The typical operating energy for the ring is 1.3-1.5 GeV.

Storage currents are ~ 150 mA and current lifetimes ~11 hours. The critical wavelengths are ~4 Å and ~7 Å for energies of 1.3 GeV and 1.5 GeV, respectively.

Synchrotron radiation is the light produced when relativistic electrons are accelerated. This occurs in the field of the bending magnets of the synchrotron storage ring. The radiation that is produced is plane polarized in the plane of the

electron's orbit. As one deviates above or below this plane, the radiation is elliptically polarized.

The experiments were performed using several ultra high vacuum (UHV) end-stations on LSU's Plane Grating Monochromator (PGM) beamline[34]. The PGM beamline was designed to monochromatize plane-polarized light from the synchrotron storage ring and deliver it to the user at the end station. This beamline is located in port 4A of the CAMD synchrotron. It has two gratings which cover the range from 20 eV - 700 eV. The measurements presented here were all acquired using both the lower energy grating of 360 lines per mm (20 - 180 eV) as well as the higher energy grating of 1221 lines per mm (200 - 700 eV). The beamline was operated at a resolving power of ~ 1500 and the beam spot size at the end station was typically 0.5 mm.

2.4.2 Experimental Setups

This section will describe the experimental setup, substrate preparation and the techniques used to grow the thin films. Photoemission and photoabsorption data were collected with three separate instruments as indicated in figure 2.8. Figure 2.8 a) shows our physics department instrument consisting of a main chamber that houses a 50-mm hemispherical analyzer.

(a)

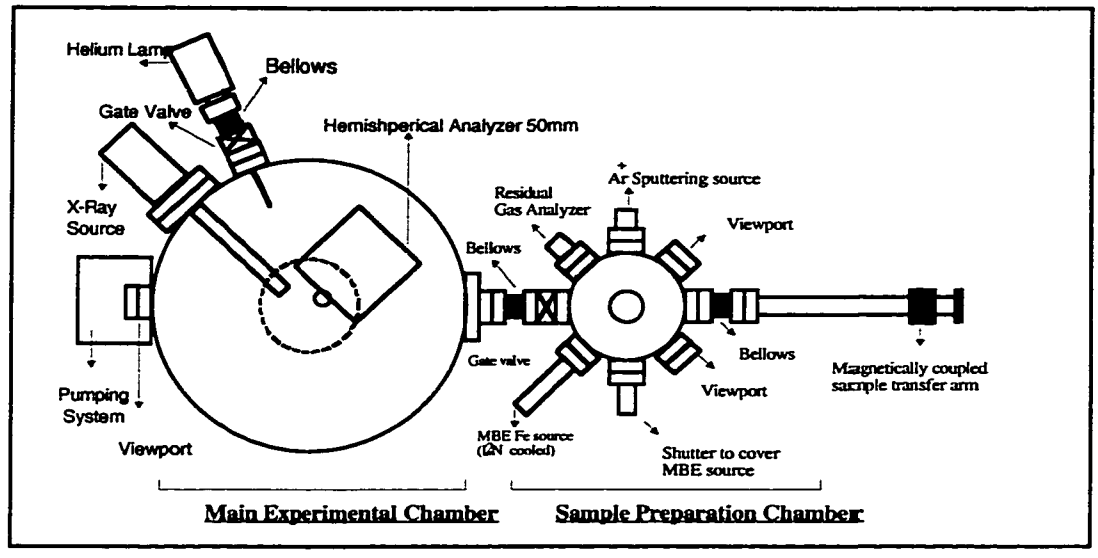

(b)

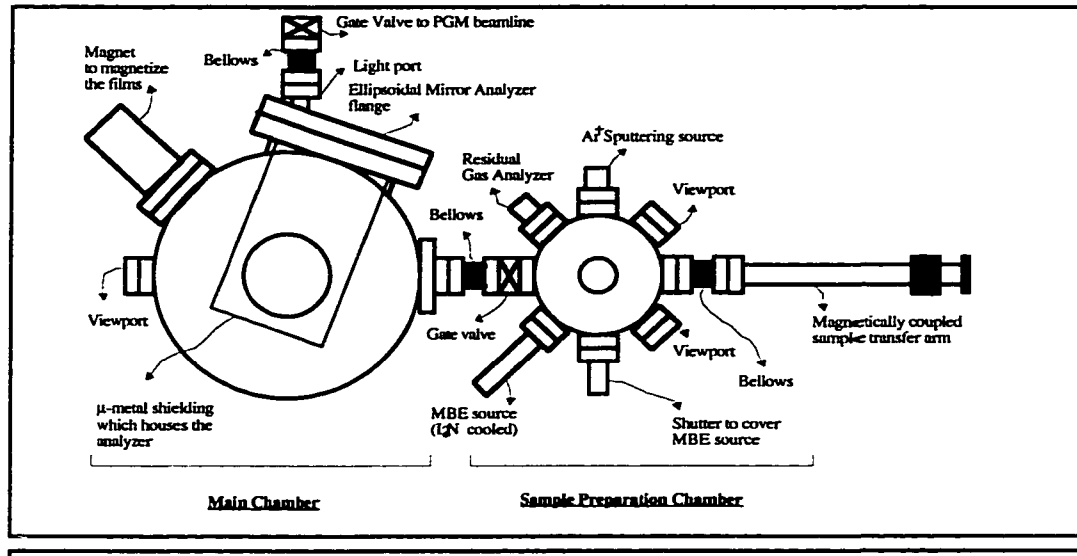

(c)

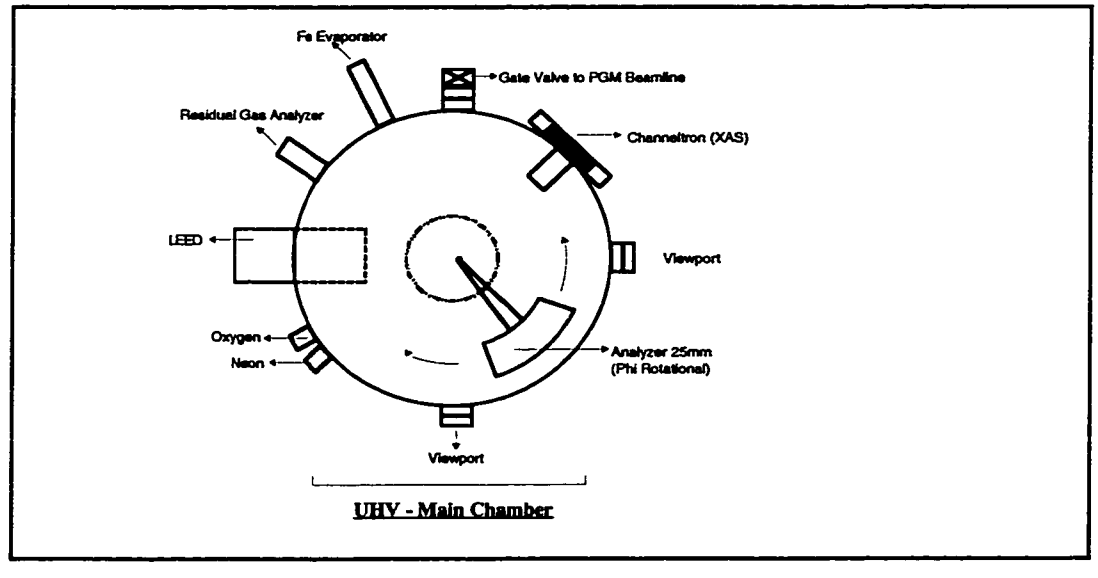

Figure 2.8: The three UHV chambers that were used in this investigation.

The analyzer was mounted on a 2-axis goniometer that enabled us to vary the detection angle of the photoemitted electrons.

The sample was mounted on a manipulator that enabled us to rotate the sample about the manipulator's axis for ARUPS measurements. The X-ray source and the He resonance lamp that was used for the photoemission (XPS and UPS) measurements are also shown on the diagram.

The sample preparation chamber that is connected to the main chamber through a gate valve, houses all the equipment needed for cleaning of the crystal (sputtering and annealing) as well as a MBE source to evaporate Fe films on the Cu substrate. A magnetically coupled transfer arm allows the transfer of samples between the preparation and the analysis chamber. The isolation of the analysis chamber from the film growth process prevents the coating of the optics and deterioration of the vacuum in the spectrometer.

The base pressure in the main chamber was below $1x10^{-10}$ Torr and that in the preparation chamber was better than $1x10^{-9}$ Torr during film deposition.

Figure 2.8 b) shows the EMA chamber that is connected to the PGM beamline at CAMD. The EMA is magnetically shielded by 3 layers of mu-metal to reduce the influence of stray magnetic fields on the electron trajectories. The preparation chamber is identical to the one described above in figure 2.8 a).

The third chamber used in this investigation houses both characterization tools (energy spectrometer and LEED optics) as well as the sample preparation equipment. It is a two-level system with the top portion used for sample preparation while the bottom part, housing a 25-mm hemispherical analyzer, is used for photoemission. It also houses a channeltron detector that was used to perform NEXAFS measurements. The hemispherical analyzer in this chamber was mounted on a 2-axis goniometer that enabled us to vary the detection angle of the photoemitted electrons.

A retractable rearview LEED optics was mounted in this chamber which allowed us to characterize the sample before and after oxidation without moving the sample.

2.5 Thin Fe/Cu(100) Film Growth and Oxidation

A high purity (99.99%) commercial Cu(001) crystal was initially prepared by mechanical polishing followed by electrochemical polishing. The crystals were sputtered for ~30 minutes with 500 V Ar^+ ions at a pressure of $5x10^{-5}$ Torr.[35] This atomic-scale 'sand-blasting' cleans the surface of adsorbed contaminants and any previously deposited film.

A sputtered surface, however, is not smooth on the atomic level as Karunamuni showed with his STM images.[36] For Cu under our conditions, pits up to 500 Å across and hundreds of Å deep are formed. These pits were removed by annealing for ~10 minutes at ~ 600°C. The annealing increases the mobility of the atoms on the surface and redistributes the atoms to render a flat surface with monoatomic steps and terraces 100's of Å wide. The substrates were subjected to several sputtering and anneal cycles every day.

The Cu crystal was periodically rechecked by LEED for surface crystallinity and periodically it was repolished mechanically to remove roughening that arises over time after several cycles of Fe deposition. Cycles of oxidation at elevated temperature also resulted in surface roughness and this also resulted in additional time required for surface cleaning.

Mechanical polishing (0.5μm grit) was followed by electropolishing in a solution of 25% hydrochloric acid and 75% phosphoric acid[37]. The crystal, suspended on pure Cu holder, serves as the anode (+), while a pure Cu plate serves as the cathode (-). The electropolishing is performed for 30 seconds at a voltage of 2.1V and then the crystal is thoroughly rinsed with distilled water. This helps to restore the bright copper color of the crystal surface, which turns hazy due to roughening.

2.5.1 Thin Film Growth on Cu(100)

The Fe thin films were grown in ultra-high vacuum using molecular beam epitaxy (MBE) from an e-beam heated wire. The evaporator used here was designed, constructed and assembled in-house for this purpose. An iron rod, 1mm in diameter, was placed along the axis of a hollow cylindrical Cu cooling block. A concentric filament was placed around the tip of the Fe rod. By passing ~ 5 - 6 amps of current through the filament, and biasing the Fe rod to +2kV, the tip was heated by the thermionically emitted electrons, which bombarded the Fe rod, resulting in heating and evaporation. A collimating aperture was used to guide the flux of Fe to the substrate. The Cu block was cooled using flowing liquid nitrogen to keep the pressure increase in the chamber at a minimum during deposition. Typical evaporation rates were ~1-5 ML per minute.

During deposition, the ion current to the substrate was monitored and was observed to be ~1 nA. The product of the evaporation time and this ion current was used as a rough indicator of the film thickness. We also mounted a quartz crystal oscillator to monitor evaporation rates. Core level spectra of the overlayer and substrate may also be used to determine the film thicknesses. As the film thickness increases, the intensity of the substrate peak decreases as the emitted electrons are attenuated by the overlayer. The ratio of the intensities of the corresponding

overlayer core level peaks to those of the substrate can be used to estimate the film thickness as described in Chapter 3 using the Fe 3*p* peaks.

2.5.2 Oxidation Procedure

During the oxidation, the Cu crystal, mounted on a sample transfer puck, was heated from the back by electron bombardment. The temperature of the filament was electronically stabilized so that the sample temperature could be held constant to $\pm$ 2K. The chamber was filled with oxygen to 1 x 10^{-6} Torr at room temperature and simultaneously the sample was heated slowly to 810K and maintained at this temperature for 3-5 minutes. It was then cooled slowly (0.5 degree per sec) to 500K, at which point the heating was switched off and the sample was allowed to cool to 300 K. During cooling, the oxygen exposure was stopped when the temperature cooled to 550K. The oxidation procedure described above was used in the first and second experimental setups described in figure 2.8. Heating during the oxidation procedure in the third chamber was accomplished by resistively heating the sample. Here, the sample was electrically isolated and a current of ~30 A passed through it. To measure the temperature of the sample, a W-5% Re / W-26% Re thermocouple was spot welded to the holder very close to the sample.

Chapter 3

Ultrathin Fe Films Deposited on Cu(100)

In atomically-thin metal-on-metal films, crystal structures that are not normally accessible in bulk materials or at room temperature can often be stable. While bulk Fe is bcc, Fe films grown on Cu(100) forms an fcc-like phase at low film thicknesses and this new structure and different atomic volume give rise to interesting magnetic phenomena.[37]

Several studies indicate that the formation of ultrathin layers of Fe on the Cu(100) substrate is pseudomorphic.[38, 39, 40] For thicknesses beyond10 ML it reportedly reverts to bulklike bcc-Fe.[41] Fcc-Fe and fcc-Cu have lattice constants of 3.58 Å and 3.61 Å respectively.[42] Previous studies of Fe/Cu(100) system indicated that the small ~1% lattice mismatch results in a tetragonally distorted film on the fcc Cu(100) substrate at low Fe coverage.[41] This tetragonal distortion is a result of the tensile stress, causing the z-dimension to compress.

Although the precise growth mode depends on deposition technique, ultrathin Fe films grown epitaxially on Cu(100) at room temperature have been observed to exhibit both layer-by-layer growth as well as a small amount of 3-D islanding.[39, 41, 43] The e-beam deposited films which exhibit a deviation from layer-by-layer growth, are shown by medium energy electron diffraction studies to exhibit some second layer growth before the first layer is complete.[38] Scanning tunneling microscopy (STM) studies showed that nucleation and growth of the second ML of Fe starts from a total coverage of about 0.5ML.[41, 44] These observations are consistent with our own STM studies. At thicknesses above 2 ML the growth appears to be layer-by-layer.

Several experiments have indicated that structural and magnetic transitions in Fe/Cu(100) occur at different film thicknesses.[38, 39, 41, 44] From 0 to about 5 ML the MBE-grown Fe films are ferromagnetic (FM) with a tetragonally distorted fcc structure, corresponding to an increased atomic volume of ~6%.[38, 39, 40] At 5 ML, there is a precipitous drop in the perpendicular magnetization, which is thought to reside in a magnetically "live" surface layer. From 5 to 11 ML the Fe film is undistorted fcc and, except for the surface "live" layer, is theoretically predicted to be antiferromagnetic (AFM). For Fe coverages of more than 11 ML, fcc Fe becomes unstable and transforms into bulk FM bcc Fe.[38]

The sensitivity of the fcc Fe moment to atomic volume was investigated by Bagayoko and Callaway who found that the electronic band structure, and hence magnetic moment, depended critically on atomic volume.[45] At larger Wigner-Seitz radii, they found that the exchange splitting increased, with an increasing occupancy of a significant portion of the *d*-electron majority-spin bands. Recent total energy calculations for various configurations of the spin orientations in multilayer Fe found that the equilibrium magnetic structure depends critically on volume and symmetry, with several different FM and AFM configurations in close energetic competition.[46] Asada and Blügel conclude that of all possible collinear spin configurations of single layers of fcc Fe on Cu(100), 1-3 ML fcc Fe are FM while thicker layers have AFM-coupled bilayers of parallel orientation. With an odd number of layers, the top layers' magnetization gives the film a net moment.

3.1 LEED Results from Fe/Cu(100)

As described in the previous chapter, we can employ low energy electron diffraction to obtain structural information about the substrate surface as well as the overlayer on top of it. All the LEED data described below were taken in chamber 3 at CAMD.

Figure 3.1a) shows the LEED pattern of a clean Cu(100) surface that was taken with a beam energy of 82 eV.

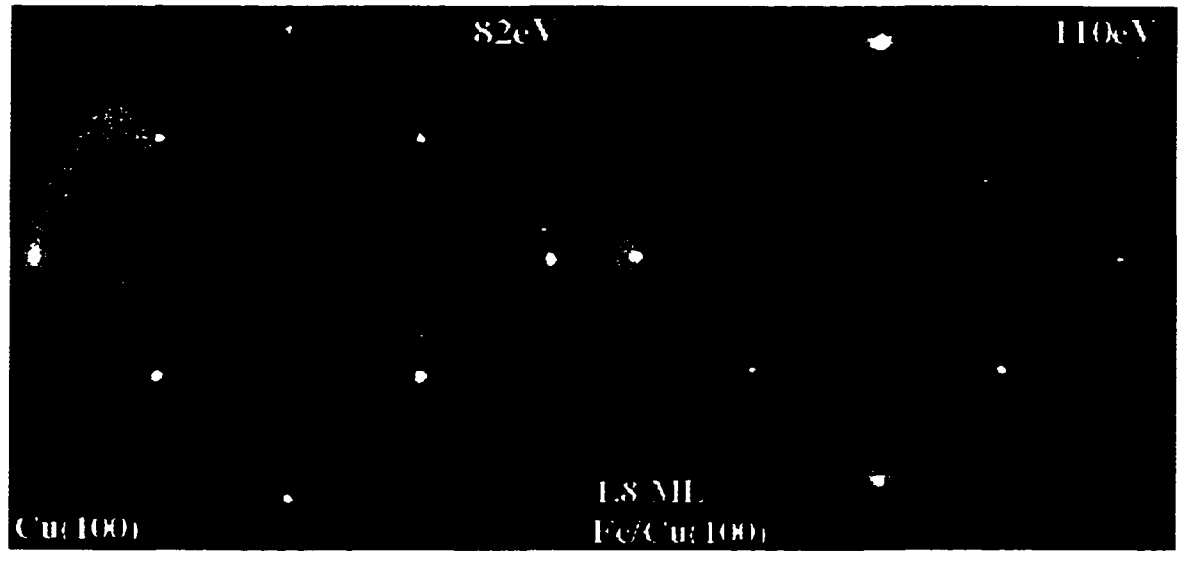

(a) (b)

Figure 3.1:(a) LEED pattern of clean Cu(100) taken at normal incidence with a beam voltage of 82 eV. (b) The LEED pattern of 1.8 ML Fe on Cu(100) at 110 eV, remains virtually unchanged (1 x 1).

In figure 3.1b) the Cu(100) LEED pattern remains virtually unchanged (1 x 1) with deposition of up to 1.8 ML Fe onto the substrate, indicating that the growth of Fe on the Cu(100) substrate is pseudomorphic. This means that the usual bcc-Fe is growing as fcc-Fe on Cu(100). For thicknesses greater than 10 ML it reportedly reverts to bulklike bcc-Fe.[41] As we increase the Fe coverage, the LEED pattern becomes more diffuse but remains (1x1).

Previous studies of Fe/Cu(100) system indicated that the small 1% lattice mismatch results in a tetragonally distorted film on the fcc Cu(100) substrate at low Fe coverage.[41] This small mismatch and distortion, in part, produces the blurring of the LEED pattern for Fe/Cu as compared to the sharp Cu(100) pattern.

3.2 Photoemission Studies on Fe/Cu(100)

Electron energy levels of an atom can be divided into two types: core levels, which are tightly bound to the nucleus, and valence levels, which are only weakly bound. The binding energies of the core levels [20] depend on the chemical species and on the oxidation state, giving well-characterized chemical shifts. In the creation of a chemical bond, the valence electrons of an atom interact with the valence electrons of other atoms forming new compounds.

We can characterize the new material by measuring the valence electronic structure. Furthermore we can get additional clues into the nature of the bonding by monitoring how this new valence state impacts core-electron binding energies through their chemical shifts.

In this section we describe how UPS was used to study the evolution of the valence band structure of ultrathin Fe films deposited on Cu(100) as a function of increasing Fe coverage in the 0-12 monolayer range. We used X-Ray Photoelectron Spectroscopy (XPS) to look at the core levels of the Fe/Cu(100) system. Angle-resolved photoemission was used to probe the valence electronic structure and to extract Fermi surface contours as a function of increasing Fe coverage.

3.2.1 Core-level Photoemission

As mentioned in chapter 2, the kinetic energy (E_k) of the electron depends on the energy of the photon hν as expressed by the Einstein photoelectric law:

$$E_k = h\nu - E_i - \phi, \qquad (3.1)$$

where the initial energy (E_i) is the energy of the particular electron in the atom.

Since we can use a specific photon energy (determined by the X-ray source) to probe our sample, we can measure the kinetic energy and calculate the binding energy. The core-level binding energies thus provide unique signatures of the relevant energies. The binding energies in electron volts (eV) for various electronic levels in Cu and Fe are provided in figure 3.2.

XPS spectra for three coverages of Fe/Cu(100) are given in figure 3.3. They were obtained with a Mg K_α x-ray source producing X-rays with a photon-energy of 1253.6 eV. The shapes of the three spectra are typical for XPS data.

The core-level and Auger peaks sit on a background that is due to inelastically scattered electrons and this is indicated schematically below the 1.8 ML curve. These data are surface sensitive since electrons in XPS can travel only short distances through the solid before losing energy due to collisions, so that only near-surface electrons escape unscattered.

The 1.8 ML Fe/Cu(100) spectra in figure 3.3 shows the presence of relatively large Cu 2*p* peaks as well as Cu Auger peaks. The Auger peaks are due to the recombination of core holes with valence electrons and are a "by-product" of core level photoemission.

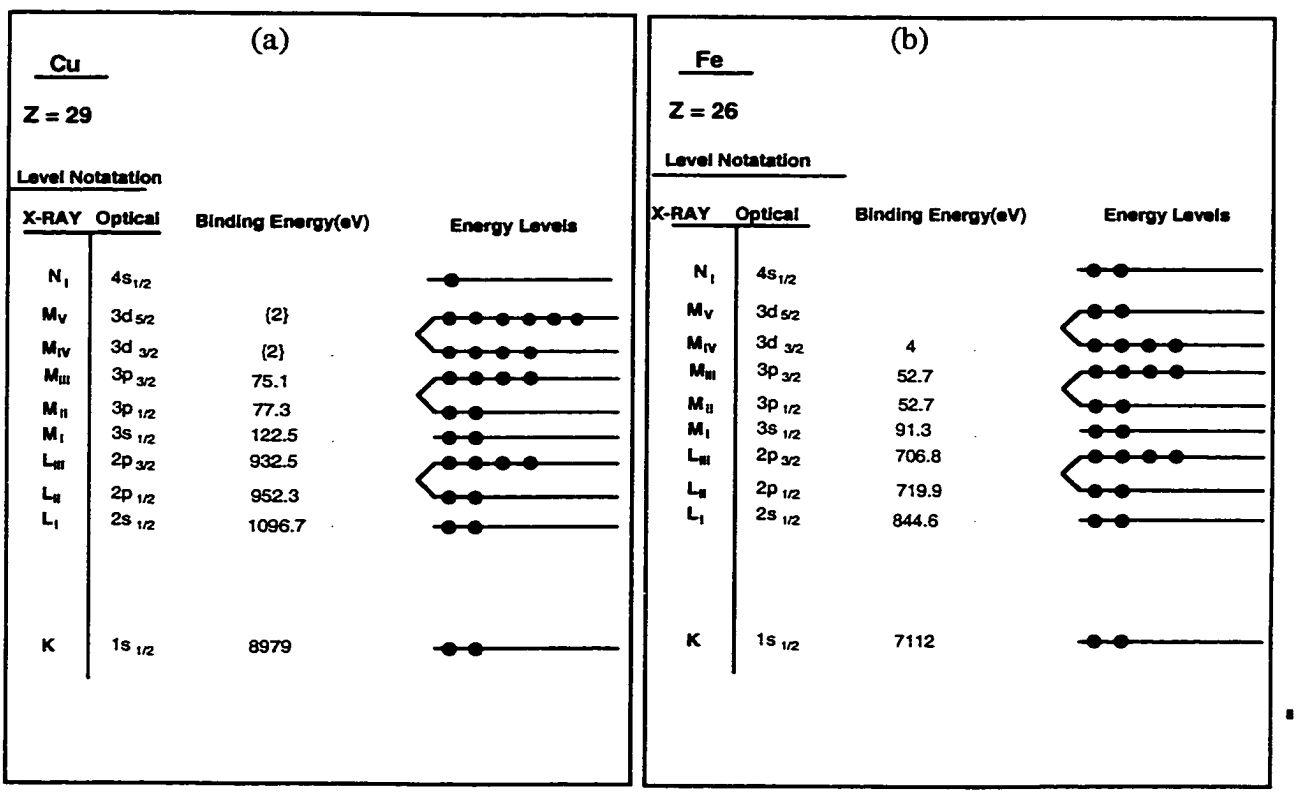

Figure 3.2 Schematic (not to scale) of Energy level diagrams for (a) Cu and (b) Fe

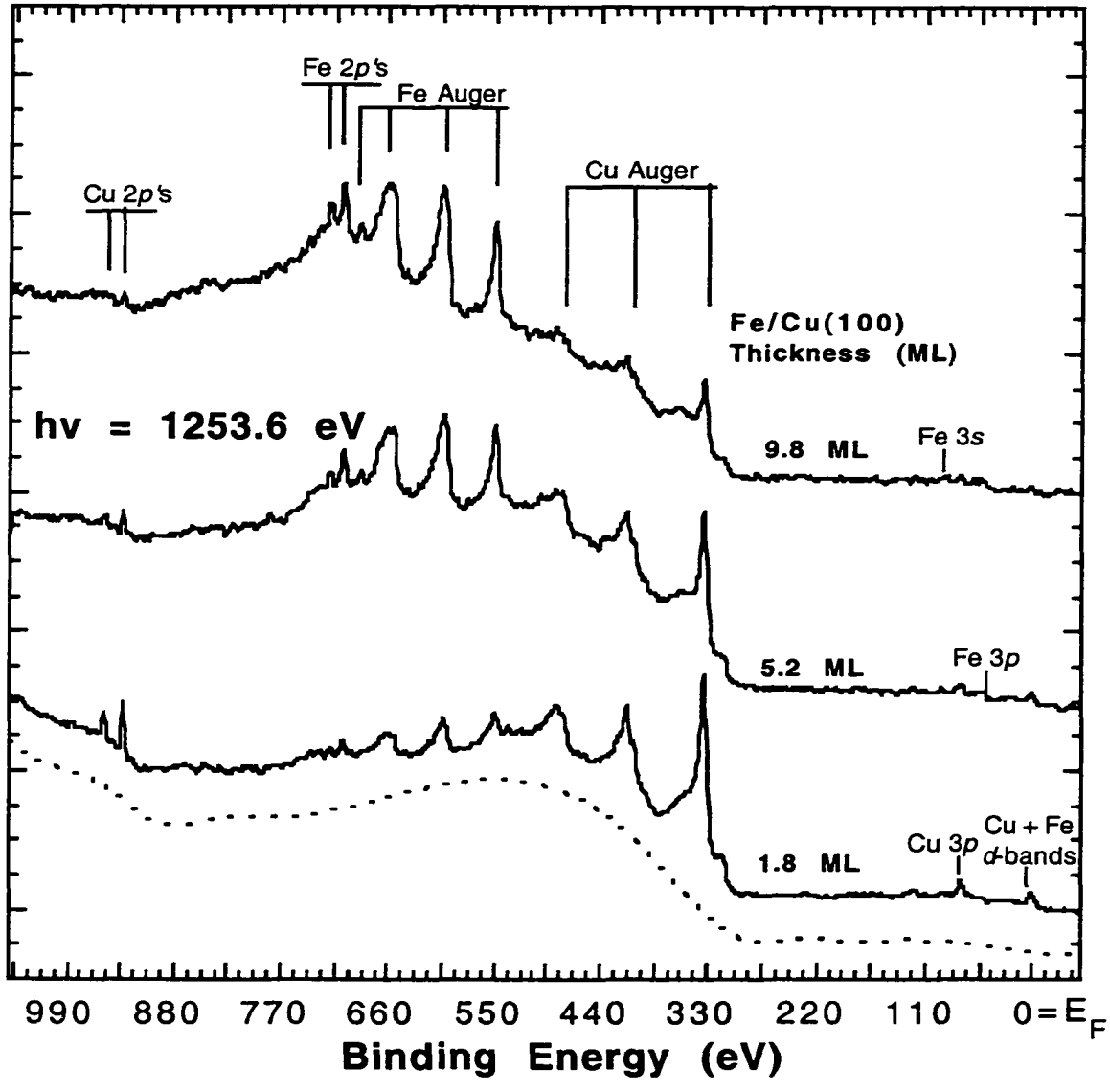

Figure 3.3: XPS spectra of Fe deposited on Cu(100) as a function of thickness, taken with a Mg K_α X-Ray source giving hν=1253.6 eV. The Cu and Fe $2p_{1/2}$ and $2p_{3/2}$ core-levels are visible; however, the Fe overlayer thickness determines the intensity of these peaks. The intensity of the Fe 2*p* and Auger peaks increase considerably compared to the Cu 2*p*s and Cu Augers for higher Fe coverage.

They arise from the core-hole left behind after photoemission being filled by an electron dropping down from a higher lying orbital. Conservation of energy requires that the excess energy be removed by ejecting another electron. The value of the Auger kinetic energy is characteristic of the atomic energy levels involved and therefore provides a direct elemental identification.[20] Also present in the 1.8 ML spectrum, are lower intensity Fe 2*p* and Fe Auger peaks. At binding energies below 300 eV, some of the valence bands can be observed, but their intensities are extremely low due to a low cross-section at this high photon energy. As the coverage of Fe increases (5.2 ML and 9.8 ML), we observe that the intensities of Cu 2*p* and Auger peaks decrease dramatically while the intensity of the Fe 2*p* and Fe Auger-electrons increase.

3.2.2 Thickness Measurement: Attenuation of 3*p* Levels

One of the most important measurements in film characterization is the film thickness. Film growth rates were estimated during deposition using a water-cooled quartz crystal oscillator. This provided a rough estimate of the film thickness. Several photoemission techniques were employed to provide a quantitative measure. Core level spectra of the overlayer and substrate may be used to determine the film thicknesses. As the film thickness increases, the intensity of the substrate peak decreases as the emitted electrons are attenuated by the overlayer. The ratio of the

intensities of the corresponding overlayer core level peaks to those of the substrate can be used to estimate the film thickness, using Beer's law.

Let I_{Fe} and I_{Cu} be the intensities of the Fe and Cu core level peaks respectively. Then

$$I_{Cu} = I_{0(Cu)} e^{-d/\lambda}, \tag{3.2}$$

where I_o is the total photoemission intensity, d is the film thickness and λ is the inelastic mean free path in Fe. Correspondingly, I_{Fe} is given by

$$I_{Fe} = I_{0(Fe)}(1 - e^{-d/\lambda}). \tag{3.3}$$

Solving for d from the above two equations gives

$$d = \lambda \ln\left[1 + \frac{(I_{Fe} / I_{0(Fe)})}{(I_{Cu} / I_{0(Cu)})}\right] \approx \lambda \ln\left[1 + \frac{I_{Fe}}{I_{Cu}}\right]. \tag{3.4}$$

The thicknesses may be estimated from the ratio of the peak intensities from the core level spectra, providing the value λ, the inelastic mean free path is known. The electron inelastic mean free path (IMFP) in solids fall on a so-called universal curve, roughly independent of the material[47]. It depends only on the electron's

kinetic energy and has a minimum of 3 - 5 Å. For electrons of ~100 eV kinetic energy, $\lambda \sim 5.6$ Å, which translates to about 2.7 ML for the system of interest.

Figure 3.4 shows the angle-integrated EDC's for emission from the 3*p* core levels of Fe and Cu using 165 eV photons for several different Fe coverages. The uniform and almost complete attenuation of the Cu 3*p* peak indicates that there is little or no interdiffusion or alloying between the two species. The film thicknesses were estimated using equation 3.3 and assuming $\lambda = 2.7$ ML. These were consistent with estimates from the rate monitor.

3.2.3 Valence Band Photoemission

Angle–integrated photoemission curves for varying thicknesses of Fe/Cu(100) are presented in figure 3.5 with hv=90 eV. The bottom curve shows the spectrum for clean Cu, which has a low density of sp-like states at the Fermi level, $E_F = 0$. The Cu 3*d*-electron bands give the prominent peak between 2 and 5 eV binding energy.

When Fe films are deposited several changes occur. An enhanced DOS appears at E_F, corresponding to Fe 3*d*-electrons. The Cu *d*-band is attenuated and completely disappears in the thickest films. The spectra from the 15 ML films are essentially identical to those from bulk Fe.

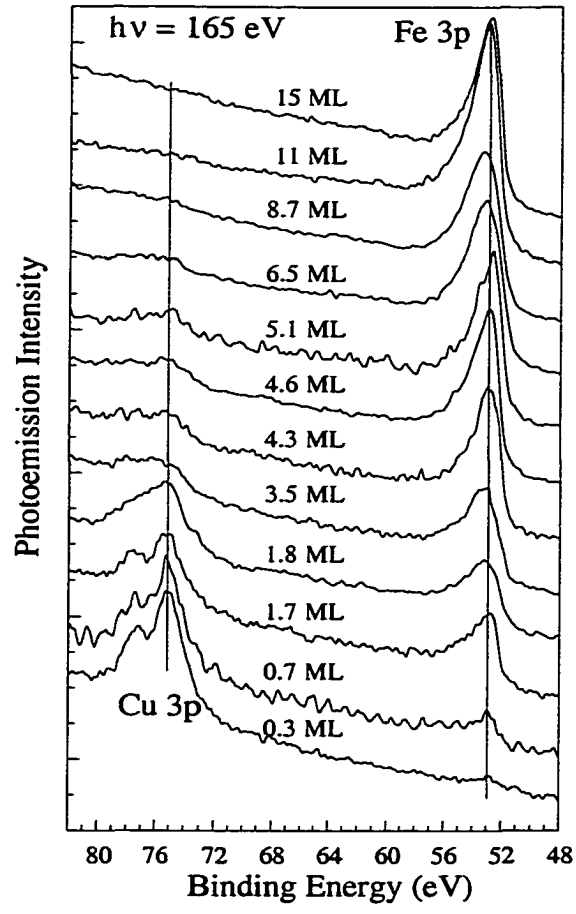

Figure 3.4: Photoemission spectra at hν = 165 eV for Fe films on Cu(100). The $3p_{1/2}$ and $3p_{3/2}$ spin-orbit splitting is clearly visible for the Cu at 77.3 eV and 75.1 eV respectively. The intensity of the Cu 3p peaks decreases considerably to zero as the Fe 3*p* intensityincreases from zero as more Fe is deposited.

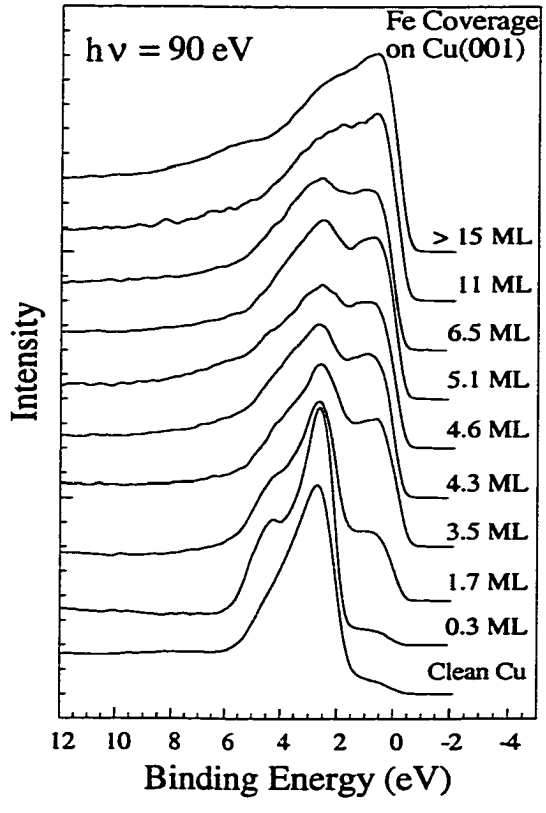

Figure 3.5: Angle-integrated photoelectron energy distribution curves of the Cu and Fe 3*d* valence bands at hν = 90 eV for clean Cu, and the Fe films shown.

At the 0.3 to 4 ML film thickness, a distinct shoulder is seen at about 4.5 eV binding energy that is less evident at higher coverages.

In order to extract more information from these data, one can produce difference spectra that are shown in figure 3.6 for 1.7 and 6.5 ML Fe coverages. These spectra are produced by estimating the attenuation of the Cu substrate by the overlying Fe film, correspondingly scaling the clean Cu spectrum, and subtracting it from the Fe-overlayer spectra. In addition, a smooth background of inelastically-scattered electrons has been removed from the difference curves. This effectively provides a spectrum showing the Fe-induced changes in the surface density of states. In figure 3.6(b) and 3.6(c) these difference curves are presented as well as spectra (dashed curves) which would arise from ±20% errors in our coverage estimates.

The 6.5 ML difference curve shows a spectrum that is essentially identical to the spectrum for thick Fe films, consistent with a bcc-like DOS. In contrast, the 1.7 ML film shows a characteristic three-peaked structure unlike bcc Fe. The details of this structure, however, depend not only on the charge that is provided by the Fe overlayer but also depends on any transfer of charge between the substrate and the overlying film. The one new feature, clearly evident in the curves in figure 3.5, however, is the feature that appears at ~4.5 eV binding energy.

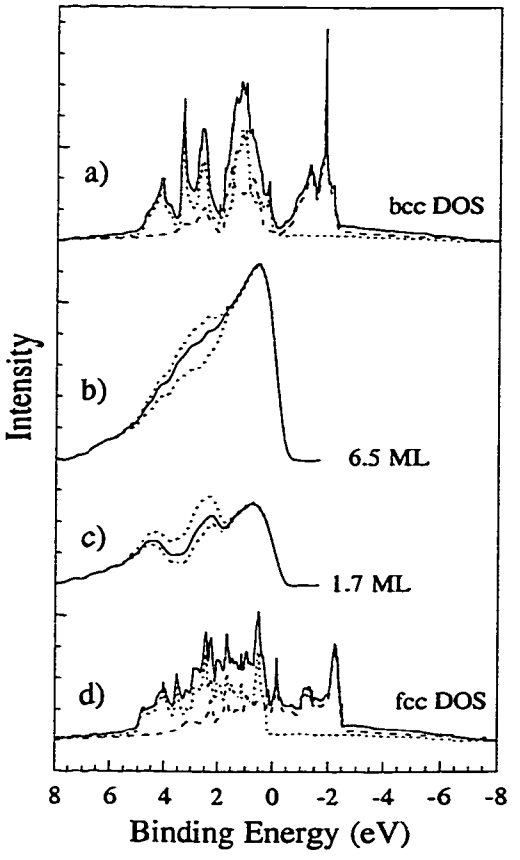

Figure 3.6: (a) Density of States (DOS) for bulk bcc Fe. Short-dashed line gives the spin-up DOS, and the long-dashed line gives spin-down DOS. (b and c) Difference spectra obtained for 6.5 and 1.7 ML Fe on Cu(100) respectively. Dashed curves represent variations in Cu attenuation corresponding to a variation in thickness of ±20%. (d) DOS for bulk fcc Fe.

From simple concepts of two dimensional films, one might anticipate the lack of an extended, periodic near-neighbor environment to produce a dehybridization of electronic states. This, however, would lead to a band narrowing, which is not in accord with the 1.7 ML spectra in figure 3.5.

To understand better the difference between these electronic structures, we have calculated (in collaboration with Chris Harwell and Randall Hall from the LSU Chemistry department) the bulk band structures for both fcc and bcc Fe, and the DOS for these structures appear in figure 3.6(a) and (d).[48]

These calculations have been accomplished with the WIEN97 code, which uses the generalized gradient approximation with a fully relativistic linearized augmented plane-wave method for ferromagnetic films.[49] The lattice constants used in the fcc structure correspond to that of bulk Cu while the bcc parameters are those of bulk Fe. Although the DOS within the bands vary, neither the bandwidth nor the location of the bottom of the *d*-band is significantly different for FM fcc Fe compared with FM bcc Fe. Structurally alone, we cannot yet explain the 4.5 eV binding energy feature.

3.3 Fermi Surface Contours (Spin-Reorientation)

Additional information on the electronic changes that are occurring can be extracted from measurements of Fermi surface contours as a function of film

thickness. The instrument used to collect these contours is the display-type Ellipsoidal Mirror Analyzer (EMA) discussed in chapter 2.

The EMA collects electrons in a 32° half-angle about the sample normal, performing energy analysis, while preserving the angular information of the electrons, providing an energy-resolved two-dimensional image of the intensity pattern of electrons emitted from the sample. These contours, obtained with the EMA, can be visualized using the cartoon at the top of figure 3.7. There, a bulk fcc Brillouin zone is shown with a spherical cross-section intersecting it. We essentially image a top-down view of this cross-section with emission angle mapping directly to k-vector.

Figure 3.7 also shows photoelectron angular distribution images of the Fermi surface of a 4.2 ML Fe film compared with that from an 8.7 ML Fe film, both taken with hν=75 eV. The photons are linearly polarized in the horizontal plane i.e., the [110] azimuth of the crystal. The data have only been corrected for channel plate efficiency and are plotted on a linear intensity scale, with the whitest feature representing maximum photoemission intensity and the darkest feature representing minimum intensity. Ideally the image should show sharp contours of intensity. Broadening of the structure in the images can be due to both energy (lifetime) and wave-vector effects as well as imperfections in the structure of the overlayer film.

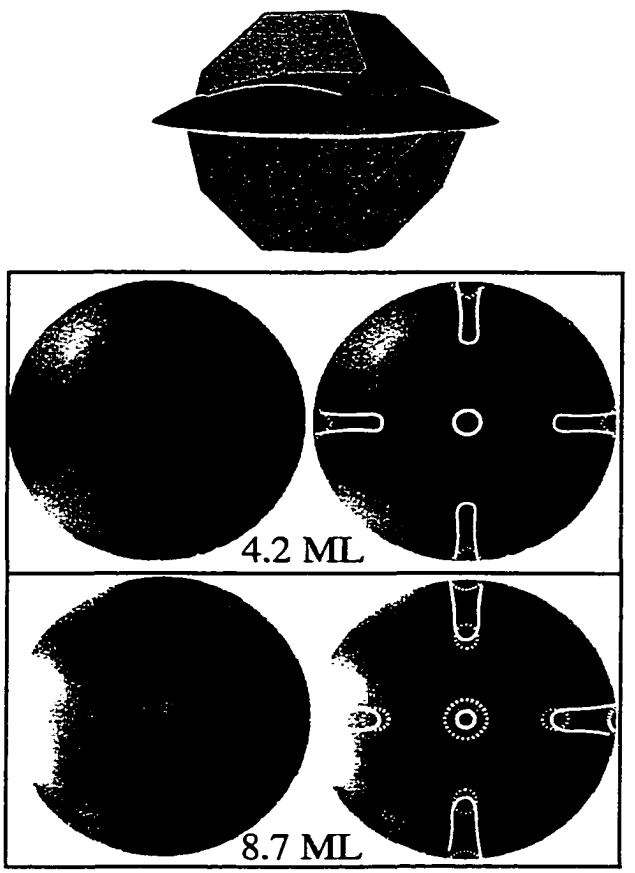

Figure 3.7 Top: Schematic of the principle by which photoemission measures Fermi surface contours. An fcc Brillouin zone is shown with a free-electron final state intersecting it. By changing the photon energy, the k-space radius of the final state will move throughout the Brillouin zone. Middle, bottom: Photoelectron angular distribution images of the Fermi surface of a 4.2 ML and an 8.7 ML Fe film on Cu(100) taken with hν=75 eV. The horizontal azimuth is the [110]. Calculated FS contours are overlaid in white on the right; majority bands solid and minority bands dashed.

In the right of figure 3.7 these images are overlaid with the FS contours predicted by theory for the fcc (middle) and bcc (bottom) Fe.

The 4.2 ML image from the fcc Fe film shows distinct features in the [100] directions as well as normal-emission intensity. As the film thickness increases, these local intensity maxima appear to *rotate by 45°*. The 8.7 ML image shows distinct intensity in the [110] azimuths. The FS images for thicker films (> 8.7 ML) are similar to the 8.7 ML image. It is just at these ranges where the magnetization reorients from perpendicular to in-plane. The rotation of intensity maxima is probably also associated with a structural transition but the theoretical contours show that more than just the fcc-bcc transition is involved. However we have not yet computed an antiferromagnetic fcc structure, such as that proposed by Asada and Blügel.[46]

The observation of bulk-like Fermi surface contours in atomically thin films has been observed previously for Ni on Cu(001), supporting our comparison with FS contours from bulk calculations.[50] Although the experimental contours are rather diffuse for Fe on Cu(001), these data suggest that an electronic structural transition that strongly affects the Fermi surface is associated with the magnetization reorientation observed previously.[38, 39, 41, 44]

Chapter 4

Oxidation of Fe Films on Cu(100)

This chapter will focus on the high-temperature oxidation of ultrathin Fe films deposited on Cu(100) as described in chapter 2. Core-level as well as valence-band photoemission will be used to discuss the electronic changes associated with the oxidation of these ultrathin Fe/Cu(100) films. In addition, supporting low energy electron diffraction (LEED) data will be presented to compare the structural changes observed before and after oxidation.

Furthermore, data from an electron yield technique called near edge X-ray absorption fine-structure (NEXAFS), will be discussed. This absorption technique probes the deeper lying core levels of the oxide, to reveal the effect of oxidation on the ultrathin Fe/Cu(100) layers.

During our investigation of oxide films that are relevant in magnetic devices, we discovered that well-ordered oxides may be grown on dissimilar metallic substrates. This allows us an alternative method for studying oxides, ameliorating

the need for difficult surface preparation techniques required with single crystal oxides. In our case, cleanliness and stoichiometry are controlled by our growth methodology. Cleanliness is well under our control, however the stoichiometry of our oxides relies on the details of the kinetics leading to the final product. Although thermodynamics may suggest a *most* stable oxide, kinetics may preclude its formation. One goal of this study is to investigate the regimes of Fe thickness, annealing temperature, and oxygen partial pressure that result in the desired phase formation on Cu(100).

One important point to note is that these films were formed and characterized in three different chambers using three different electron spectrometers to obtain the photoelectron energy distribution curves (EDC's).

The initial core level data was obtained in a UHV chamber equipped with a Mg K_α source that produced 1253.6 eV X-rays. This chamber was also equipped with a Helium I resonance lamp that produced 21.2 eV photons. Electron spectra were obtained using a VSW HA50 hemispherical analyzer. The detector position was aligned at 22.5° with respect to the sample normal and the detection was *highly angle-resolved* within ±3° acceptance angle.

The majority of our data was taken with a second instrument at the plane grating monochromator (PGM) beamline at CAMD. The photoelectron spectrometer used to collect this data is a display-type ellipsoidal mirror analyzer (EMA) described in Chapter 2.2.[29] As mentioned previously, it collects electrons in a ±32° half-angle about the sample normal, providing differential energy analysis while preserving the angular information of the electrons. The EMA is also able to obtain *angle-integrated* energy distribution curves (EDCs), which is a measure of the electronic DOS.

Attached to both of the chambers described above was a smaller preparation chamber where the entire sample preparation (Ar-sputtering, annealing and oxidation) was performed. Samples were then transferred to the main chamber for characterization.

A third UHV chamber was used containing a 25-mm hemispherical analyzer for *angle-resolved* UPS, and an electron channeltron used for NEXAFS studies on our films. This chamber was equipped with retractable rearview LEED optics and all the sample preparation as well as the sample characterization was done in the same chamber. The sample characterization equipment was located on the top section of this chamber, while the sample preparation equipment (sputtering, annealing and oxidation) was located separately at the upper section.

4.1 Iron Oxide Formation – Previous Work In Our Group

The STM (Scanning Tunneling Microscopy) images, shown in figure 4.1, were collected by Karunamuni as part of his thesis work and it is used with his permission.[19] The Auto Probe VP 900 model STM used above, was manufactured by Park Scientific Instruments, and it is housed in a UHV chamber located in the Surface Science laboratory at LSU.[19]

The STM image of 0.5 ML Fe evaporated on a Cu(100) substrate is shown in figure 4.1 a). As can be seen in the figure, Fe deposition onto the clean Cu(100) surface results in islands randomly spaced across the surface, with the growth nucleating randomly. At higher Fe coverages these islands begin to coalesce to give good layer-by-layer growth at room temperature. Figure 4.1 b) shows the surface of 0.5 ML Fe/Cu(100) after it was exposed to ~1000L oxygen at room temperature. The islands become ill defined as we lose imaging capability.

Previous photoemission studies on the room temperature oxidation of Fe/Cu(100) identifies this oxide as Fe_2O_3.[51] The STM images shown in figures 4.1 c) and 4.1 d) are for Fe/Cu(100) surfaces oxidized at 810 K, and it shows dramatically different surfaces compared to figure 4.1 b).

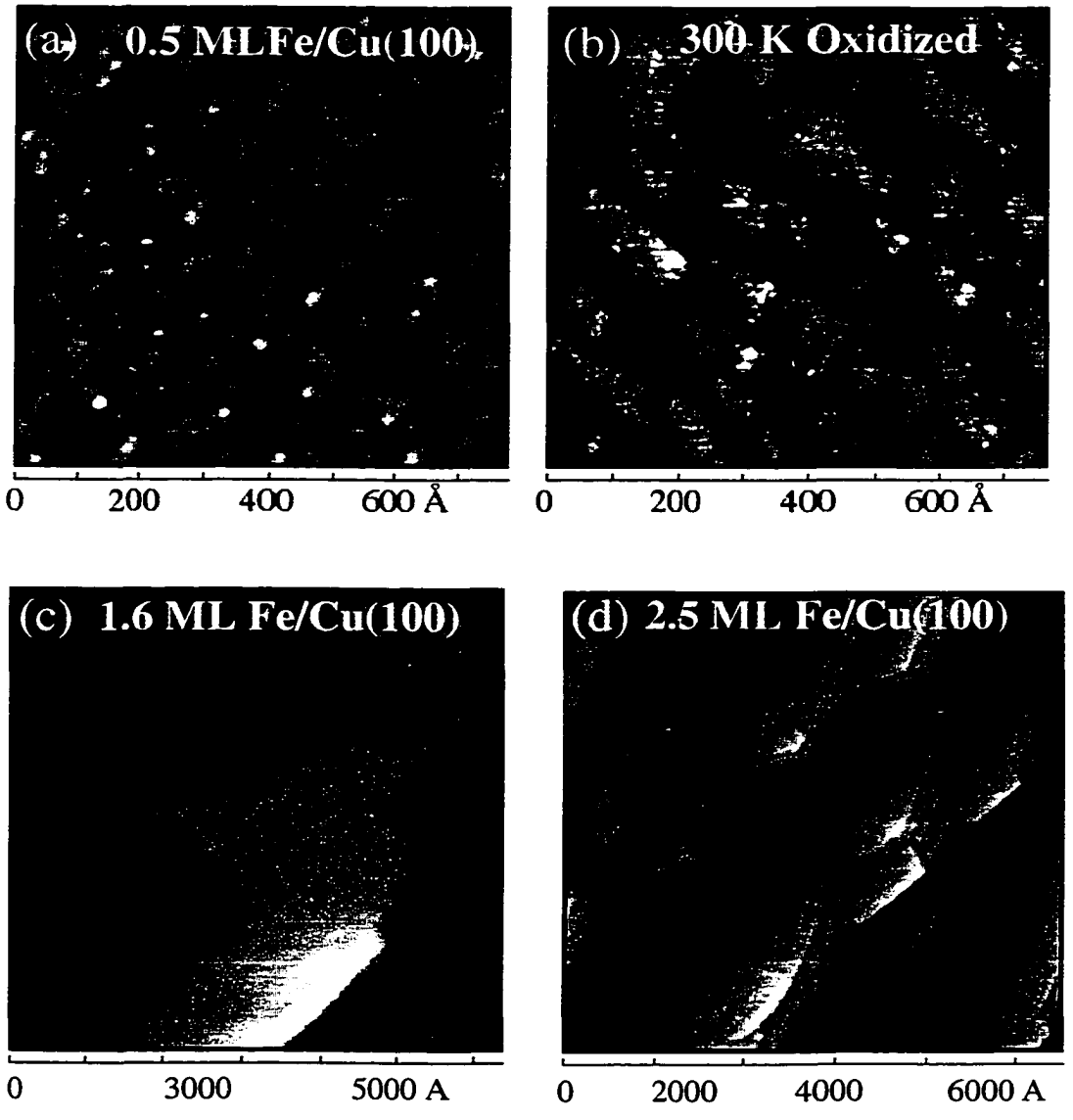

Figure 4.1: STM images of Fe/Cu(100) and Fe/Cu(100) oxidized under different conditions. (a) 0.5 ML Fe/Cu(100) showing uniform growth of Fe islands on Cu. (b) Room temperature oxidized Fe/Cu(100) is non-crystalline. (c) 810 K oxidation of 1.6 ML Fe/Cu(100) showing FeO formation with two directions of oxide strips. (d) 810 K oxidation of 2.5 ML Fe/Cu(100) showing Fe_3O_4 formation with a completely different structure than FeO.[35]

The oxide formed for initial Fe coverages below 2 ML, shows the formation of micron long islands along two preferential directions ([011] and [1$\bar{1}$0]) which are perpendicular to each other as shown in figure 4.1 c). These micron-long oxide strips force Cu to flatten locally by moving substrate steps aside. The dark stripes within these oxide strips are slight modulations in z-height. These dark stripes are believed to result from strain relief from differences in lattice spacing between the oxide and the substrate. Upon closer examination, the atoms are arranged in a fashion that creates a hexagonal superstructure. Experimental STM results and LEED data compared with simulated LEED patterns provide structural evidence that the oxide formed from < 2 ML initial Fe coverage is FeO. Figure 4.1 d) shows the STM image after 810K oxidation of > 2 ML Fe/Cu(100). The oxide that forms at high Fe coverage is different from the FeO that formed at low initial Fe coverage. Unlike the FeO islands, which are generally isolated, this new oxide grows in large patches on the Cu surface. The edges of the oxide islands are straighter than the FeO edges. Moreover, the edges are oriented 15^{o} from the [001] directions. The dark stripes as well as the hexagonal superstructure still exist on this new oxide. The new oxide was identified structurally on the basis of STM, LEED and simulated LEED as Fe_3O_4(111) on Cu(100). Patches of FeO can be seen on the Fe_3O_4(111).

This prior STM study provides the background for the work in this thesis. The different oxides were identified structurally, but no spectroscopic evidence was given to verify that FeO and Fe_3O_4 were indeed formed. The rest of the work described here will establish a link between this structural STM study, and the electronic nature of the system.

4.2 LEED – This Investigation

As a transfer standard for comparison with prior work we use LEED to determine which oxide forms under the different conditions described above. All the LEED data described below were taken in the UHV chamber at CAMD.

Figure 4.2 a) shows the 56 eV LEED pattern of a 0.74 ML Fe/Cu(100) surface that was oxidized in 1 x 10^{-6} Torr oxygen at 540 ^{o}C for 5 minutes as described earlier. Prior STM measurements showed that this initial coverage results in two domains of FeO, with long strips of oxide aligned along [110] directions. The LEED spots in 4.3 a) are arranged in two hexagons rotated 90 degrees with respect to each other consistent with the STM observation of 2 mutually perpendicular domains. The lattice constant measured from the center of each of the bright spots in the hexagonal LEED pattern is consistent with the value for FeO.

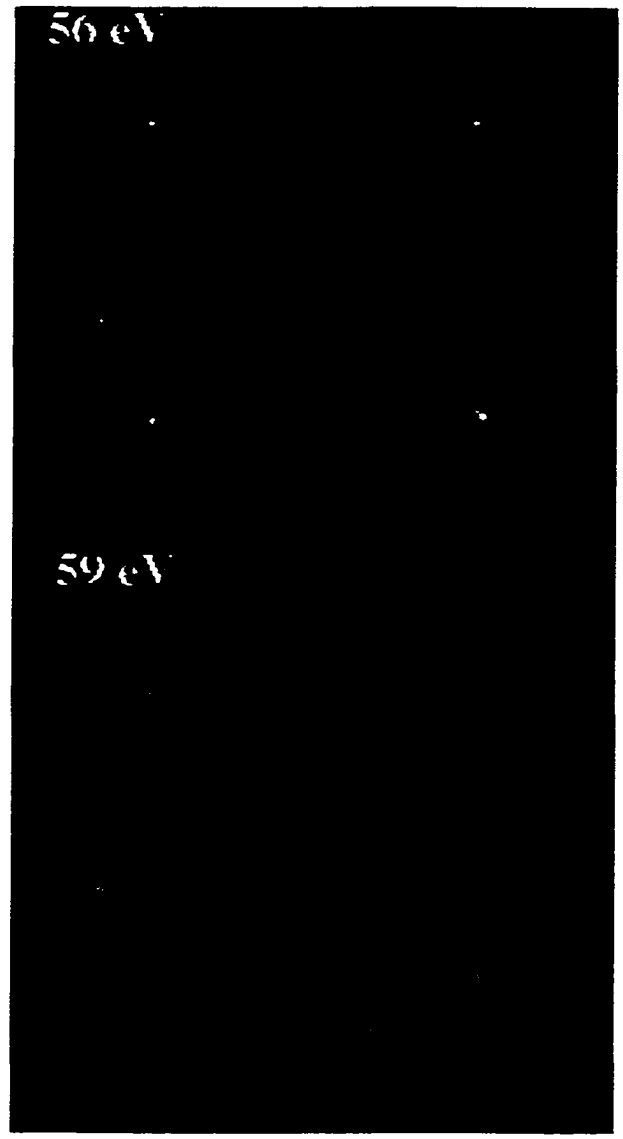

Figure 4.2: (a) LEED pattern of oxidized 0.74 ML Fe/Cu(100) taken at 56 eV. The LEED patterns are arranged in two hexagons rotated by 90 degrees. Diffraction spots indicate the presence of a superlattice on the oxide surface. (b) The LEED pattern (59 eV) after oxidation of 2.5 ML initial Fe/Cu(100) shows a similar pattern, but the diffraction spots are now smeared out.

Furthermore, the oxide pattern is split into several diffracted spots that are aligned with the (100) direction on the Cu substrate that is also visible. These split spots suggest that a superlattice is present on the oxide surface. This compares well with STM results by Karunamuni that found just such a superlattice with a periodicity of 20.5Å

The LEED pattern of a 2.5 ML Fe/Cu(100) oxidized film is shown in figure 4.2 b). The LEED pattern looks identical to the FeO films with the exception that the diffraction superstructure spots are smeared into streaks. Previous reports on Fe-oxide films formed at room temperature showed similar patterns but without the distinct spot-splitting that we saw from oxide layers formed for an initial thickness below 2 ML.[16, 52]

4.3 Core-Level Photoemission

4.3.1 X-Ray Photoelectron Spectroscopy (XPS)

As described in the previous chapter we can make use of XPS to probe the core-levels of our substrate and overlayer since it is element specific. Furthermore XPS can also provide information about chemical bonding by comparing core level shifts that arise from charge transfer during bond formation. The initial core level data was obtained in the UHV chamber in the surface science laboratory at LSU.

The XPS spectra in figure 4.3 were taken after the Fe/Cu(100) films, shown in figure 3.3, were oxidized. The 1.8 ML Fe/Cu(100) spectrum in figure 4.3 again shows the presence of Cu 2*p* peaks as well as Cu Auger peaks. The presence of oxygen is indicated by the intense 513 eV O Auger peak located at an apparent binding energy of ~ 740.8 eV. The peak is broad and intense and for this photon energy, overlapping the Fe 3*p* core level peaks. Upon oxidation, the Fe $2p_{3/2}$ peak experiences a core level shift of ~ 4.2 eV to higher binding energy and it is located at 710.9 eV compared to 706.7 eV of the unoxidized Fe/Cu(100) spectra shown in figure 3.3.

All the Fe Auger peaks are still present from the oxidized Fe/Cu(100) film, but it they are not as sharp as the Auger peaks from the unoxidized Fe/Cu(100) films. The O 1*s* peak is observed at 528.7 eV. The intensity is very low and it is located between the high intensity Fe and Cu LMM Auger peaks. Again, at binding energies below 300 eV, some of the shallow core-levels like the Cu and Fe 3*p*'s at 75.2 and 52.5 eV are visible, but their intensities are extremely low since they have a low cross-section at this photon energy. The spectra at higher initial Fe coverages essentially show the same peaks with the main difference being increased intensity of the Fe and O peaks.

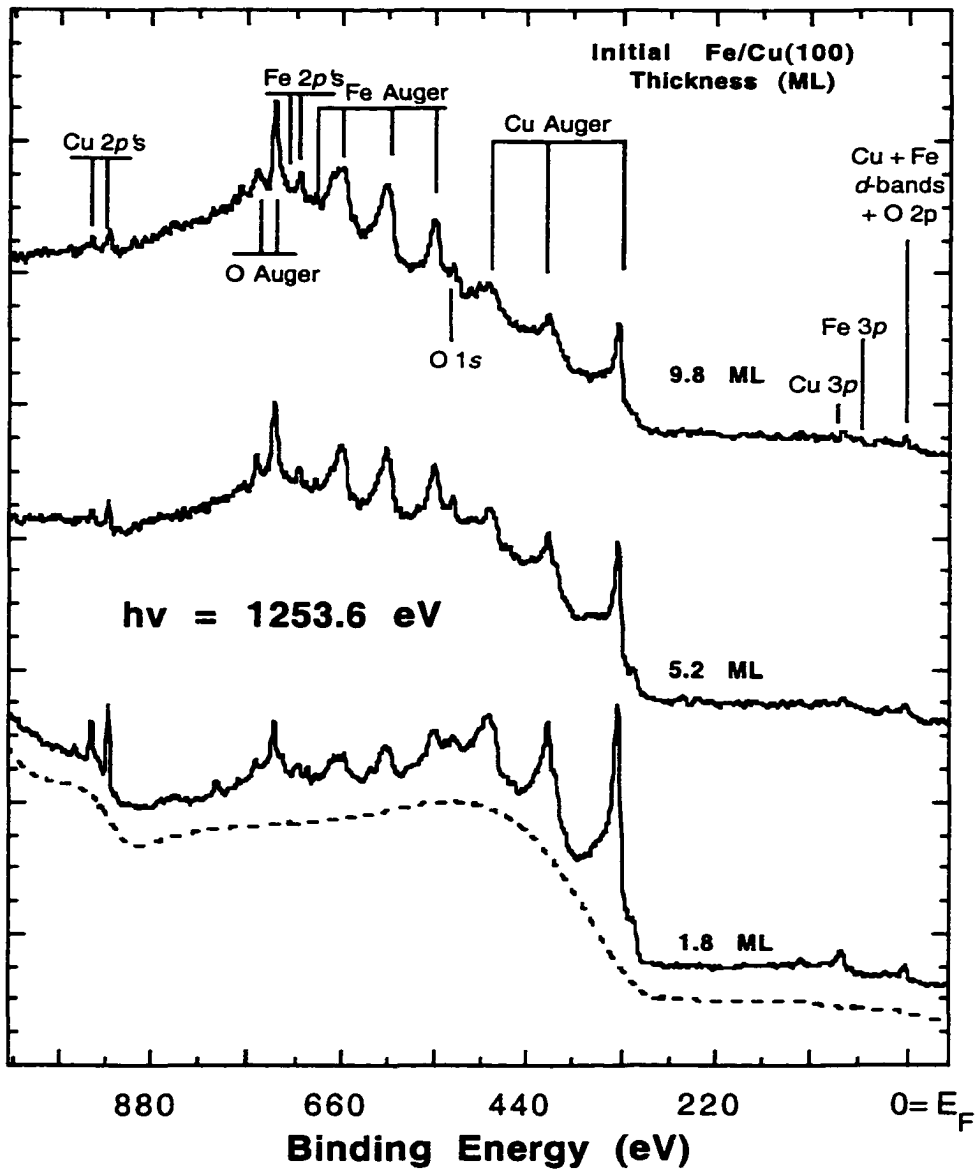

Figure 4.3:(a) XPS spectra of Fe/Cu(100) films of different thicknesses oxidized at 810 K. The Fe 2p underwent a core level shift after oxidation. (compare with Figure 3.3)

This indicates the presence of more oxide, in the form of either larger oxide islands or thicker oxide films.

The Fe $2p_{3/2}$ peak undergoes a smaller core level shift than the $3p$'s and it is located at 710.1 eV compared to 706.7 eV (~ 3.4 eV shift) from the clean Fe/Cu(100) shown in figure 3.3. Previous studies showed that the observed chemical shifts for Fe^{2+} is ~ 3.0 eV and for Fe^{3+} ~ 4.1 eV.[20] Kishi *et al.* [52, 53] as well as others[12] reported chemical shifts of the Fe $2p_{3/2}$ peak of ~ 2.9 eV on FeO and ~ 3.8 eV for Fe_3O_4. Chambers *et al* [54] reported XPS and XPD (X-ray photon diffraction) measurements on several Fe oxide single crystals, including Fe_3O_4 and reported the appearance of a distinct shoulder on the Fe $2p_{3/2}$ peak located at ~709.0 eV for Fe^{2+} and ~710.5 eV for the Fe^{3+} species. We did not observe this shoulder in our data due to the overlapping of the Fe $3p$ core level peaks with the O and Fe Auger described above.

Perhaps the most striking aspect of the data shown in figure 4.3 is related to the oxide film resulting from oxidation of 9.8 ML Fe/Cu(100). Clearly oxide forms on the surface as shown by the presence of Fe and O core level peaks. If all 9.8 ML

Fe formed an oxide layer, the thickness of the oxide would be ~13ML. This amount of oxide would be expected to attenuate completely any signal from the Cu substrate. This is inconsistent with the reasonably strong Cu Auger and Cu 2*p* peaks observed here. Their presence suggests that either the overlayer oxide film is very thin, that the oxide is columnar with bare Cu between islands, or that Cu is located on top of the oxide film.

STM suggests that the initial oxidation of Fe/Cu(100) produces flat islands of oxide and that further oxide growth produces thicker films, inconsistent with columnar growth. Furthermore, we have tested for the presence of Cu atop the oxide by angle-dependent XPS measurements. The angle of emission of the detected electrons and the surface normal was varied from 85° (grazing emission) to 5° (near normal emission). If Cu covered the oxide surface, then we would expect to see an enhancement of the Cu signal at grazing angle, while the Fe signal from the oxide would be less intense. We did not see any changes in the relative intensities of the peaks. Furthermore ARUPS showed strong dispersion of the Cu signal. This was indicative that the Cu did not cover the oxide and that the signal came from the substrate. These measurements show conclusively that Cu is not coating the oxide

surface. If indeed the resulting oxide is very thin then the question stands, **where did the missing Fe go?**

XPS measurements taken on our sample after repeated cycles of Fe deposition and subsequent oxidation at 540 ^{o}C revealed the migration of Fe atoms into the near surface region of the Cu(100) substrate despite the bulk immiscibility of Fe in Cu. In fact, previous studies showed that deposition at substrate temperatures as little as 20^{o}C above room temperature, can cause intermixing in the surface layer with incorporated Fe islands that appear as pits in the Cu terrace.[55] These "pits" have been observed in Karunamuni's previous STM work.[36] We believe this is the fate of the "missing" Fe.

4.3.2 Changes in the 3*p* Peaks

The XPS core-level data described above showed multiple overlapping Fe 2*p* features making the identification of valence states ambiguous. In order to address this, we decided to investigate chemical shifts in the Fe 3*p* shallow core levels using synchrotron radiation from the PGM beamline at CAMD. These angle-integrated experiments were done using the Ellipsoidal Mirror Analyzer (EMA). The sample preparation and Fe evaporation were carried out in the same film-growth chamber

used above. The sample was then transferred with a magnetically-coupled transfer arm to the main chamber for analysis.

In order to probe the Fe 3*p* core levels situated at 53.1 eV binding energy for clean Fe/Cu(100) and ~ 55 - 56 eV for oxidized Fe/Cu(100), we used photons of energies that ranged between 120 and 200 eV. The thickness was established using the methods described in the previous chapter (i.e. by comparing the attenuation of the Cu 3*p* peak and growth of the Fe 3*p*).

Figure 4.4 shows four angle-integrated EDC's taken at a photon energy of 165 eV with the EMA. All EDC's are aligned with respect to the Fermi edge as indicated on the bottom of the figure. The solid curves in the figure (a) and (c) were obtained from a 1.6 ML and 6.1 ML Fe/Cu(100) films respectively, prior to oxidation. The Cu $3p_{1/2}$ and $3p_{3/2}$ are barely resolved at 75.1 eV and 77.3 eV. The intensity differences of the Fe 3*p* peaks for the 1.6 ML and 6.1 ML Fe/Cu(100) at 53.1 eV binding energy can also be noted. The thicker film also shows a more intense Fe 3d peak near E_F relative to the substrate Cu's 3*d* peak at ~2 eV. After oxidation, the data given by the solid curves are obtained. The Cu $3p_{1/2}$ and $3p_{3/2}$ are even more intense than they were from the unoxidized film, indicating the presence of bare Cu patches on the surface.

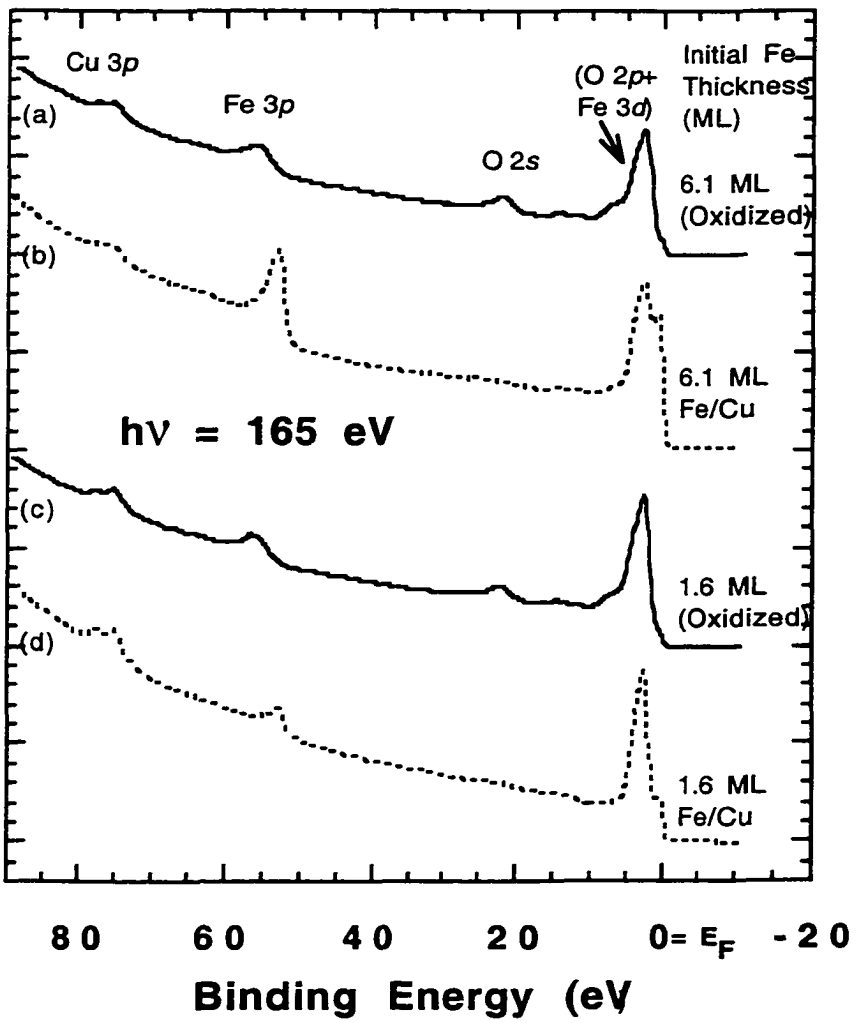

Figure 4.4 Angle-integrated EDC's taken at a photon energy of 165 eV with the EMA. The dashed curves in the figure (b) and (d) were obtained from a 1.6 ML and 6.1 ML Fe/Cu(100) films respectively. The solid curves (a) and (c) represent the 1.6 ML and 6.1 ML Fe/Cu(100) films that were oxidized.

The spectrum from the 1.6 ML Fe/Cu(100) film undergoes several changes upon oxidation. First we notice that the Fe 3*p* peak shifts by ~ 3.0 eV to 56.0 eV binding energy, secondly an O 2*s* peak appears at 22.4 eV, and third a shoulder grows just below Cu *d*-bands at ~7.0 eV. This shoulder is due to the O 2*p* states that are hybridized with the Fe 3*d*-bands.[7] The DOS at the Fermi edge also drops significantly as compared to the metallic Fe due to the charge transfer of Fe 3*d* to O 2*p* during bond formation. The spectrum for the oxidized 6.1 ML Fe/Cu(100) film undergoes almost identical changes, but the Fe 3*p* peak broadens and shifts to even higher binding energy. The difference of about 0.7 eV in the Fe 3*p* core level shift observed for the thick and thin Fe oxide, compares well with the Fe 2*p* core level shift of ~1eV seen in the XPS data. As mentioned above, this additional shift is indicative of the presence of both Fe^{2+} *and* Fe^{3+} cations on our substrate.

In figure 4.5 a closer look at the Fe 3*p* states is presented. The lower curve shows the spectrum from 2 ML clean Fe on Cu. This curve can be fit by a single Gaussian curve located at 53.1 eV with a full-width half maximum of 2.35 eV. This 3*p* peak is really composed of two unresolved features – the $3p_{1/2}$ and $3p_{3/2}$ but their small splitting and individual linewidths (short lifetimes) give a single feature.

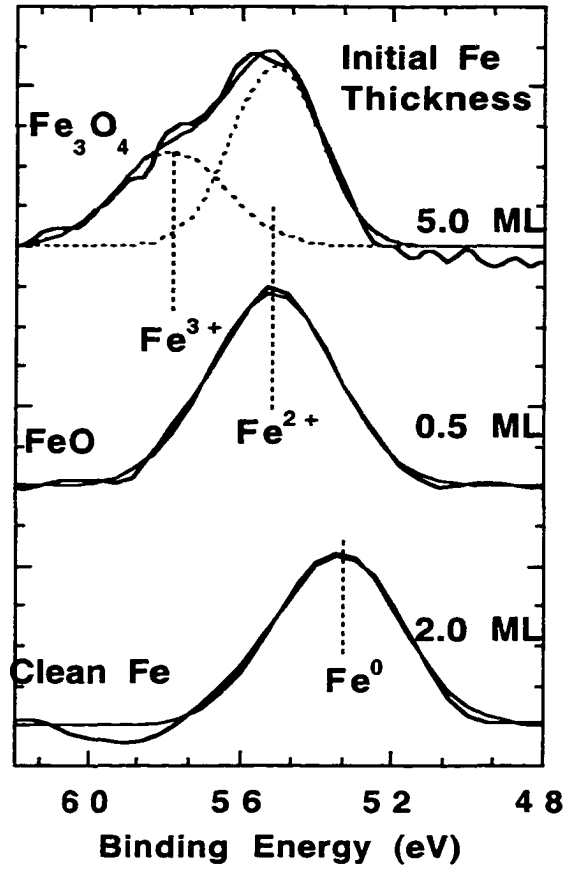

Figure 4.5: Fe 3*p* taken at hν = 145 eV. (a) 2.0 ML Fe/Cu(100) fitted with a single gaussian peak at 53.1 eV. (b) The 0.5 ML oxide fitted with a single Gaussian peak, located at about 55.6 eV consistent with (Fe^{2+}) in FeO. (c) The Fe 3p for 5.0 ML oxide with a two gaussian peak fit located at 55.1 eV and 57.6 eV, indicating the presence of Fe^{2+} and Fe^{3+} cations, hence Fe_3O_4 formation.

When a 0.5 ML Fe film is oxidized, this peak shifts by 2 eV to higher binding energy and narrows to 2.30 eV as shown in the middle curve. This shift and narrowing indicates that only one ionic species of Fe is present on the sample, and its location is comparable to Fe^{2+} positions reported in literature.[56]

On the basis of a structural model, the earlier STM study conducted in our lab suggested that oxidation of < 2 ML Fe resulted in the formation of FeO. These data spectroscopically confirm that identification. Furthermore, when thicker Fe films are oxidized, the 3*p* peak is substantially different. In that case, an additional Gaussian located at 57.6 eV is needed for an adequate fit. This second Gaussian implies that a second Fe valence is present in the oxide film. We identify this second peak as being due to Fe^{3+}. The oxide formed from thicker Fe films contains both Fe^{2+} and Fe^{3+} cations, as does Fe_3O_4. However the ratio of Fe^{2+} to Fe^{3+} in our film is 2:1 whereas in magnetite (Fe_3O_4) the ratio is 1:2. This means our oxide has excess Fe^{2+}. Either we have incomplete oxidation or we have reduced regions in a very thin film. A reduced region, such as a Fe terminated interface, in combination with the atomically-thin films that we grow, are consistent with these observations.

4.4 Valence Band Photoemission

4.4.1 Initial Investigation–He I Lamp (Angle-Resolved)

Valence band photoemission studies were performed in the Surface Science laboratory at LSU, using a He I (21.22 eV) UV source and a VSW HCA50 hemispherical analyzer. The detector position was aligned at 22.5° with respect to the sample normal.

In figure 4.6(a) the valence band spectra for iron deposited on Cu(100) are shown as a function of increasing Fe thickness. For the 0 ML Fe on Cu(100) sample (bottom curve) emission from the copper 3*d* bands gives the peaks located at about 2.3, 3.3 and 4 eV binding energy. These peaks correspond to emission from Cu 3*d* bands of Δ_5, Δ_2 and Δ_3 symmetry respectively. Weak emission from the Cu *s-p* band is observed at the Fermi edge. The fairly broad peak at located at ~1.2 eV binding energy is due to a Cu surface state. Its presence confirms that our Cu(100) is clean and well-ordered.

As Fe is deposited, we note the growth of Fe 3*d* features located near the Fermi edge, superimposed on the Cu *s-p* band. In the 1.5 ML Fe/Cu(100) spectrum we note that the Cu(100) features are still strong and the surface state is still visible.

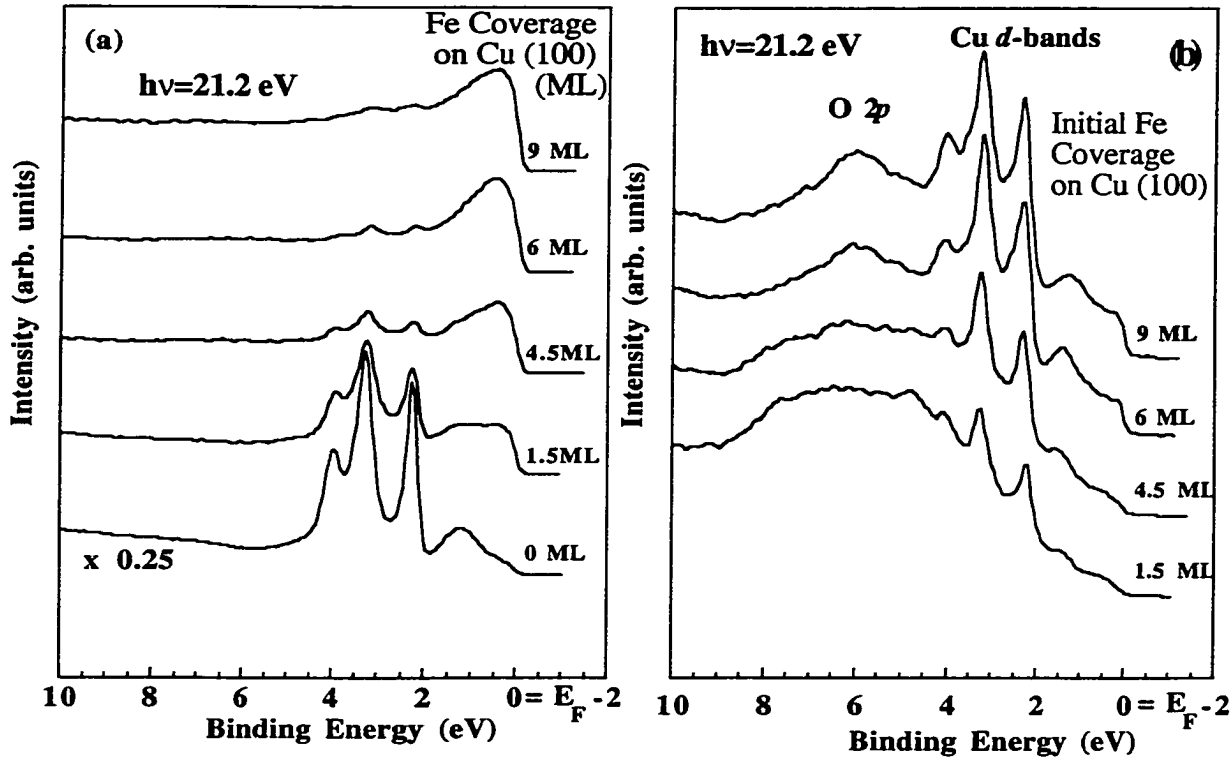

Figure 4.6: (a) UPS valence band EDC's, as a function of increasing Fe thickness on Cu(100). For thicker films, the Cu features decrease significantly as the Fe 3*d* becomes more dominant. (b) EDC's of the same film after the 810K oxidation. A surprising observation is that with increasing initial Fe coverage there is an enhancement of the Cu 3*d* features,as well as a sharpening of the O 2*p* peak ~6 eV.

This indicate that we still have some bare Cu, i.e. some second-layer growth is occurring before the first layer is complete. For thicker films the Cu features decrease significantly while the Fe 3*d* features grow to dominate the spectra.

In figure 4.6(b), we show EDC's of the same films after the 810K oxidation. For the low initial Fe coverage (1.5 ML), we observe a broad oxygen 2*p* valence band between 3 and 9 eV. Cu 3*d* features are also observed from patches of bare Cu. A low DOS is noted at the Fermi edge. With increasing initial Fe coverage, we note that the O 2*p* feature becomes more peaked at 6 eV and we see an enhancement of the Cu 3*d* features. These observations imply that regions of Cu substrate are clean and free of oxide, as was previously observed with STM. The DOS observed at the Fermi surface is significantly higher than that expected from either Cu or from any of the common oxides of Fe.

Analysis of both angle-integrated and angle-resolved UPS spectra taken at different photon energies gave no evidence of Cu on top of the oxide films.

For oxidized Fe films much thicker than those in figure 4.6(b), we have observed spectra that are essentially identical to those from the 6 and 9 ML Fe films, *including Cu 3d-features of similar intensity.* This means that even in the presence of excess Fe, the oxide that forms during a single annealing cycle does not completely cover the surface: bare Cu remains and this is consistent with STM

observations. Furthermore, we only observe two distinctly different spectra for the high-temperature oxidized Fe. The spectrum from the oxide that forms for the thinner Fe films is characterized by a rounder oxygen 2*p* band and a low density of states at E_F. The oxide from thicker Fe films has an O 2*p* band that is sharply peaked at 6 eV and has a distinct metallic Fermi edge with a high DOS.

The enhanced DOS could arise from two sources. First, incomplete oxygen-coordination of Fe cations at the interface could result in a more metallic interfacial density of states. However, this would only be observed if the oxide overlayer were thin enough to allow penetration of the electrons from the interface. Second, incomplete oxidation may give rise to metallic Fe on the surface. However, we do not think that this metallic Fe is on the surface. Rather, we believe that the Fe is alloyed into the Cu. At first glance this may seem remarkable since Fe and Cu are not bulk miscible. However, alloy phase diagrams for surfaces may be very different from the bulk. Furthermore, evaluation of Karunamuni's STM data suggests that this alloying actually occurs. (Karunamuni observed "pits" that formed on the Cu terraces during the oxidation processes.)

Another remarkable observation is that in the presence of more Fe on the surface, the patches of bare Cu on the surface are larger after oxidation. At low

initial Fe coverage, the oxide covers more of the Cu substrate surface. As reported before, XPS (and STM) clearly showed the migration of Fe atoms into the underlying Cu substrate after repeated cycles of oxide formation. This implies that we have at least two competing processes on the surface: a) oxide formation and b) diffusion of Fe atoms into the Cu substrate. A model will be proposed in the next chapter to account for the behavior of this oxide layer on the Cu(100) substrate.

Since the UPS spectra from CuO(100) are very similar to what we have seen on oxidized Fe/Cu(100)[57], we have seriously studied the possibility of Cu oxidation in our experimental conditions.

Figure 4.7 shows the spectrum of clean Cu(100) using He I to test for the oxidation of the Cu(100) substrate. The Cu(100) sample was exposed to 1000 Langmuir of oxygen at room temperature and the only observed difference was a reduced intensity of peaks. Furthermore, we heated the Cu(100) substrate to 810K in 10^{-6} Torr O_2 for 5 minutes and no sign of oxidation of the substrate was observed in either the UPS or XPS spectra.

4.4.2 Angle-Integrated Photoemission Data

In figure 4.8, we show EDC's of oxidized Fe films on Cu(100) as a function of increasing initial Fe coverage taken at a photon energy of 45 eV with the EMA.

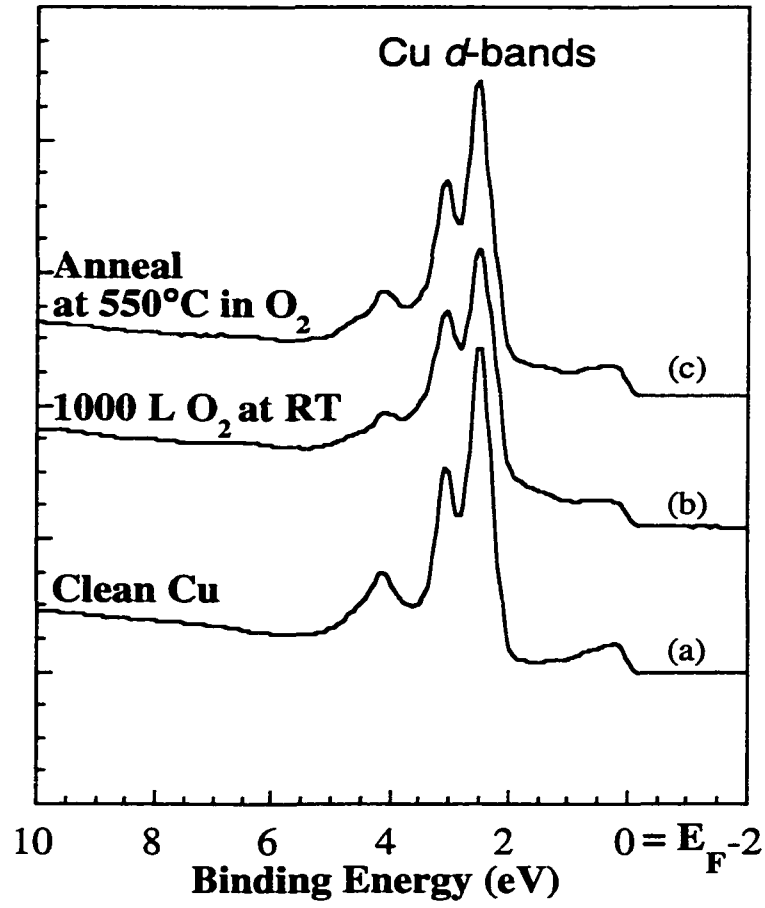

Figure 4.7: (a) UPS spectrum of clean Cu(100). (b) The same spectrum after exposure to 1000 Langmuir of oxygen at room temperature. (c) The spectrum obtained following the full high temperature oxidation procedure.

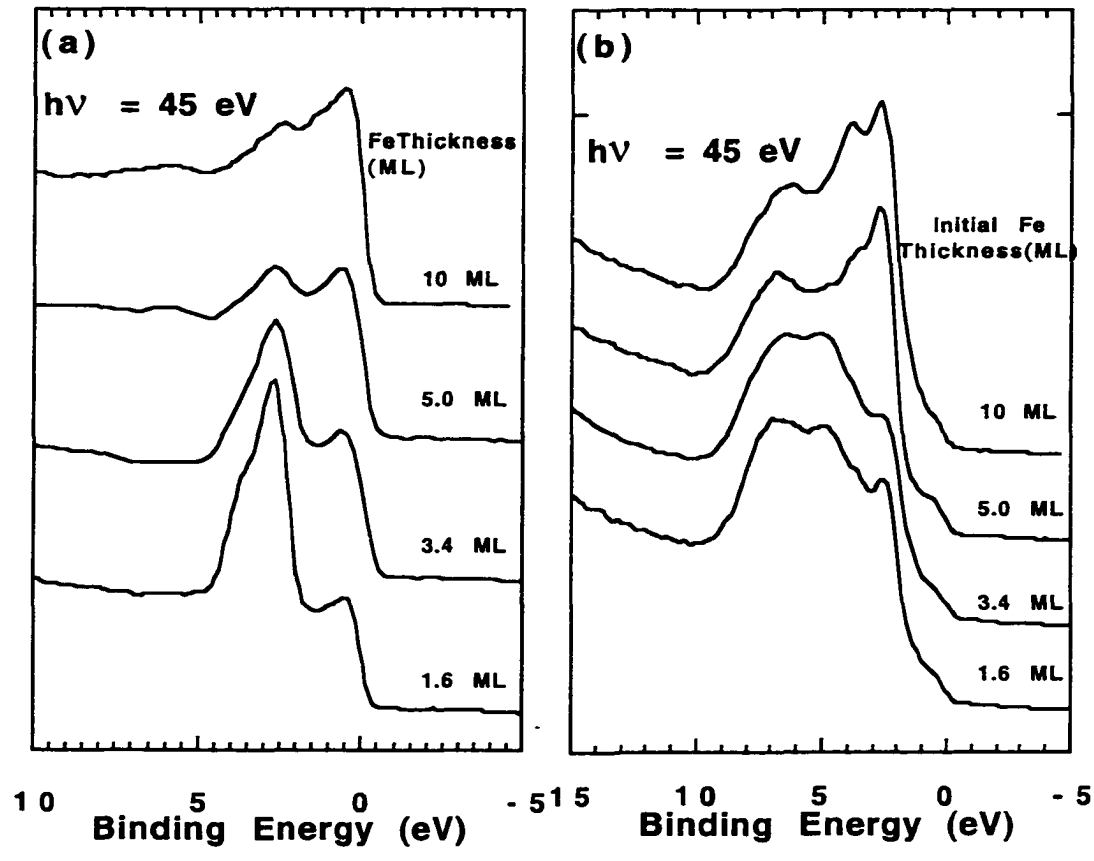

Figure 4.8 (a) Angle-integrated EDC's of Fe/Cu(100) films as a function of increasing initial Fe coverage taken at hν = 45 eV, and (b) the UPS data of the same films after oxidation.

For oxides from the low initial-Fe-coverage (1.6 ML and 3.4 ML), we once again observe a broad O *2p* and Fe *3d* hybridized band between 3 and 10 eV. The Cu *3d* features are also observed around 2.5 eV. Note that the Cu peaks are not well resolved. This is a consequence of the angle integration, which produces a spectrum that is an average over the Brillouin zone. At the Fermi edge, we observe a relatively low density of states with a broad peak that extends up to about 1 eV. With increasing initial Fe coverage (5.0 ML and 10 ML), we notice that the O *2p* peak becomes more peaked at ~ 6.8 eV and we see a strong enhancement of the Cu *3d* features at 2.5 eV and 4.8 eV that dominate the spectra. Again, for the thicker Fe films, it appears that there is less Fe oxide on the surface when in the unoxidized Fe film.

4.5 NEXAFS on Ultrathin Oxidized Fe/Cu(100) Films

This section will present a systematic study of Fe_3O_4 and FeO by means of X-ray absorption spectroscopy by comparing the changes observed in the oxygen K- and Fe $L_{2,3}$-edge absorption spectra.

These deeper lying core levels of the oxides were probed using near edge X-ray absorption fine-structure (NEXAFS). This is characterized by the absorption of a single photon resulting in a transition from a core level state to an excited state

coupled by a dipole transition. For the oxygen K edge (the 1*s* level or $l = 0$), the dipole selection rule means that only oxygen p character states ($l = 1$) can be reached in the final excited state. The observed spectra for O K-edge can hence be interpreted (to a first approximation) as the oxygen 2*p*-projected unoccupied density of states (DOS).[20, 58, 59]

This simplified approximation to the DOS can be problematic in trying to compare data with calculations due to the interaction of the excited electron in the final-state with its surroundings, where correlation effects lead to a modified apparent DOS. The O K-edge core hole is located at the oxygen site while the states in the unoccupied bands just above the Fermi level (E_F) exhibit their spectral weight mainly on the metal sites. The O 2*p* orbitals are hybridized with the metal 3*d* states and this leads to admixtures of 2*p* character in the unoccupied metal bands.

O K-edge spectra of iron oxides have been recorded previously with electron energy loss spectroscopy (EELS) and NEXAFS[58, 60, 61, 62]. Colliex *et al.* performed an EELS study of several Fe oxides on Si(100).[60] They observed interesting changes in the O K and Fe $L_{2,3}$ edges in FeO, Fe_3O_4, and Fe_2O_3. In the O K-edge pre-peak region (discussed in 4.4.1 below), a single peak is observed at ~530

eV and this peak's relative intensity gradually increases from FeO (Fe^{2+}) to Fe_3O_4 (that contain both Fe^{2+}+Fe^{3+}).

Stöhr *et al.*[63] showed that X-ray absorption could also be used to determine molecular orientations on surfaces because of the polarization dependence of the various molecular orbitals. Interpretation of experimental absorption data is often accompanied by calculations based on some theoretical models. For a qualitative interpretation of the features observed in the first electronvolts above threshold, molecular–orbital (MO) theory constitutes a useful tool. It calculates the energy and orbitals for a cluster made of a metal ion surrounded by its oxygen nearest neighbors. Wu *et al.* extended this work to solids and performed full multiple scattering (MS) calculations to interpret the characteristic features of the O K-edge absorption spectra.[59] They have connected the specific atomic arrangements and the electronic structure of each iron oxide with the position, shape, and intensity of the different characteristic features of the spectra and contrasted these calculated spectra with experimental data from single crystals.[59] A comparison of their calculated results with the data presented here is given below.

Schedel-Niedrig *et al.*[58] recently showed that by using XAS, it is possible to estimate the molecular orientations of Fe-O bonds. The various transitions are

polarization dependent, i.e. the electron emission intensity varies as a function of the **E** vector of the light, relative to the symmetry elements of the crystal structure.[12] They proposed a simple model where the O K-edge excitations are grouped into two types: antibonding *pd* π-resonances that are polarized perpendicular to the Fe-O bonds and antibonding *pd* σ-resonances, which are polarized along the Fe-O bonds.

NEXAFS measurements were carried out by measuring the total electron yield (TY) from the sample surface. The total electron yield is proportional to the absorption coefficient, provided the mean free path of the collected electrons is small compared to the photon absorption length. NEXAFS experiments were carried out at CAMD in the third UHV chamber described in chapter 2 using monochromatic photons from the PGM beamline.

The total electron yield I was measured by a channeltron placed in front of the sample. The primary photon beam intensity I_o was measured by a photodiode, which measures the total electron current from a tungsten grid, located in the front of the analysis chamber.

Spectral artifacts due to oxygen and iron contamination of the optical components in the PGM were removed by dividing the spectra from the oxidized films by the spectrum from clean Cu(100) under identical conditions.

4.5.1 Oxygen K-Edge

Figure 4.9 shows the O K-edge X-ray absorption spectra from an oxidized 3.7 ML Fe film grown on Cu(100). The angles between the **E** vector of the light and the surface normal of the sample were ~85 degrees for normal incidence and ~10 degrees for grazing incidence, respectively. This corresponds to mainly s-polarized light and p-polarized light, respectively, in our configuration. Guiot *et al.* showed for α-Fe_2O_3 films on α-Al_2O_3 that if the polarization of the photon beam is parallel to the (0001) plane (normal incidence), bonds lying mainly in the surface plane are probed. He also showed that at grazing angle bonds lying mainly out of plane are probed.

From the XPS data in figure 4.3, the oxygen 1*s* peak was located at ~530 eV binding energy and this is indicated with an arrow on the spectra in figure 4.9. All spectra were normalized at a photon energy of ~550 eV. The spectra can be divided into two distinct regions, which will be discussed separately.

(I) The first region (labeled A) directly at the threshold is usually called the near-edge or "pre-peak" region.[58] The structure of the spectra in this region can be used to differentiate between the three oxide phases (FeO, α-Fe_2O_3, Fe_3O_4), since it is due to transitions from O 1*s* to O 2*p* - Fe 3*d* hybridized bands.

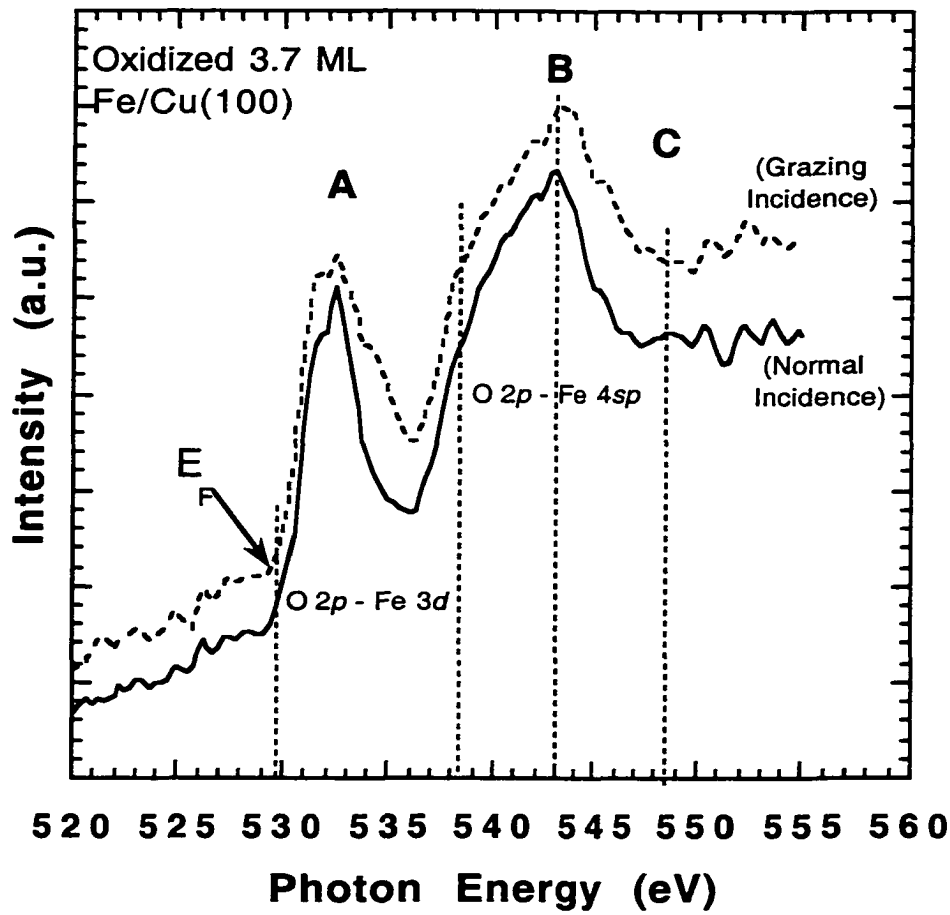

Figure 4.9: O K-edge X-ray absorption spectra of an oxidized 3.7 ML Fe film. The absorption spectra for normal incidence are given by the solid curve, and that for grazing incidence is given by the dashed curve.

This assignment agrees with observed structures. In our data we notice that peak A is broader for s-polarized light, suggesting the presence of multiple valence states of Fe. This compares very well with data on single crystals of Fe_3O_4 and with ultrathin Fe_3O_4 formed on other metallic substrates like Pt(111)[58, 62]. Wu also showed experimentally and with molecular orbital (MO) calculations that for Fe_3O_4 these peaks are not separated but can be represented as a single broad peak with a shoulder indicating the presence of more than two valence states of Fe present in Fe_3O_4.

(II) The second region (labeled B), typically 6 – 20 eV after the threshold, shows a strong feature peaked at about 543 eV. This region is attributed to O 2*p* states hybridized with Fe 4*s* and Fe 4*p* states.[58] This structure can be related to the symmetry set up by the nearest oxygen neighbors. The large energy spread is an indication of significant covalency in these oxides.[58].

Additional O K-edge absorption spectra from oxidized Fe films with initial thicknesses of 0.8 ML, 1.4 ML and 2.6 ML are shown in figure 4.10. This is normal incidence data obtained with an angle between the **E** vector of the light and the surface normal of ~5 degrees. The 0.8 ML, and 1.4 ML films are similar. In region A, the "pre-peak" or near-edge region indicates a single sharp peak at about 534 eV.

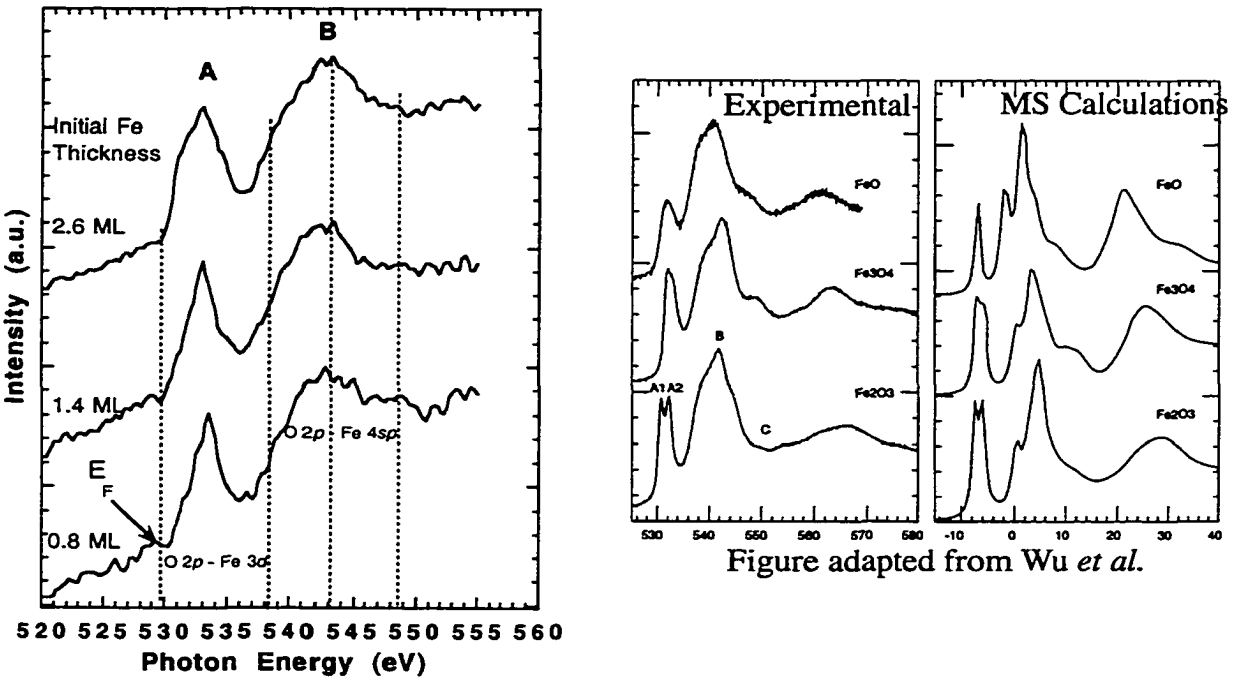

Figure adapted from Wu *et al.*

Figure 4.10: O K-edge absorption spectra of oxidized Fe/Cu(100) films with initial thicknesses of 0.8 ML, 1.4 ML and 2.6 ML obtained at normal incidence. The data on the right was adapted from Wu *et al.* [59] (obtained from single crystals).

Region B did not change significantly, but we notice an additional feature at ~ 549 eV with a slightly higher intensity for the 0.8ML oxide.

The top curve for the thicker oxide (formed from 2.6 ML Fe/Cu(100)) in figure 4.10 is different from the two thinner oxides. In region A, in addition to the sharp peak centered at ~534 eV, we notice a second peak starts to form at ~ 532 eV and peak A is much broader indicating the presence of two valence states of Fe which is consistent with the formation of Fe_3O_4.[58]. The features in region B are also slightly broader for the thicker oxide and the centroid of the broad peak is slightly shifted towards higher photon energy at 544 eV. There is remarkable agreement between our data and data published recently by Wu *et al.* (indicated next to figure 4.10). They calculated the characteristic features of the O K-edge absorption spectra in the light of full multiple scattering (MS) method.[59]

Their calculations revealed a narrow near-edge peak for FeO single crystal, while for Fe_3O_4 a broad peak reveals the presence of both Fe^{2+} and Fe^{3+} valence states.

4.5.2 Iron $L_{2,3}$ Edges

The spectra from the Fe $L_{2,3}$ edges of a 2.3 ML Fe/Cu(100) film is shown in figure 4.11 before and after oxidation.

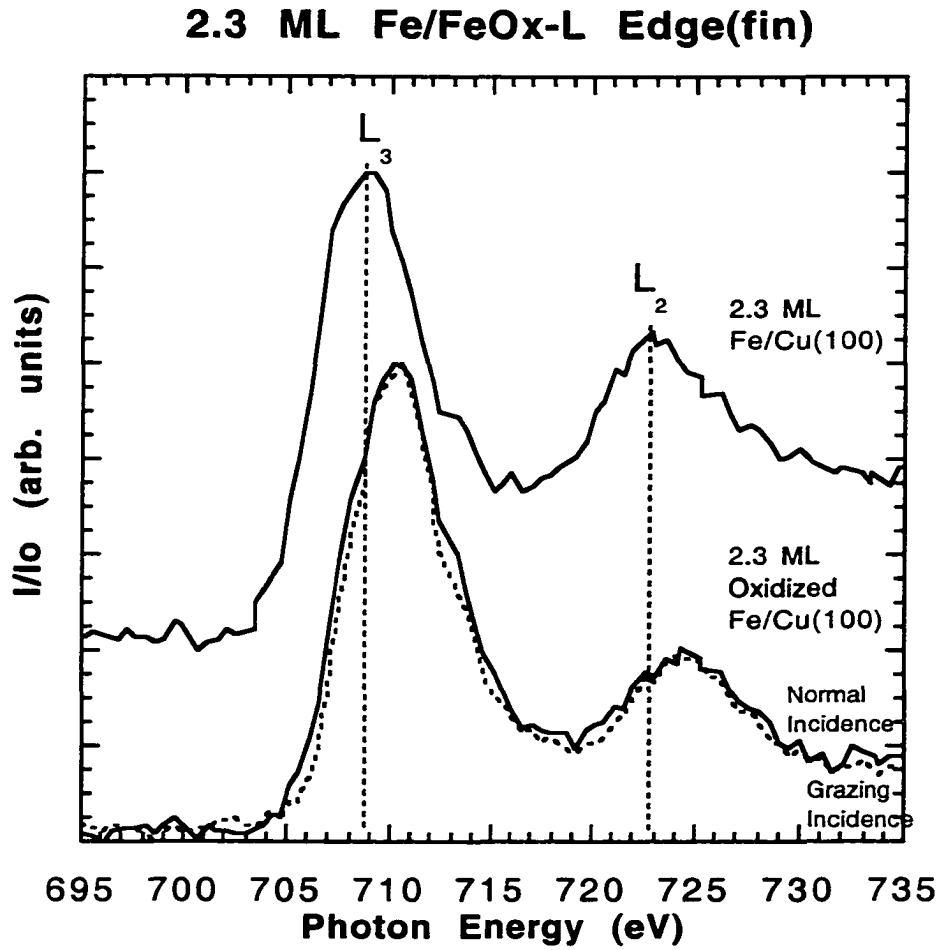

Figure 4.11: (a) Fe $L_{2,3}$ edges of a 2.3 ML Fe/Cu(100) film before (top), and after(bottom) oxidation. All spectra were normalized at a photon energy of 735 eV. The top spectrum represents the clean Fe/Cu(100).

The top spectrum was obtained from unoxidized Fe/Cu(100) and the arrows indicate the position of E_F from the XPS $2p$ data. The edges exhibit similar profiles, which, as in photoemission, are separated by the spin-orbit splitting of the Fe $2p_{3/2}$ and Fe $2p_{1/2}$ levels. Several authors [64] have compared the $I(L_3)/I(L_2)$ line ratio and peak shifts for Fe metal and FeO phases using electron energy loss spectroscopy (EELS). Leapman[65] reported a Fe $2p_{3/2}$ shift of 1.4 eV between Fe metal and FeO, as well as a $I(L_3)/I(L_2)$ line ratio of 3.1 for metal and 5.5 for FeO respectively.

When the 2.3 ML Fe/ Cu(100) film is oxidized, we obtain the spectra shown in the bottom of figure 4.11. The absorption spectrum for normal incidence is given by the solid curve, and that for grazing incidence is given by the dashed curve.

Upon oxidation, one can see that both $L_{2,3}$ features shift by 1.4 eV to higher photon energy. This chemical shift results from the reduced core-hole screening that results when the iron transfers $3d$-electrons to oxygen in forming the bond. The reduced $3d$ population means that a photoexcited $2p$ electron will sense more of the nuclear charge and thereby exhibit a higher binding energy. In the oxide spectrum taken at normal incidence, we notice a small shoulder on L_3 at ~712.3 eV that is not

as strong at grazing incidence angles (dotted spectrum at bottom). The peaks at grazing incidence are also slightly narrower when compared to normal incidence.

Figure 4.12 is a series of Fe L-edge spectra from Fe oxides formed with different initial Fe thicknesses. We notice that the shift from the metallic Fe peak is about 0.4 larger for the thinner oxide (1.4 ML) as compared to the thicker oxides.

Figure 4.13 shows the data obtained for the Fe $L_{2,3}$ edges of an oxidized 1.4 ML Fe/Cu(100) film for two different angles between the **E** vector of the incoming light and sample normal. The top spectrum was taken at a grazing angle, while the bottom spectrum was taken at normal incidence. A 14% difference between the intensities of the lines was observed in our data. This observation suggests that these transitions are sensitive to the orientation (polarization) of the incident light.

When the light is incident on the surface at grazing angles, then the **E** vector of the incoming photon beam oscillates in a direction normal to the surface. The light, hence, would couple strongly with bonds that are directed out of the plane of the sample. (Quantum mechanically the L_3 transitions will be favored.) The reason for this higher intensity in thinner FeO like oxides (as in figure 4.13) may be the increase of the number of unoccupied 3*d* states available for mixing with O 2*p* states (hybridization) within the monolayer.

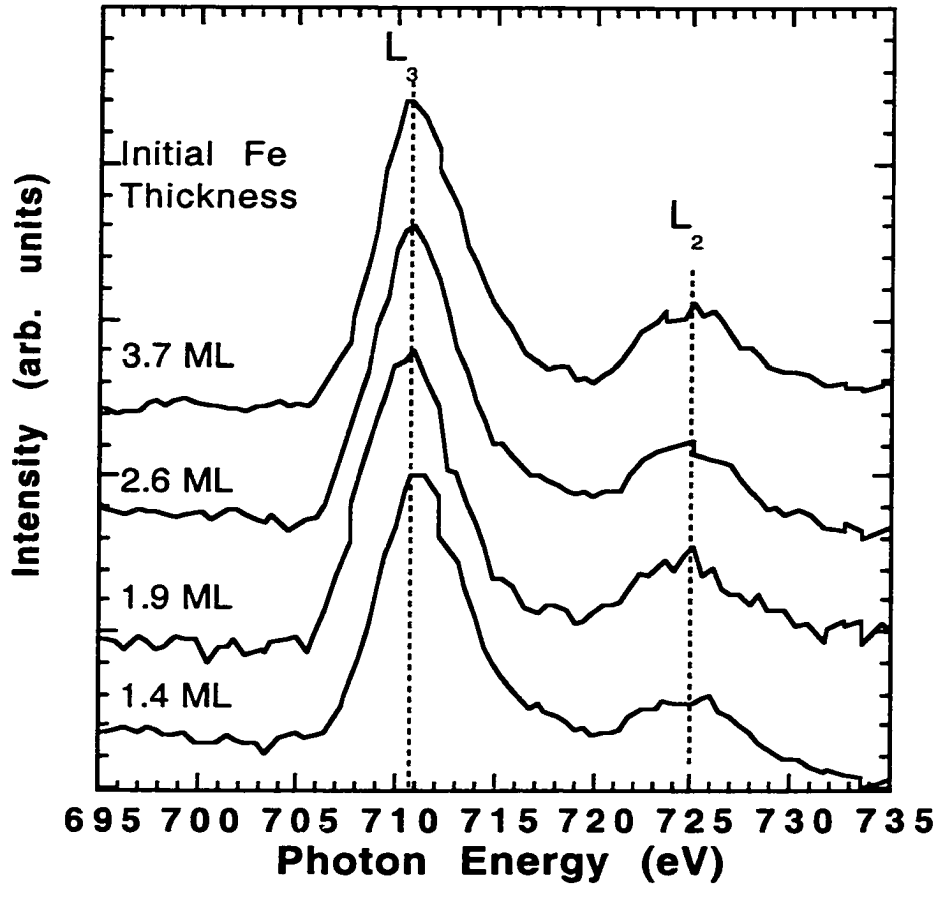

Figure 4.12: Fe L-edge spectra taken from oxides with different initial Fe thickness. The spectra are all similar but we notice a small phase shift for the thinner oxide (1.4 ML) of about 0.4 eV as compared to the thicker oxides.

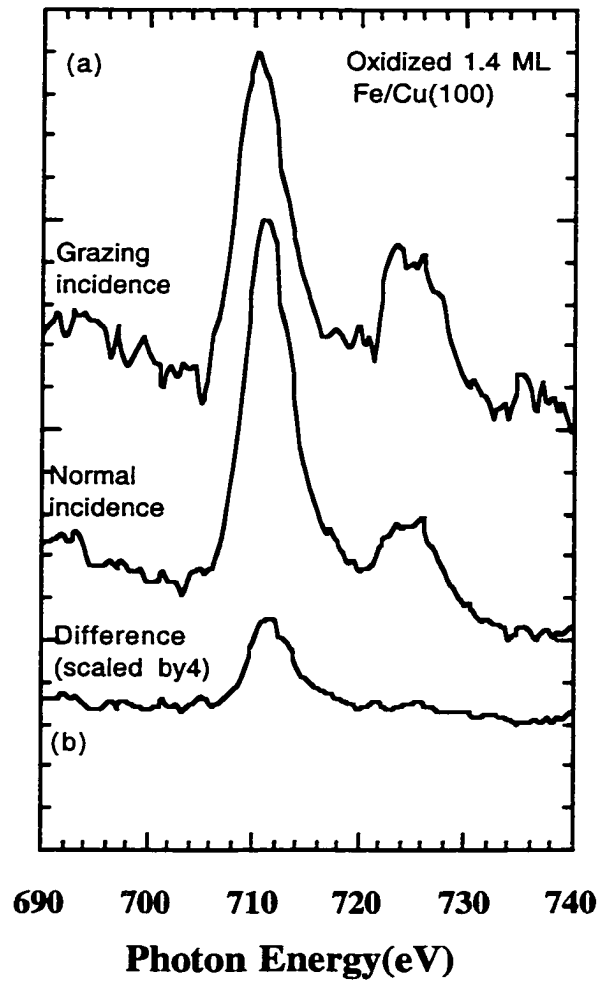

Figure 4.13: Fe $L_{2,3}$ edges of an oxidized 1.4 ML Fe/Cu(100) film for both normal and grazing incidence. The difference spectrum is indicated at the bottom of the figure and it shows a 14% higher intensity of the ratios of the two lines depending on grazing angle.

This can be related to either the different local surroundings of the Fe cations within the mono- and multilayers or due to coupling of occupied Fe 3*d* states with unoccupied underlying Cu 3*d* states at the substrate overlayer interface. The observed polarization dependence is not due to surface effects like roughness, etc. since the LEED patterns exhibit sharp spots and low background intensities. STM images of the FeO revealed a smooth 5 Å high FeO layer.

Chapter 5

Discussion and Conclusions

5.1 Ultrathin Fe Films on Cu(100)

5.1.1 Review of Previous Work on Fe/Cu(100)

Ultrathin Fe films deposited on a Cu(100) substrate exhibit very interesting magnetic and structural properties in the 0.5 ML to 12 ML range. Bulk Fe normally crystallizes in the bcc phase at 300K, but above 1184 K it exists as fcc Fe.[41] The pseudomorphic growth (meaning Fe is now growing as fcc-Fe) of ultrathin layers of Fe on fcc Cu(100) at room temperature has been under intense scrutiny the past few years.[41, 44]

A general picture has emerged that begins with submonolayer Fe that is under tensile stress from matching the larger Cu lattice spacing. In an attempt to maintain a constant volume per atom, the ultrathin fcc Fe experiences a tetragonal distortion (for thicknesses < 5ML) and the dimension perpendicular to the film is contracted.[41] In this face centered tetragonal thickness regime, the films have a

uniform high spin ferromagnetic phase with the easy magnetization axis perpendicular to the film surface.[38]

As thicker films are grown (between 5 and 11 ML), the Fe/Cu(100) film is undistorted fcc. Furthermore, at 5 ML, there is a precipitous drop in the perpendicular magnetization, which is thought to reside in a "live" FM surface layer with the underlying Fe proposed to be antiferromagnetic (AFM).[38] Experimental confirmation of this remains to be found. For Fe coverages of more than 11 ML, fcc Fe becomes unstable and transforms into the bulk FM bcc Fe.[38]

The sensitivity of the fcc Fe moment to atomic volume was investigated using band structure calculations, and it was found that the electronic band structure, and hence magnetic moment, depended critically on atomic volume (as discussed in Chapter 3).[45]

5.1.2 This Investigation on Ultrathin Fe/Cu(100)

The thickness-dependent structural and magnetic changes, observed in ultrathin Fe films deposited on Cu(100) films, prompted us to investigate the nature of the electronic structure within these thickness ranges. Specifically, we were interested in investigating the extent that these phase transitions were reflected in the electronic structure at the Fermi surface.

Structurally, our LEED measurements of ultrathin Fe layers on Cu(100) show a perfect (1 x 1) pattern indicating good pseudomorphic growth. With increasing Fe coverage, the LEED pattern remains (1 x 1), but the sharp spots became more diffuse. This is most likely due to relaxation in the film caused by the crystal mismatch discussed earlier.

In order to explore the spectroscopic differences between tetragonally-distorted fcc (< 5ML) and the fcc (5ML – 11 ML) Fe films on Cu(100), we conducted a valence band photoemission study. Since the valence electronic band structure depends on the atomic volume, we expect to observe a change in the photoemission spectra and Fermi surface contours as a function of film thickness as we go through the 5 ML-transition. Angle–integrated photoemission curves for varying thicknesses of Fe/Cu(100) taken with $h\nu$ = 90eV, showed differences in the bands for thin and thick films.

Further analysis, using difference spectra (Fe/Cu signal minus Cu signal) between a thick and thin film, revealed some interesting results. The difference curves effectively provide a spectrum of the Fe-induced changes in the surface density of states (DOS). The spectra for thicker films were consistent with a bcc-like electronic DOS. However, the curves for thinner films were unlike bcc Fe.

To understand the difference spectra between these Fe/Cu(100) films, band structure calculations were conducted in collaboration with Chris Harwell and Randall Hall from the LSU Chemistry Department.[48] These were linearized augmented plane-wave (LAPW) calculations using the generalized gradient approximation.[49] Using bulk FM fcc and bcc lattice parameters, these calculations showed that the DOS within the bands vary, and the bandwidths are similar for the two phases. While the bcc structure shows a DOS more sharply-peaked near the top of the band, the fcc phase is significantly flatter, consistent with the observed data.

Additional information on the electronic changes that are occurring can be extracted from measurements of Fermi surface contours as a function of film thickness. Fermi surface images from fcc Fe films with thicknesses below 5 ML showed distinct features in the [100] directions. For thicker films (> 5ML), these local intensity maxima appear to *rotate by 45°*. The calculated fct to fcc contours do not agree well with the observed data, however. We have not yet computed an antiferromagnetic fcc structure, such as that proposed by Asada and Blügel.[46]

The observation of a different structure at the Fermi level, however, is consistent with a structural change and suggests that the atomic volume may be different in fct and fcc Fe/Cu(100) films. This implies that we have observed a link between the magnetic/structural properties and the electronic structure at the ~4-5

ML transition where the magnetization switches from perpendicular FM to this lower-moment, in-plane state.

5.2 Oxidation of Fe Films on Cu(100)

5.2.1 Review of Previous Work on Fe Oxides

The oxides of Fe crystallize in one of four common phases, FeO, α-Fe_2O_3, γ-Fe_2O_3 and Fe_3O_4. The bulk oxide phase diagram as a function of temperature and oxygen partial pressure suggests that appropriate thermal treatment and oxygen exposure can form the desired Fe oxide phase however, the surface phase diagram for Fe oxides is not the same as in the bulk. Furthermore, it is likely that a separate phase diagram exists for each kind of substrate and orientation, whether it is a single-crystal oxide, a bulk metal, or a thin film.

Recent experiments have demonstrated that it is possible to stabilize a few of these complex oxide structures in the form of ultrathin films by epitaxial growth on appropriate crystalline substrates. Particularly, thin films of Fe oxides have been successfully grown on oxide substrates.[10, 11, 12, 13]

Previous studies on the room temperature oxidation of Fe/Cu(100) revealed contradictory results, with some investigators reporting the formation of α-Fe_2O_3 while others report the formation of both FeO and Fe_3O_4-like species.[17, 18, 66]

These interpretations relied heavily on XPS measurements. However, the interpretation of Fe *2p* core-levels in a mixed oxide is problematic due to the presence of satellite structures and the broad, overlapping features of differing Fe charge states. These contradictory results at 300 K warranted further investigation of the Fe oxidation process on Cu(100) to determine which factors (temperature, oxygen exposure, etc.) govern the formation of which oxide.

In a purely *structural* study, Karunamuni investigated the morphology of ultrathin Fe oxide films on Cu(001) formed at elevated temperature using STM and LEED. Two distinct oxides were observed depending on the initial Fe coverage. For Fe films of less than 2 ML thick, FeO(111) forms with preferential island growth along the [110] directions. For initial Fe coverage exceeding 2 ML, a new oxide phase identified as $Fe_3O_4(111)$, forms consisting of uniformly thick patches of oxide with large, atomically-flat terraces. This oxide also grows in strips oriented 15° from the [010] azimuth. The different oxides were identified *structurally*, but no *spectroscopic* evidence was given to verify that FeO and Fe_3O_4 were indeed formed.

Furthermore, some of the results obtained from the STM study were not well understood and some questions remained unanswered. For instance, what is the nature of the pits that are formed on Cu terraces during the oxidation processes?

Does the valency of the oxides agree with the known valencies of bulk oxides? Does the Cu(100) oxidize under our treatment?

5.2.2 This Investigation on Oxidized Fe/Cu(100)

This investigation sought to address these questions, making use of photoemission and photoabsorption to investigate the oxidation states of the different oxides formed at elevated temperature. As a transfer standard for comparison with prior STM work, LEED patterns were used to determine which oxide forms under the different conditions described above. For oxides formed from thin Fe films on Cu(100) our LEED showed the presence of two domains, each with a hexagonal superstructure rotated 90 degrees with respect to each other. This is consistent with the STM observation of 2 mutually perpendicular domains observed by Karunamuni for FeO. Furthermore, the oxide pattern is split into multiple higher order diffracted spots (indicating a superlattice) that are aligned with the (100) direction on the Cu substrate. This compares well with STM results by Karunamuni indicating a superlattice structure with a periodicity of 20.5Å on FeO. LEED data for thicker oxide films on Cu(100) were not as conclusive as the FeO films.

One concern that we had about our oxidation procedure was that we might inadvertently oxidize the underlying Cu substrate. Oxidation of the Cu substrate would further complicate the interpretation of subsequent photoemission and

photoabsorption data. To test for the possibility of Cu oxidation, we exposed a clean Cu surface to oxygen using our typical oxidation procedure. The subsequent photoemission spectra revealed clean and well-ordered Cu(100) with no sign of oxidation of the substrate.

The shifts (and shapes) in the peaks of the XPS spectra are normally used to determine changes in the valence-state of different oxides. Upon oxidation of our Fe/Cu(100) films, the Fe 2*p* peaks underwent core level shifts towards higher binding energies. However, for the X-ray anode used, the Fe 2*p* peaks were located between O and Cu LMM Auger peaks and their overlapping features made the identification of Fe^{2+} and Fe^{3+} valence states ambiguous. In order to circumvent this problem, we decided to investigate chemical shifts in the Fe 3*p* shallow core levels using synchrotron radiation from the PGM beamline at CAMD.

Using synchrotron light of hν = 165 eV, we probed the shallow 3*p* core levels. The peak for Fe/Cu(100) was located at 53.1 eV and was fitted with a single Gaussian indicating an Fe^{0} state. When ultrathin Fe (< 2 ML) was oxidized, the 3*p* peak shifted by 2 eV to higher binding energy. It was also fitted with a single Gaussian that was consistent with a single Fe valence, the Fe^{2+} state. The Fe^{2+} 3*p*-peak position compares very well with data reported in literature for FeO.[56]

For thicker oxidized Fe films, the Fe 3*p* peak broadened substantially and an additional Gaussian peak was needed for an adequate fit. This second Gaussian implies that a second Fe valence is present in the oxide film. The oxide formed from thicker Fe films contains both Fe^{2+} and Fe^{3+} cations, as does Fe_3O_4. Once again this can be tied directly to Karunamuni's STM work where he identified the phase for the higher coverage oxide as Fe_3O_4.

In bulk Fe_3O_4, we expect to get two Fe^{3+} for each Fe^{2+} and the ratio of the area of the Fe^{3+}/Fe^{2+} peaks is 1/2, far from the value of 2/1. This can be explained by looking in more detail at the interface between the oxide and the substrate. In the structural model proposed by Karunamuni, the oxide was locked into registry with the Cu substrate by a first layer of metal ions. These ions are coordinatively unsaturated by oxygen and this deficiency may lead to an increased fraction of the lower valence states. This is consistent with the ratio observed.

Another method of interrogating the Fe valence states in the oxides is to measure NEXAFS spectra. O K-edge spectra revealed a distinct difference in the near-edge peaks for oxides formed on Cu(100) from thin Fe and thick Fe. The near-edge peaks for oxides formed from < 2 ML Fe/Cu(100) is a narrow single peak indicating a single Fe valence state. For oxides formed from > 2 ML Fe/Cu(100), we

get a much broader peak indicating the presence of two valence states of Fe which is consistent with the formation of Fe_3O_4. Our data compares well with MS calculations performed by Wu, *et al.* which revealed a narrow near-edge peak for FeO bulk, while showing a broad peak for Fe_3O_4 indicating the presence of both Fe^{2+} and Fe^{3+} valence states.[59]

Valence band photoemission data for low initial Fe coverage shows a broad O *2p-valence* band with a low density of states at the Fermi edge. With increasing initial Fe coverage (>2 ML), the O 2*p* peak becomes more peaked, Cu 3*d* features become enhanced, and the Fermi edge shows a higher DOS. This DOS is significantly higher (almost metallic-like) than that from either Cu, or any of the oxides of Fe. The same observations were made using the EMA at CAMD. This observation is also consistent with the suggestion that the interface is deficient in oxygen as mentioned above.

At lower initial Fe thickness, the oxide covers much of the Cu substrate surface after the high temperature oxidation, and Cu signals are nearly attenuated. However, one remarkable observation noted in almost all the photoemission data is that the oxide resulting from larger amounts of Fe on the surface provided an increasing Cu signal. The presence of the strong Cu signals suggests that either the

Cu is located on top of the oxide film, or that the oxide has formed patches with exposed Cu between the islands.

We tested for the presence of Cu atop the oxide by angle-dependent XPS measurements. If the Cu covered the oxide surface, we would expect to see an enhancement of the Cu signal at grazing angle, coupled with a less intense Fe signal. However, we did not see any changes in the relative intensities of the peaks. Furthermore ARUPS showed strong dispersion of the Cu signal. This indicated that the Cu did not cover the oxide and that the Cu signal came from the substrate. These measurements show conclusively that Cu is not coating the oxide surface.

If bare Cu is present in increasing amounts for thicker initial Fe films, one might expect that columnar oxide growth might be involved. This is inconsistent with STM data however, which show that the oxide islands remain flat. These data also suggest that the islands range from ~5A to ~10 A thick. Although we do not know the extent to which these islands are embedded deep into the Cu substrate, their small size seems to be inconsistent with the large initial Fe coverage. This may be explained, though, by considering the oxidation process.

As reported above, XPS showed the migration of Fe atoms into the underlying Cu substrate after repeated cycles of oxide formation at higher temperature. This suggests that we could have two processes competing with one

another on the surface: a) oxide formation and b) diffusion of Fe atoms into the Cu substrate. Note that this latter phenomenon is unique to the surface phase diagram since Fe and Cu are immiscible in the bulk.

5.2.3 Proposed Model for Missing Fe After Oxidation

Figure 5.1 is a schematic of a proposed model to account for the "missing Fe". The oxidation procedure at elevated temperature, consists of exposing the Fe/Cu(100) layers to $1x10^{-6}$ Torr oxygen at room temperature and then to start simultaneously the heating process.

For low Fe thickness the entire thin Fe overlayer can react with the oxygen to form FeO islands upon annealing to 810K. The FeO layer is bonded strongly to the Cu surface and almost no alloying of the Fe takes place since it already formed the thermodynamically stable FeO overlayer. STM data shows that the Cu substrate morphology changes in order to accommodate this ionic lattice which produces large flat terraces in the regions adjacent to the oxide. Since the cohesive energy of the oxide lattice is so large (11.6 eV per formula unit for spinel), it easily drives Cu steps to flow and group to provide the large terraces that are stabilized by the ionic lattice's Madelung energy.[3] Furthermore, for the thicker initial Fe/Cu(100) films we note that upon oxidation at 810 K, oxidation of the uppermost layer takes place.

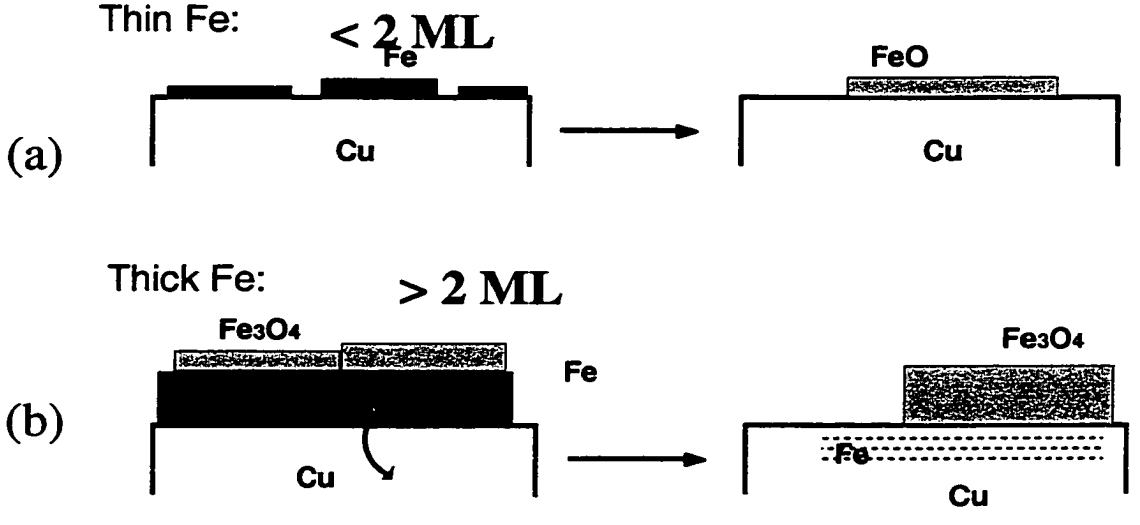

Figure 5.1: Schematic of proposed model to account for missing Fe: (a) represents a thin Fe layer (<2ML) that is oxidized at 810 K to FeO. The rate of FeO formation is much faster than surface alloying. (b) represents a thick Fe/Cu(100) layer. Here the rate of surface alloying of the Fe atoms is much faster compared to the rate of oxide formation on the surface. This results in the formation of less Fe_3O_4 than expected and Fe atoms embedded in the subsurface region.

However, due to the lack of oxygen at the interface, surface alloying at 810 K takes place at a rate competing with oxide growth downward. The competition between oxidation and alloying results in less oxide on the Cu surface, and produces Fe alloyed into the near-surface region.

This model explains the large "pits" seen by Karunamuni on the bare Cu terraces. Fe alloying into the substrate most probably produces these structures. Furthermore, it may also partially contribute to the high DOS observed near E_F in the photoemission spectra.

This model also explains why additional cycles of Argon sputtering were needed to clean the Cu substrate after repeated Fe oxidation at elevated temperature to get rid of the near surface Fe present in our sample.

5.3 Conclusions

The work reported in this investigation is on the pseudomorphic growth of ultrathin layers of Fe on Cu(100). We were able to detect a direct link between the electronic properties and the observed magnetic and structural changes reported by several investigators. The Fermi surface of Fe/Cu(100) films in coverages below 5 ML gave a contour that is significantly different than the contours of coverages

higher than 5 ML. This shows a direct link between the electronic properties and structural/magnetic properties has been reported.

In addition, we also reported an experimental study of the growth of iron oxides on a dissimilar metal. We were able to produce extremely well-ordered oxides grown on a metallic surface without oxidizing the Cu substrate. The structure and properties of these oxide films were characterized by an array of experimental techniques including LEED, XPS, UPS and NEXAFS.

One of the oxides formed during this investigation is Fe_3O_4, a magnetic material predicted to provide carriers of only one spin orientation (half-metallic). This may provide a significant new step towards the development of microelectronic devices like magnetic RAM and more sensitive computer disk head sensors based on spin-dependent transport. Cu is a metal that is compatible with current device components and the growth of an ordered oxide on a Cu substrate make this work extensible in a direct manner to technologically interesting applications. Furthermore this spectroscopic study provides some interesting observations of the fundamental processes at work in thin film growth and oxidation.

A point of concern for device application is the Fe alloying that took place in the near surface region of the Cu substrate. A phase diagram that guides the formation of these ultrathin ordered Fe oxide films on Cu needs to be developed in

order to better control the parameters of oxygen pressure, annealing temperature and time needed to form these oxides.

References

1. G. A. Prinz, *Science* **282**, 1660-1663 (1998).

2. M. N. Baibich, *et al.*, *Phys. Rev. Lett.* **61**, 2472 - 2475 (1988).

3. R. L. Kurtz, J. Karunamuni, and R. L. Stockbauer, *Phys. Rev. B.* **60**, R16 342 (1999).

4. R. J. Soulen, *et al.*, *Science* **282**, 85-88 (1998).

5. Z. Zhang, and S. Satpathy, *Phys. Rev. B* **44**, 13319-13331 (1991).

6. S. F. Alvarado, *et al.*, *Phys. Rev. Lett.* **34**, 319-322 (1975).

7. R. J. Lad, and V. E. Henrich, *Phys. Rev. B* **39**, 13478-13485 (1989).

8. M. Wuttig, B. Feilmann, and T. Flores, *Surf. Sci.* **331-333**, 659-672 (1995).

9. O. Muller, and R. Roy, *Springer-Verlag,* (1974).

10. J. F. Anderson, *et al.*, *Phys. Rev. B* **56**, 9902-9909 (1997).

11. J. A. Borchers, *et al.*, *Appl. Phys. Lett.* **64**, 381-383 (1994).

12. Y. Q. Cai, M. Ritter, W. Weiss, and A. M. Bradshaw, *Phys. Rev. B* **58**, 5043-5051 (1998).

13. Y. J. Kim, *et al.*, *Phys. Rev. B* **55**, R 13448-R13451 (1997).

14. D. Lind, S. D. Berry, G. Chern, and H. Mathias, *Phys. Rev. B* **45**, 1838 (1992).

15. A. Barbieri, W. Weiss, M. A. van Hove, and G. A. Somarjai, *Surf. Sci.* **302**, 259-279 (1994).

16. H. den Daas, O. L. J. Gijzeman, and J. W. Geus, *Surf. Sci.* **285**, 15-26 (1993).

17. K. Kishi, and J. Nishioka, *Surf. Sci.* **227**, 97 (1990).

18. L. Lozzi, M. Passacantando, P. Picozzi, S. Santucci, and H. den Daas, *Surf. Sci.* **331-333**, 703 - 709 (1995).

19. J. Karunamuni, *Ph.D. Thesis*, Louisiana State University (1999).

20. C. R. Brundle, C. A. Evans Jr., and S. Wilson, Eds., *Encyclopedia of Materials Characterization* (Butterworth-Heineman, Greenwich, 1992).

21. D. P. Woodruff, and T. A. Delchar, *Modern Techniques of Surface Science - Second Edition.* E. A. Davis, I. M. Ward, D. R. Clarke, Eds., Cambridge Solid State Science Series (Cambridge University Press, Cambridge, ed. 2, 1994), vol. 14.

22. M. A. Van Hove, W. H. Weinberg, and C.-M. Chan, *Low-Energy Electron Diffraction.* G. Ertl, Ed., Springer Series in Surface Science (Springer Verlag, Berlin Heidelberg New York, ed. 1, 1986), vol. 6.

23. H. Lüth, *Surfaces and Interfaces of Solid Materials* (Springer, Berlin Heidelberg New York, ed. 3, 1996).

24. S. D. Kevan, *Phys. Rev. Lett.* **50**, 526 (1983).

25. C. N. Berglund, and W. E. Spicer, *Phys. Rev.* **136**, 1030 (1964).

26. E. O. Kane, *Phys. Rev. Lett.* **12**, 97 (1964).

27. W. E. Spicer, *Phys. Rev.* **112**, 114 (1968).

28. F. J. Himpsel, *J. Appl. Optics* **19**, 9 (1980).

29. R. L. Stockbauer, and A. Pararas, *Nucl. Instrm. Meth. Phys. Res. A* **266**, 560 (1988).

30. Z. Qu, *et al.*, *Surf. Sci.* **324**, 133 (1995).

31. J. Stöhr, Ed., *NEXAFS Spectroscopy* (Springer, Heidelberg, 1992).

32. J. J. Sakurai, *Modern Quantum Mechanics*. S. F. Tuan, Ed. (Addison-Wesley, Reading,Massachusetts, ed. Revised, 1994).

33. R. L. Stockbauer, P. Ajmera, E. D. Poliakoff, B. C. Craft, and V. Saile, *Nucl. Instrm. Meth. in Phys. Res.* **A291**, 505 (1990).

34. E. Morikawa, J. D. Scott, E. D. Poliakoff, R. L. Stockbauer, and V. Saile, *Rev. Sci. Instrum.* **63**, 1300 (1992).

35. G. J. Mankey, M. T. Kief, F. Huang, and R. F. Willis, *J. Vac. Sci. Technol. A* **11**, 2034 (1993).

36. J. Karunamuni, R. Kurtz, and R. Stockbauer, *Surf. Sci.* **442**, 223-238 (1999).

37. G. J. Mankey, R. F. Willis, and F. J. Himpsel, *Phys. Rev. B* **48**, 10284-10290 (1993).

38. J. Thomassen, F. May, B. Feldmann, M. Wuttig, and H. Ibach, *Phys. Rev. Lett.* **69**, 3831 (1992).

39. D. Li, M. Freitag, J. Pearson, Z. Q. Qiu, and S. D. Bader, *Phys. Rev. Lett.* **72**, 3112 (1994).

40. D.-S. Wang, A. J. Freeman, and H. Krakauer, *Phys. Rev. B* **24**, 1126 (1981).

41. J. Giergiel, J. Shen, J. Woltersdorf, A. Kirilyuk, and J. Kirschner, *Phys. Rev. B* **52**, 8528-8534 (1995).

42. S. E. Greco, J. P. Roux, and J. M. Blakely, *Surf. Sci.* **120**, 203-222 (1982).

43. J. Thomassen, B. Feldmann, and M. Wuttig, *Surf. Sci.* **264**, 406-418 (1992).

44. D. Chambliss, and K. E. Johnson, *Surf. Sci.* **313**, 215-226 (1994).

45. D. Bagayoko, and J. Callaway, *Phys. Rev. B* **28**, 5419 (1983).

46. J. Asada, and S. Blugel, *Phys. Rev. Lett.* **79**, 507 (1997).

47. M. P. Seah, and W. A. Dench, *Surface and Interface analysis* **1**, 2 (1979).

48. R. H. Madjoe, *et al.*, *Journal of Applied Physics* **85**, 6211-6213 (1999).

49. P. Blaha, K. Schwarz and J. Luitz, WIEN97, *A Full Potential Linearized Augmented Plane Wave Packet for Calculating Crystal Properties* (Karlheinz Schwarz, Techn. Univ. Wien, Vienna 1999).

50. G. J. Mankey, K. Subramanian, R. L. Stockbauer, and R. L. Kurtz, *Phys. Rev. Lett.* **78**, 1146 (1996).

51. V. S. Smentkowski, and J. T. Yates, *Surf. Sci.* **232**, 113-128 (1990).

52. T. Maeda, Y. Kobayashi, and K. Kishi, *Surf. Sci.* **436**, 249-258 (1999).

53. K. Kishi, and S. Nishioka, *Surf. Sci.* **179**, 377 (1987).

54. S. A. Chambers, Y. J. Kim, and Y. Gao, *Surf. Sci. Spectra* **5**, 219-228 (1998).

55. K. E. Johnson, D. D. Chambliss, R. J. Wilson, and S. Chiang, *J. Vac. Sci. Tech.* **A11**, 1654-1660 (1993).

56. H.-J. Kim, J.-H. Park, and E. Vescovo, *Phys. Rev. B.* **61**, 15 288 (2000).

57. S. Warren, *et al.*, *J. Phys.: Condens. Matter* **11**, 5021-5043 (1999).

58. T. Schedel-Niedrig, W. Weiss, and R. Schlogl, *Phys. Rev. B* **52**, 17 449 - 17 460 (1995).

59. Z. Wu, *et al.*, *Phys. Rev. B* **55**, 2570-2577 (1997).

60. C. Colliex, T. Manoubi, and C. Ortiz, *Phys. Rev. B.* **44**, 11 402 (1991).

61. Y. Ma, *et al.*, *Phys. Rev. B* **48**, 2109 (1993).

62. F. M. de Groot, J. C. Fuggle, B. T. Thole, and G. A. Sawatsky, *Phys. Rev. B* **42**, 5459-5468 (1990).

63. J. Stöhr, and R. Jaeger, *Phys. Rev. B.* **26**, 4111 (1982).

64. B. T. Thole, and G. van der Laan, *Phys. Rev. B* **49**, 9613 (1994).

65. R. D. Leapman, L. A. Grunes, and P. L. Fejes, *Phys. Rev. B* **26**, 614 (1982).

Vita

Reginaldt Hamilton Madjoe was born in Pretoria, South Africa, on August 16, 1964 to Mary Madjoe and Abel Madjoe (deceased 1973). He has two siblings: an elder sister Unice, and a younger brother Simon who is a science teacher. He graduated from Eersterust High School in Pretoria. He attended the University of the Western Cape (UWC) in Bellville, Cape Town, in 1983. He graduated with a bachelor's degree in physics as well as a high school teacher's diploma. In 1987 and 1988 he was employed as a science teacher at Ravensmead High School in Cape Town.

In 1989 he returned to the University of the Western Cape (UWC) as a senior laboratory assistant (similar to graduate/teaching assistant in US) and in 1991 he was awarded the bachelor of science (Hons) degree from UWC. Reginaldt was employed as a junior lecturer in the physics department at the University of the Western Cape in 1992 where he taught undergraduate physics. He continued his studies and received a masters degree from UWC in March of 1994. His masters' thesis (done under supervision of Dr R. Pretorius) was entitled "The formation of cobalt silicide layers in Si<111> by laser-induced epitaxy". In 1995 he was promoted to full lecturer in the Physics department at UWC.

In June 1995 he was offered the South African Educational Program (SAEP) fellowship (administered by the Institute of International Education in Washington, D.C.) to pursue a fulltime doctoral program in the US.

Reginaldt was granted extended study leave by UWC and in the fall of 1995, he entered Louisiana State University. He began his research in surface science and condensed matter physics under his major professors, Richard L. Kurtz and Roger L. Stockbauer in November 1996 and is currently a candidate for the degree of Doctor of Philosophy. He is a member of the American Vacuum Society and the South African Physics Society.

He married his lovely wife Lynette Scheepers in 1988 and they are blessed with two boys, Sean (aged 12) and Clarence (aged 7).

DOCTORAL EXAMINATION AND DISSERTATION REPORT

Candidate: Reginaldt Madjoe

Major Field: Physics

Title of Dissertation: Photoemission and Photo-Absorption Studies of Ultrathin Fe Films on Cu(100) Oxidized at Elevated Temperature

Approved:

Major Professor and Chairman

Dean of the Graduate School

EXAMINING COMMITTEE:

Date of Examination:

November 20, 2000